Propagation of terahertz radiation in non-homogeneous materials and structures

Swift, George Peter

UNIVERSITY OF DURHAM

PROPAGATION OF TERAHERTZ RADIATION IN NON-HOMOGENEOUS MATERIALS AND STRUCTURES

GEORGE PETER SWIFT

DEPARTMENT OF PHYSICS

A THESIS SUBMITTED FOR THE DEGREE OF DOCTOR OF PHILOSOPHY

2008

Abstract

The work undertaken is concerned with looking at how terahertz frequency radiation (here defined as 300 GHz -10 THz) propagates through media which have a random structure ("non-homogeneous materials"). Materials of this type are important in a wide range of applications, but are of particular interest in security and surveillance.

Propagation of terahertz radiation through non-homogeneous materials is not well understood: both interference and scattering effects become important in this spectral range, where the wavelength and size and separation of the scattering centres are often commensurable. A simple model, which uses the phase change of a wave to describe its transmission through media having relatively small changes in refractive index is developed and compared with both exact theories and experimentally obtained measurements. Overall, a satisfactory agreement between the experimental data for transmission through arrays of cylinders, textiles and powders is seen.

It is well known that pulses of terahertz radiation from optoelectronic sources have a complex shape. Post detection signal processing routines can be used to clean up the experimentally determined signals. The development of such algorithms is described, before they are applied to experimental results to determine: the minimum size of gaps between slabs to mimic voids in media; and the response of various compounds to a sharply terminated input pulse.

The investigation of scattering from random structures requires the construction of a spectrometer having the capability to measure THz pulses scattered at different angles. Such a system ideally requires fibre-fed detection schemes to be used. The construction of a scattering spectrometer is described and its performance outlined.

Pulses of terahertz which have been scattered by a sample of interest can be reconstructed, using methods from conventional tomography, to produce images of the phantom under test. Such measurements are outlined here. To our knowledge, this is the first time that tomography has been undertaken using a fixed sample and rotating detector arrangement.

Publication list

JOURNAL (REFEREED)

J.R. Fletcher, G.P. Swift, D. Dai, J.A. Levitt and J.M. Chamberlain *Propagation of terahertz radiation through random structures: An alternative theoretical approach and experimental validation:* J. App. Phys. **101** 013102 (2007)
J.R. Fletcher, G.P. Swift, D. Dai, P.C. Upadhya and J.M. Chamberlain *Pulsed THz signal reconstruction:* J App. Phys. **102** 113105 (2007)
A.J. Gallant, M.A. Kaliteevski, D. Wood, M.C. Petty, R.A. Abram, S. Brand, G.P. Swift, D.A. Zeze and J.M. Chamberlain, *Pass-band filters for THz radiation based on dual metallic photonic structures:* App. Phys. Lett. **91** 161115 (2007).
M.A. Kaliteevski, D.M. Beggs, S. Brand, R.A. Abram, J.R. Fletcher, G.P. Swift and J.M. Chamberlain, *Propagation of electromagnetic waves through a system of randomly placed cylinders: the partial scattering wave resonance:* J. Modern Optics **53** (14) 2089 (2006)

CONFERENCE

J.R. Fletcher, G.P. Swift, D. Dai and J.M. Chamberlain, *THz Pulse Reconstruction:* Proc. The Joint 32nd International Conference on Infrared and Millimetre Waves, and 15th International Conference on Terahertz Electronics, 62 (2007)
A.J. Gallant, G.P. Swift, D. Dai, M. Kaliteevski, D.A. Zeze, D. Wood, M.C. Petty, S. Brand, R.A. Abram and J.M. Chamberlain, *Micromaching for Terahertz Artificial Materials:* Mater. Res. Symp. Proc. Vol. 1016, 1016-CC05-07
A.J. Gallant, J.A. Levitt, M. Kaliteevski, D. Wood, M.C. Petty, R.A. Abram, S. Brand, G.P. Swift, D.A. Zeze and J.M. Chamberlain, *Artificial plasmonic materials for THz applications:* Proc. SPIE Vol. 6472, 6472-06 (2007)
J.A. Levitt, A.J. Gallant, G.P. Swift, D. Dai and J.M. Chamberlain, *Terahertz micro-spectroscopy using a transient mirror technique:* Proc. SPIE Vol. 6472, 64720O (2007)
G.P. Swift, J.R. Fletcher, A.J. Gallant, D. Dai, J.A. Levitt and J.M. Chamberlain, *Scattering of THz Radiation from Random Structures:* Proc. The Joint 31st International Conference on Infrared and Millimetre Waves, and 14th International Conference on Terahertz Electronics, 153 (2006)
A.J. Gallant, J.A. Levitt, G.P. Swift, D. Dai, M. Kaliteevski, D. Wood, M.C. Petty and J.M. Chamberlain, *The Fabrication of THz Photonic Filters Using Ultraviolet Based SU8 Micromachining:* Proc. The Joint 31st International Conference on Infrared and Millimetre Waves, and 14th International Conference on Terahertz Electronics, 194 (2006)
G.P. Swift, D. Dai, J.R. Fletcher, A.J. Gallant, J.A. Levitt, R.A. Abram, D.M. Beggs, M.A. Kaliteevski and J.M. Chamberlain, *Terahertz scattering: comparison of a novel theoretical approach with experiment:* Proc. SPIE Vol. 6120, 61200R, (2006)*
J.R. Fletcher, G.P. Swift, D. Dai, D.M. Beggs, R.A. Abram, M.A. Kaliteevski, J.A. Levitt, A.J. Gallant and J.M. Chamberlain, *Scattering in THz imaging:* SPIE meeting on Defense and Security, Bruges, Sept 2005

OTHERS

G.P. Swift, The combination of signal processing and broadband terahertz spectroscopy for the imaging of defects: The Rank Prize Funds Mini-Symposium on Optical Aspects of Non Destructive Testing, Wordsworth Hotel, Grasmere, May 2008
G.P. Swift, J.R. Fletcher, J.A. Levitt, D.C. Dai and J.M. Chamberlain, *Propagation of Terahertz Radiation in random structures,* Physics Poster Session for young researchers, SET for Britain, Houses of Parliament, Nov 2006*
G.P. Swift, J.R. Fletcher, D.M. Beggs, M.A. Kaliteevski, R.A. Abram, D.C. Dai, J.A. Levitt, A.J. Gallant and J.M. Chamberlain, *Terahertz Scattering: comparison of a novel theoretical approach with experiment,* Poster Session at Her Majesty's Government Communication Centre meeting on Terahertz Security Applications, Grey College, University of Durham, Sept 2005*

Declaration

The work presented in this thesis was carried out in the Terahertz Physics Group in the Department of Physics, University of Durham between October 2004 and December 2007. This work has not been submitted for any other degree in the University of Durham, or elsewhere, and unless otherwise stated, is the original work of the author.

Copyright

Acknowledgements

I would like to begin by thanking my supervisor, Professor Martyn Chamberlain for all his help, support and constant encouragement during the completion of this work. I am gratefully indebted to Dr. Howard Cummins of HMGCC (Her Majesty's Government Communications Centre) for the financial support which that institution provided during my PhD.

The work undertaken would not have been possible without the advice provided and willingness to help of the rest of the THz group. I would like to extend particular thanks to: Dr John Fletcher, for all his help with the theoretical side of the work as well as his constant wisdom; Dr. DeChang Dai for all his experience and help, teaching me how to work in a THz lab, without whom, the experiments would not have taken place; Dr. James Levitt and Dr. Andrew Gallant for their general advice and company; and the various technical staff. Grateful thanks are also extended to the THz group at the University of Leeds, in particular Professor Edmund Linfield and Dr. Prashanth Upadyha, for useful discussion, growth of LT-GaAs and use of the ultra-broadband setup.

My time in Durham has been made all the more enjoyable through involvement with different groups of people: Grey College Junior, Middle and Senior Common Rooms; Durham University Choral Society; Palatinate Voices; St. Chad's College Choir; along with organ studies under Keith Wright, which have all helped to keep me sane. I would like to acknowledge the support of my many friends, but particularly Dave Clark and Simon King for many enjoyable sociable experiences, their willingness to put up with me, and for being generally good mates.

Finally, I would like to thank my family, and in particular my parents for all the love, support and guidance over the many years of my study at Durham.

Contents

List of Figures

1. Introduction

This thesis is concerned with the study of terahertz radiation and more specifically its propagation through non-homogeneous media, for example clothing and powders that could contain either explosives or drugs of abuse. Work reported in this thesis was undertaken on behalf of HMGCC (Her Majesty's Government Communications Centre) and also formed an important part of the European Union Framework VI TeraNova programme (IST 511415), to investigate, in particular, the interaction of terahertz radiation with random media that are of interest to the security sector.

1.1 An overview of the work undertaken in this thesis

The overall aim of the studies reported here was to investigate the interaction of terahertz (THz) radiation with random structures. Motivation for the work undertaken in this thesis arose from the possible use of terahertz radiation in security applications. Broadband pulses of terahertz radiation can be used to identify materials that are of interest as 'targets' in security and surveillance systems e.g. drugs of abuse and explosives. Many compounds have resonant frequencies within the terahertz region of the electromagnetic spectrum. This means that THz radiation can be used to identify unknown substances by comparing their response to THz radiation with libraries of previously recorded terahertz spectra. However, in real-life applications these target materials will often be secreted behind other materials e.g. clothing, or drugs mixed with a cutting agent. Unfortunately, the average spacing of fibres in clothing and particle size of the powders is comparable with terahertz wavelengths and consequently the radiation is easily scattered. These scattering effects can be used to advantage in imaging and sensing to determine: the characteristic size, texture and location of objects concealed within a matrix of other material. Conversely, they can diminish and scramble the return signal from a suspect item secreted below garments, or produce false positives in spectra when interference takes place within a scattering structure.

Mathematical models have been developed, in collaboration with a theorist, to describe how terahertz radiation propagates through materials of a random nature. These materials contain structures on a scale comparable to that of a terahertz wavelength, which is of the order of a few hundred microns, so scattering phenomena become important. Comparison has been made with experimental measurements of propagation

through phantoms with both known (cylindrical arrays) and unknown (clothing and powders) scatterer positions. The measurements were undertaken using a sensitive, broadband terahertz time domain spectrometer (THz-TDS), built during the period of study.

One common problem in terahertz spectroscopy arises from the fact that there is very little control over the time dependence of the output pulse from a THz-TDS system. The initial pulse from a typical source is followed by various after-runners and echoes, resulting from reflections within the source structure, which produce delayed and dispersed repeats of the initial output. Consequently, the signal detected is more complicated than that expected from the electronic mechanisms within the source itself. Through the use of signal processing, the response of the sample to a single cycle THz pulse can be seen. Experimental measurements were made to test these algorithms by investigating the gap between plates to mimic voids within a larger material. Thus, by using signal processing, additional information can be obtained from the THz signal that would otherwise be lost if simple Fourier Analysis only is performed. Some of these measurements were undertaken using a specially built reflection spectrometer.

This work has been extended to look at the scattered radiation profile from completely random structures. A terahertz spectrometer with the capability of measuring the scattered radiation profile was built, using a fibre-fed detection system. Analysis of the time delays of THz signals at various angles using signal processing, allows a 'picture' of the structure under test to be built.

1.2 Terahertz radiation

Terahertz radiation forms just one small part of the electromagnetic spectrum, which encompasses all electromagnetic waves ranging from long wavelength radio waves, through microwaves, infrared, visible, ultraviolet, to very short wavelength x-rays and gamma rays. These waves all have perpendicular magnetic and electric components, which oscillate transversely to the direction of travel. All of these waves travel at the speed of light in a vacuum and have a fixed relationship between their frequency and wavelength, given by $f = c/\lambda$. Figure 1.1 shows a general electromagnetic wave; the properties of electromagnetic waves are discussed in more detail in section 1.2.

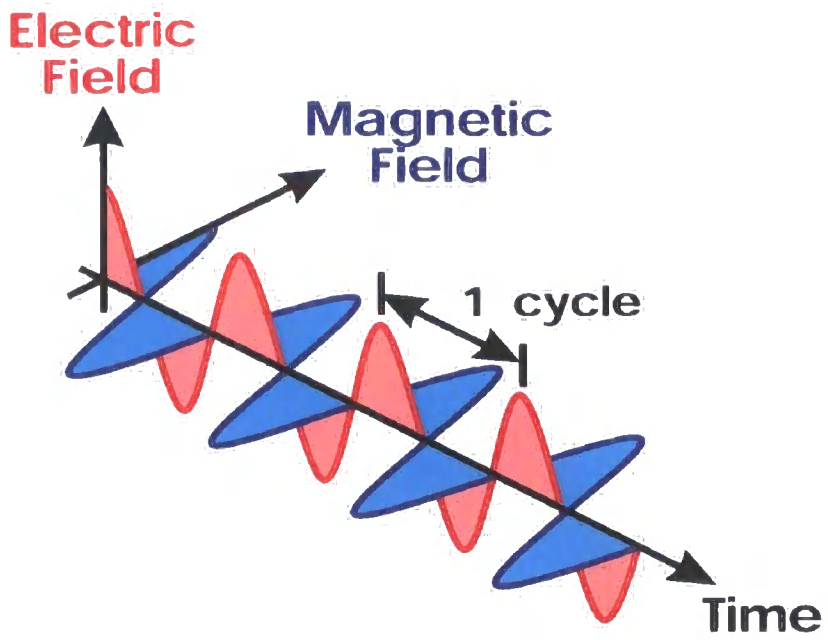

Figure 1.1: An electromagnetic wave.

The terahertz region lies between microwaves and infrared and can broadly be defined as containing waves with frequencies between 300 GHz and 30 THz. Figure 1.2 shows the complete electromagnetic spectrum and provides some idea of its vast scale. It should be noted that a frequency of 1 THz corresponds to a wavelength of 300 μm, a temperature of 47 K and a photon of this frequency has energy 4.1 meV. Unfortunately, the terahertz region of the spectrum sits between the two regimes where a significant change takes place in the method by which the waves are emitted. At the low frequency end of the spectrum, waves are emitted when electrons oscillate in a circuit, with the maximum speed of oscillation normally being limited to several tens of GHz. At higher frequencies, electronic circuits become unresponsive when the upper limit to the frequency of oscillation in transistor like devices, set by the fundamental physics of solids and technological limitations, is reached. Frequency multipliers can be used to achieve higher frequencies, but they suffer from low efficiencies. Conversely, at the high frequency end of the spectrum, waves are emitted when electrons change state, releasing a photon of energy $E = hf$, where h is Planck's constant. X-rays and gamma rays are produced by changes within the atomic nucleus or inner electron state transitions. Lower frequency ultraviolet, visible and infrared radiation arises from atomic and molecular state transitions.

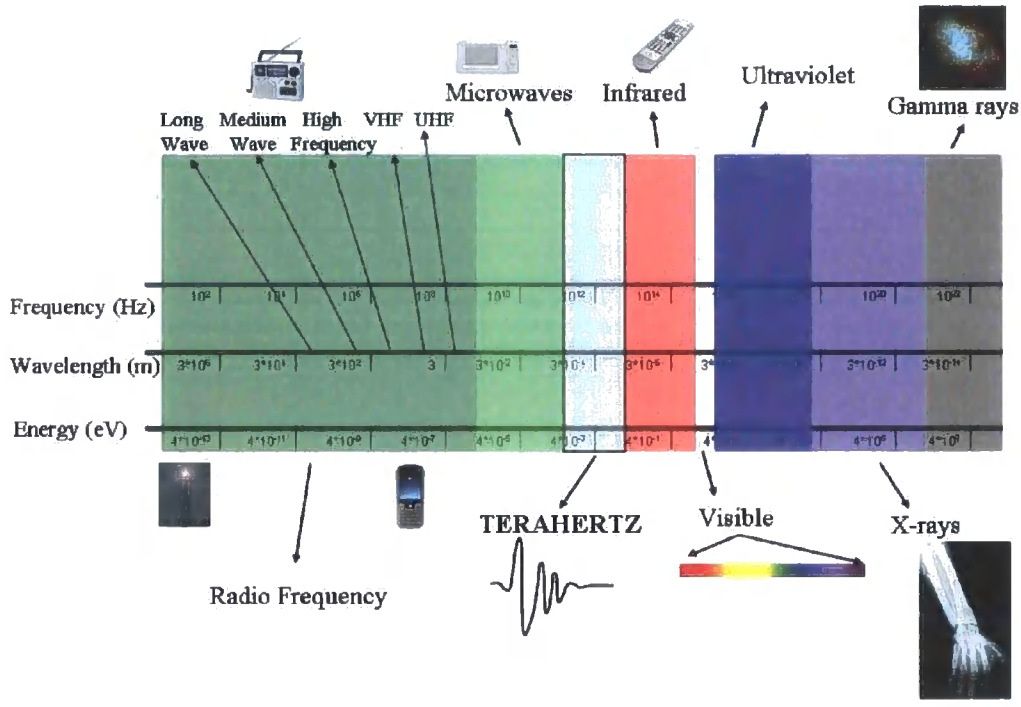

Figure 1.2: The electromagnetic spectrum.

The limitation on the lowest frequencies that can be produced from this method arises from the difficulty of producing lasing, using solid state technology, in which the energy of the emitted photons is less than the thermal energy at room temperature. This leads to the so called famous terahertz gap, where for many years it was almost impossible to manufacture both bright sources and simple detectors, which work at room temperature, of this type of radiation. However, in the past twenty or so years, great progress has been made in finding ways of producing "bright" sources that operate in this regime. These will be discussed more fully in Chapter 2.

1.3 Electromagnetic waves

All electromagnetic waves can be described by a set of laws, developed by Maxwell in the middle of the nineteenth century. The equations relate the electric and magnetic fields to their sources: charges, currents and changing fields. Maxwell's equations in fact summarise the basic laws of electricity and magnetism, namely: Coulomb's Law; Gauss's Law; the Biot-Savart Law; Faraday's Law of magnetic induction; and Ampere's circulation law. These equations are given below in their most usual, differential form:

$$\nabla \cdot \overline{E} = \frac{\rho}{\varepsilon_0}, \qquad (1.1) \qquad \nabla \times \overline{E} = -\frac{\partial \overline{B}}{\partial t}, \qquad (1.2)$$

$$\nabla \cdot \overline{B} = 0, \qquad (1.3) \qquad \nabla \times \overline{B} = \mu_0 \overline{J} + \mu_0 \varepsilon_0 \frac{\partial \overline{E}}{\partial t}. \qquad (1.4)$$

Equation (1.1) is Gauss's Law, relating the electric field to its source, whilst equation (1.3) arises from the fact that magnetic monopoles are not seen to exist. Equation (1.2) is a simple statement of Faraday's Law, stating that changing magnetic fields produce electric fields, and equation (1.4) is a generalised form of Ampere's Law, which states that currents produce circulating magnetic fields. Ampere's Law only applies in the non-time varying case, and Maxwell generalised this to include a displacement current: the current thus becomes a sum of the conduction current, $\mu_0 \overline{J}$ and the displacement current, $\mu_0 \varepsilon_0 \partial \overline{E} / \partial t$.

Maxwell's equations reduce to the laws of electro- and magneto-statics when there is no time variation. Consideration of these equations in a vacuum leads to two wave equations, one each for the electric and magnetic field. For example, taking the curl of equation (1.2) followed by application of a well known vector identity gives:

$$\nabla(\nabla \cdot E) - \nabla^2 E = -\frac{\partial}{\partial t}(\nabla \times \overline{B}). \qquad (1.5)$$

Substitution of equations (1.1) and (1.4) produces the following wave equation:

$$\nabla^2 \overline{E} = \varepsilon_0 \mu_0 \frac{\partial^2 \overline{E}}{\partial t^2}. \qquad (1.6)$$

A similar result holds for the magnetic field. Comparison with the well known wave equation shows that the electric and magnetic fields must indeed be waves, propagating through space at a speed $\frac{1}{v^2} = \varepsilon_0 \mu_0$; put more simply the waves travel through a vacuum at the speed of light $c = \frac{1}{\sqrt{\varepsilon_0 \mu_0}}$.

A more thorough analysis can be carried out by assuming that these waves are in fact plane waves, the simplest solutions admitted by a generalised wave equation. For an electric (or magnetic) wave $\overline{E} = \overline{E}_0 e^{i(\bar{k} \cdot \bar{r} - \omega t)}$, one finds that $k^2 = \omega^2 \varepsilon_0 \mu_0$, and thus the

group velocity, $v_{gp} = d\omega/dk$ and phase velocity, $v_{ph} = \omega/k$, by definition are identical and equivalent to the speed of light, $c = 1/\sqrt{\varepsilon_0 \mu_0}$.

More generally, in a linear, isotropic, homogeneous medium the first and fourth Maxwell equations become:

$$\nabla \cdot \overline{E} = \frac{\rho_{free}}{\varepsilon}, \qquad (1.7) \qquad \nabla \times \overline{B} = \mu\sigma\overline{E} + \mu\varepsilon\frac{\partial \overline{E}}{\partial t}. \qquad (1.8)$$

Here: ρ_{free} is the charge density due to electrons and ions, which is usually taken to be zero; $\varepsilon = \varepsilon_{rel}\varepsilon_0$ and $\mu = \mu_{rel}\mu_0$ are the absolute permittivity and permeability of the medium respectively; and σ is the conductivity. Elimination of either the electric or magnetic component, in a similar way as the vacuum case, once again realises a wave equation:

$$\nabla^2 \overline{E} - \mu\sigma\frac{\partial \overline{E}}{\partial t} - \mu\varepsilon\frac{\partial^2 \overline{E}}{\partial t^2} = 0, \qquad (1.9)$$

with identical results holding for the magnetic field, $\overline{B}$ and the magnetic field intensity $\overline{H} = \overline{B}/\mu_0$. These equations are again wave-like, and their simplest solutions are plane waves. This time $k^2 = \varepsilon\mu\omega^2 - i\mu\sigma\omega$.

For poor conductors, $\sigma << \varepsilon\omega$ and $k^2 \sim \varepsilon\mu\omega^2$. The group and phase velocities are identical and are found to be $v_{gp} = v_{ph} = 1/\sqrt{\varepsilon\mu}$. In fact, $v = c/n$ where n is the refractive index of the medium, which by definition is $n = c\frac{k}{\omega}$. For a non-magnetic material, $(\mu = \mu_0)$ the refractive index is $n = \sqrt{\varepsilon_{rel}}$. Thus the wave speed is slower in poor conductors compared with a vacuum. Good conductors on the other hand have $\sigma >> \omega\varepsilon$, so $k^2 \sim -i\mu\sigma\omega$, which means that k is complex: $k = k_r - ik_i$, with $k_r = k_i = 1/\delta = \sqrt{\mu\sigma\omega/2}$. The plane wave is thus attenuated and its general solution becomes $\overline{E} = \overline{E}_0 e^{-\bar{r}/\delta} e^{i(\bar{r}/\delta - \omega t)}$, where δ is the skin depth. Calculation of the phase and

group velocities yields $v_{ph} = \sqrt{2\omega/\sigma\mu}$ and $v_{gp} = 2v_{ph}$. Using the standard definition of refractive index, we find $n = c\frac{(1-i)}{\omega}\sqrt{2\omega/\sigma\mu} = n_r - in_i$, with n_r and n_i being equal.

More generally, for materials which are neither good nor poor conductors, for example dielectrics, the full expression for the dispersion relation must be considered. This means that the permittivity is necessarily complex, which will generally be the case for the interaction of terahertz waves, with which we are concerned. If the medium is non-magnetic, the refractive index is $n^2 = \frac{c^2}{\omega^2}(\omega^2\mu_0\varepsilon - i\mu_0\sigma\omega)$, which can be written: $n^* = \sqrt{\varepsilon_{rel}}$, $\varepsilon_{rel} = \varepsilon_r - i\varepsilon_i$. This notion of complex permittivity takes absorption within the medium into account. The interaction of terahertz radiation with dielectrics will be discussed more fully in chapter two.

Electromagnetic waves were first discovered in the laboratory by Hertz in 1886/7. His discovery verified that the electromagnetic waves predicted by Maxwell do exist and can propagate through media. Hertz generated these EM waves using a spark gap oscillator and detected them using a simple loop antenna, which had a small spark gap. In further experiments, Hertz managed to measure the velocity of these electromagnetic waves, finding it to be the same as that of light. He also showed that this radiation has all the properties (reflection, refraction, polarisation, interference) of light. Thus, the work of Hertz proved that light is an electromagnetic wave, governed by Maxwell's equations.

1.4 An overview of the history of terahertz radiation

Exploration of the terahertz region has an interesting history of development, and its origins can be traced back to the early part of the 19th Century: it was Herschel who made the first quantitative measurements of the heating power of the Sun in 1800[1]. By refracting waves from the Sun, both visible and invisible, he was able to show that: all colours of visible light; and invisible waves beyond the red end of the visible part of the spectrum produced a heating effect. These invisible rays are of course now referred to as infrared radiation. Herschel also noted that rays beyond the violet end of the visible spectrum (ultraviolet) did not produce a heating effect. Of course, the history of

experiments undertaken on visible light can be traced back much earlier through the work of e.g. Fermat and Newton.

It then was not until the work of Rubens and Nichols in the latter part of the 19th Century that interest was once again ignited in the far infrared, or terahertz region of the electromagnetic spectrum[2]. Writing in 1897 they acknowledged that a gap existed between electrical waves and light waves, even though work earlier in the century had indicated that they are one and the same phenomena. In the intervening period since Hertz's discovery of radio waves, good progress had been made in shortening the wavelengths of electronic oscillations with rather less success in the production of longer heat waves. On this point they noted that "*the great difficulty which accompanies the study of infra-red waves of great wavelength is that the rays form only the minutest part of the total energy emitted by the flame or incandescent body used as a source.*" Their work centred around using a fluorite prism to separate these long wavelength rays from those that both overlap and conceal them.

At this point in time much effort was also being put into trying to explain the black-body spectrum of radiation. Figure 1.3 shows the spectrum of radiation emitted by a black body at various temperatures. It was known that the spectrum was both universal

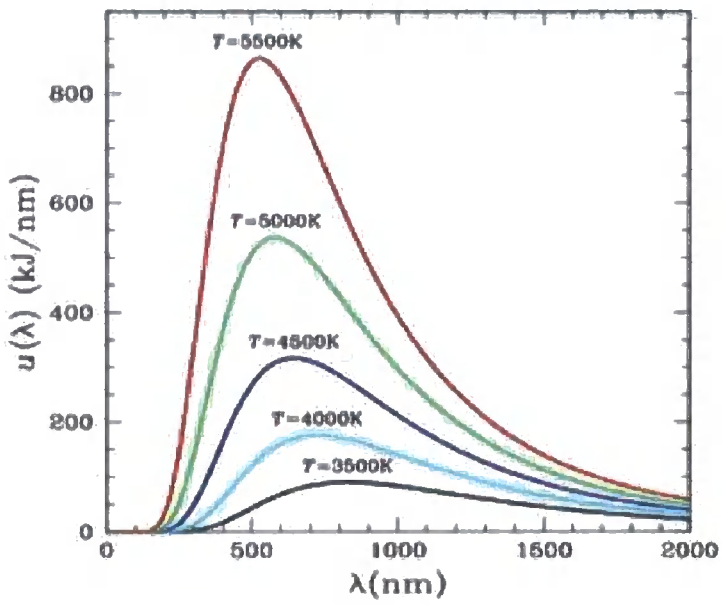

Figure 1.3: Energy density of a black body spectrum of radiation at various temperatures.

and dependent upon the temperature of the radiation, and numerous empirical relations had been developed to describe it. For example: Wien's displacement Law $\lambda_m \sim 1/T$, that relates the wavelength at which most of the energy is radiated by an object to its temperature; and the Stefan-Boltzmann Law that gives the power radiated per unit area for a black body as $R = \sigma T^4$. However, application of methods from Classical Physics in an attempt to calculate the energy density of the black body led to what has become known as the ultra-violet catastrophe. Classically, the energy density can be calculated as $u(\lambda) = \frac{8\pi}{\lambda^4} kT$, known as the Rayleigh-Jeans formula, which incorrectly predicts an exponential increase in the energy density at short wavelengths.

Many of the problems with fitting the black body spectrum actually arose from the lack of accurate experimental results at long wavelengths, or the far infrared. However, in 1900 Rubens provided Planck with accurate data of the spectrum of a black body out to long wavelengths and that same evening Planck wrote down the first form of his now famous radiation formula:

$$u(\lambda) = \frac{A}{\lambda^5 (e^{B/\lambda T} - 1)}. \tag{1.10}$$

This correctly predicts the black body energy distribution over all wavelengths. However, Planck initially wrote this equation down as a hunch without any formal justification. Eight weeks or so later, in an act of desperation to justify his formula, Planck asserted that the energy of an oscillator must be quantised in units $E = nhf$, which paved the way for the birth of Quantum Mechanics! Quantisation shows that the energy density is in fact,

$$u(\lambda) = \frac{8\pi}{\lambda^4} \left(\frac{hc/\lambda}{e^{hc/\lambda kT} - 1} \right). \tag{1.11}$$

Investigation of the far infrared part of the spectrum continued apace during the early part of the twentieth century and, during the 1920's, sources were developed to bridge the whole of this part of the spectrum. Work undertaken by Arkadiewa in 1924 succeeded in producing waves with wavelengths ranging between 50 mm and 82 μm,

using a number of small Hertzian oscillators as opposed to one large one[3]. These rays overlapped the shortest waves (wavelength 1.8 mm) produced using interferometric methods by Nichols and Tear in 1923[4] and the longest heat rays (wavelength 420 μm) generated by Rubens and Baeyer using a mercury arc lamp in 1911[5].

Between the end of the 1920's and about 1960, the main developments in the field centred around detectors with the first realisation of, amongst others, the Golay cell[6], which is still used today. In the 1960's work in the far infrared started to become commonplace once more, with: the re-birth of Raman Spectroscopy; and the advent of more powerful computers, that allowed interferometric spectroscopic techniques to be used. However, it has really been the advent of optoelectronic devices, switched by ultra fast lasers, that has led to the explosion of THz research as we know it in the last twenty or so years. These methods have fuelled the development of sources in the region that are both bright and relatively easy to use coupled with efficient detection techniques. It is this type of experimental system that has been used to undertake the work in this thesis. For a more thorough discussion of the history of the terahertz region and recent progress in closing the terahertz gap with optoelectronic methods, see the review articles by Kimmitt[7] and Chamberlain[8].

1.5 Applications of terahertz radiation

Terahertz systems commonly available in the laboratory and commercially, are usually driven by short pulses of near infrared light and thus produce short pulses of THz radiation. These pulses contain frequency components extending over a broad spectral range, typically from a few hundred gigahertz up to approximately 4 THz, but specially configured systems operating out to 30THz have also been reported.

Terahertz radiation also has the following desirable attributes: it is low in energy, so is thus non-ionising; it propagates freely through many (non-metallic) materials; the THz region is the highest frequency range where both the amplitude and phase of the radiation can be measured simultaneously and thus the electric field of the pulses recorded; THz radiation is also longer in wavelength than the near infrared part of the spectrum, so undergoes less scattering, but yet still provides adequate resolution for many imaging applications. Conversely, terahertz radiation is readily absorbed by

water, because water is a polar molecule; this limits its range of application to some degree.

Utilizing the above properties has allowed two basic types of THz system to be built: one that can be used as a tool to identify objects by investigating their characteristic spectra; the other as an imaging tool, whereby raster scanning of the beam across the sample allows a profile of the sample to be built up. Of course, these properties can also be combined within a single THz system. Below is a brief description of the two individual techniques, terahertz spectroscopy and terahertz imaging. Both of these systems contain a coherent detection mechanism and hence these THz systems have a great sensitivity.

1.5.1 Terahertz spectroscopy

The broad spectral range of a terahertz pulse contains photons having a wide variety of energies $\sim 1-15$ meV. Characteristic energies of specific internal processes for many materials fall within this range because many of them are made from biological and organic molecules that have intra-molecular motions on this energy scale. As a result, particular components of the pulse can excite various vibration, torsion and breathing modes within the sample causing resonances to occur. Since THz spectroscopy measures both the amplitude and phase of the THz wave that has interacted with the sample, the sample refractive index and absorption coefficient can easily be calculated without having to resort to a complex Kramers-Kronig analysis. Using the pulsed nature of the sources also allows time resolved measurements to be undertaken: THz radiation can be used to "watch," on a short time scale, how a sample changes with time; or how a sample responds and decays after excitation by another form of radiation.

1.5.2. Terahertz imaging

Scanning either a terahertz beam across a sample, or the sample across the terahertz beam, allows an image to be built up pixel by pixel. The image can be built in one of two ways by either: transmitting the THz pulse through a sample; or measuring the THz radiation reflected from a sample. The value of each pixel is related to the shape of the transmitted or reflected sample pulse relative to some reference pulse. Possible pixel measurements include: pulse width; amplitude; time delay; or an absorption image that

can be built up by averaging the sample's absorption over a particular frequency range. Terahertz imaging has been reviewed by both Chan *et al*[9] and Mittleman *et al*[10].

Use of the above two systems has allowed THz radiation to find numerous uses in a variety of diverse applications. Outlined below are just some of the areas were THz radiation has both found uses and where the potential exists for commercial exploitation.

Security: Using the ability of terahertz to propagate through barriers, for example clothing and packaging, coupled with the identification possibilities of THz spectroscopy, has allowed THz radiation to be used as a tool to identify drugs of abuse and explosives[11, 12]. Broadband THz sources are particularly useful for this application, since they can probe a wide number of spectral features and provide an accurate method of determining the substance.

Work by Kemp has shown that the spectra of common explosives retain the spectral features of the individual components[13]. Shen *et al* have combined spectroscopy with imaging: a pellet of explosive is raster scanned across a THz beam and then each scan undergoes Fast Fourier Transformation to provide an absorption spectrum[14]. Using this information allows the spatial distributions of individual chemical species within the pellet to be mapped out. Work by Burnett *et al* has concentrated on building a library of spectra of drugs and explosives using both THz and Raman spectroscopy over a wide range of temperatures[15]. However, it is also known that until more compact, powerful sources can be found, with powers in excess of 100 mW, THz stand-off detection systems are just not plausible[16].

Biomedical Spectroscopy: Again, the spectral features of various compounds of medical interest can be identified using terahertz methods. Photons of terahertz radiation have an energy that is typical of the excitation energies for many biological processes, such as: proton tunnelling for enzyme active sites[17]; the collective motion of Deoxyribonucleic Acid (DNA) base pairs along the hydrogen bonded backbone[18]; protein conformational changes[19]; the vibrational energy of cell membranes[20]; or the nonlinear thermal fluctuations that may be responsible for the initiation of DNA transcription[21].

Terahertz has been used to characterise plant oils and animal fats and to detect changes in the binding of molecules, a precursor for detecting protein changes. Markelz *et al* have investigated the low-frequency collective vibrational modes of various bio biomolecules[22]. Work by Brucherseifer *et al*[23] has investigated mutations along the hydrogenated backbone of DNA and this has further been developed using on-chip methods by Nagel *et al*[24].

Biomedical Imaging: The area of biomedical imaging in general is developing apace and new and improved imaging modalities are always being sought. Pulsed terahertz sources are particularly attractive in that they combine a method of producing an image with the ability to identify substances of biological interest using spectroscopy. The earliest work in this particular field by Arnone *et al*[25] concentrated on looking for caries, the initial signs of tooth decay. If they can be treated at an early stage it prevents the need for more painful drilling. This work used the fact that the refractive index differs between enamel and caries and the resolution afforded by THz radiation allows them to be seen earlier than they would be with the naked eye. Further work has been undertaken in an attempt to characterise the refractive index of enamel and dentine[26].

Other work has concentrated on defining the limits of cancer, and in particular Basal Cell Carcinoma, the most common form of skin cancer[27, 28]. Even though THz radiation only penetrates a few millimetres of skin, it provides enough information to put a far more accurate limit on the extent of the disease than can be seen on the surface alone: it is thought that the contrast difference arises from the difference in water content between healthy and cancerous tissue[29]. THz radiation has also recently found a use for mapping the margins of tumour in recently excised breast tissue, so that surgeons can check that the whole tumour has been removed in one operation[30]. For a more thorough discussion of biomedical applications, see the review by Pickwell and Wallace[31].

Semiconductors: An understanding of the carrier dynamics of semiconductors is important on both a scientific and technical level, with most interesting phenomena centering around the plasma frequency and damping rate. Both of these frequency regimes tend to correspond to energies of sub-millimetre wavelength and hence

terahertz pulses provide an attractive way to measure the various properties of semiconductors.

Grischkowsky *et al* have undertaken work to measure the absorption and dispersion due to carriers in silicon, and have also used reflection spectroscopy to measure the complex conductivity of optically dense wafers[32, 33]. Other reflection measurements, that provide an accurate measurement of the terahertz pulse phase, have also been undertaken[34]. Optical pumping, employed with terahertz probe methods, has been used to measure the transient photoconductivity of GaAs, as well as sub-picosecond dynamics of LT-GaAs by Schmuttenmaer[35, 36].

Microscopy: It is a well known fact that the resolution of any system is limited by the wavelength of the illuminating light. One immediate consequence of this is that the resolution of pulsed terahertz imaging, using broadband sources, will be limited by the spectral range over which the signal is integrated. Just using the high frequency components of a signal is not a good option here, because the signal to noise ratio is limited at these frequencies. However, it is possible to undertake terahertz imaging below the diffraction limit. This can either be done with or without an aperture.

Hunsche *et al*[37] were the first group to report microscopy using an aperture with a sub-wavelength conical tip. When apertureless microscopy is performed, a sharp tip is passed over the surface being imaged by the beam, which locally distorts and reconcentrates the terahertz field[38, 39].

1.6 Structure of this thesis

The order of work presented in this thesis is as follows. Chapter two is an in depth description of terahertz radiation, including methods used for both its generation and detection and a description of the Durham terahertz transmission set-up. Chapter three is an investigation of the propagation, in particular the transmission, of terahertz radiation in random structures. The mathematical models developed to describe how terahertz radiation propagates through materials of a random nature, containing structures on a scale comparable to that of a terahertz wavelength, are discussed. A comparison is then given between the results of this modelling and experimental measurements of THz propagation through various phantoms. A description of the development of signal processing methods to "clean up" a terahertz signal, and thus

glean more valuable information from the pulse is given in chapter four. These algorithms are then validated using: transmission and reflection measurements from a void mimicking sample; and the response of molecules impulsively excited by a terahertz pulse.

During the course of the PhD an experimental system with the capability to measure THz radiation scattered by various phantoms was built. This requires fibre-fed detection. Chapter five describes the construction of this system, including a description of near infrared pulse propagation in optical fibres. The information contained in scattered THz pulses can be used to build up a tomographic image of structures being illuminated by the radiation and this work is described in chapter six. The final chapter of the thesis summarises the work undertaken and speculates on ideas for the future development of the terahertz technology used in this programme of work.

2. Terahertz radiation

This chapter of the thesis is concerned with describing the various methods which exist for the generation and detection of terahertz radiation. As already stated in Chapter one, the terahertz region of the electromagnetic spectrum, broadly defined as covering 300 GHz to 30 THz, lies between microwaves and infrared. Unfortunately, this is the part of the spectrum where the transition between electronic and optical methods for generating bright sources of radiation overlaps. The changeover does not happen at a distinct frequency, but instead occupies a range of frequencies.

The first part of the chapter is a discussion of the wide variety of sources that have been developed to generate terahertz radiation in recent years. A more detailed description of photoconductive emitters, used for the experimental work in this thesis is then given, followed by a discussion of terahertz detection techniques. Combination of these techniques results in what is known as a terahertz time domain spectrometer. Such a system is outlined, before a discussion is given of how this can be used to determine the response of the sample to terahertz radiation.

2.1 Terahertz sources

In the past twenty or so years, numerous sources have been developed to bridge the so-called 'terahertz gap' of the electromagnetic spectrum[8]. These can be split into three main groups: those that produce the radiation by electronic means, coming from the low frequency end; those that use some sort of lasing mechanism to emit radiation, from the high frequency end; and those that use what are known as optoelectronic techniques. It is optoelectronic techniques that are most commonly used for terahertz experiments today, and it is this source and detector technology that has been used in all of the experimental work undertaken in this thesis.

2.1.1 Electronic sources

These sources are an attempt to bridge the terahertz gap from the low frequency (electronic) side of the electromagnetic spectrum, and include Gunn diodes, field effect transistors and bipolar transistors. The maximum frequency of their operation is limited by a number of fundamental solid-state principles: the characteristic transit length that electrons must oscillate along; the saturation velocity of the carriers; and the maximum

electric field that can be sustained in the device before break down. Applying a simple argument, see Chamberlain and Miles[40], shows that the power decreases with the square of the frequency, and the maximum operating frequency of these devices is approximately 0.7 THz. Higher frequencies can also be generated electronically by the use of multiplier devices, such as the Schottky diode. In principle, an unlimited frequency can be reached by stringing a number of these devices together, but in practice the highest obtainable frequency is limited by: the physical size of a number of devices in series; and the increase in initial pump power required if a useful output is to be obtained.

2.1.2 Lasing sources

A laser (Light Amplification by Stimulated Emission of Radiation) is a device that produces a strong beam of coherent photons using the phenomena of stimulated emission. Here, excited atoms in a medium are illuminated by photons having energy equal to the difference between the excited and some lower energy state. This causes stimulated emission, with the emission of another photon in phase with the incident one. To work, a laser requires the following three features: a gain medium, having suitable energy levels, in which a population inversion can be obtained; a pump source (source of energy); and a resonant optical cavity that implements a positive feedback between the emitted light and the amplifying medium[41]. Figure 2.1 shows a very simple block diagram of the combination of the above features to produce a laser.

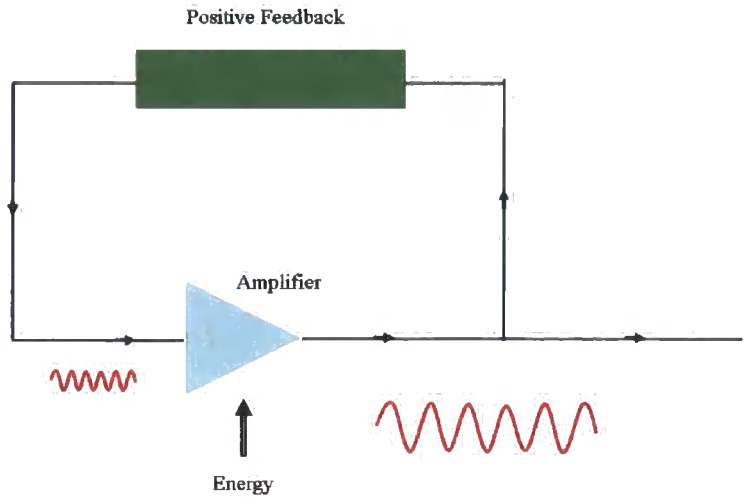

Figure 2.1: Overview of the building blocks of a laser.

In a laser, some active medium is illuminated by a pump source of radiation, resulting in a population inversion. Stimulated emission then forces the excited atoms to decay. By enclosing the active medium in a cavity, photons pass through it many times causing more and more stimulated emissions. This results in the eventual emission of an amplified and coherent beam of photons.

Within a laser cavity, the electric field oscillates transversely to the direction of propagation. However, there also exists a set of longitudinal modes within the cavity that are a time-frequency property, which arise because of the high field intensity within the cavity. The modes exist only if there is constructive interference between the two waves propagating in opposite directions within the cavity, thus creating a standing wave[42]. If the cavity is of length L, and the period of this wave is τ, then $mc\tau/2 = L$ for any integer, m. The cavity has specific period $T = m\tau = 2L/c$, which is also the time of flight of one round trip. Since a large number of longitudinal modes exist along the cavity, at frequencies $\nu_m = 1/T = c/2L$, it can be used as a resonator.

When a laser operates in its usual, continuous wave regime, the amplification is linear and coherent with gains balancing the losses. At any point in the cavity the field observed at some instance will be repeated after time T, i.e. $\varepsilon(\tau) = \varepsilon(\tau + nT)$. The power spectrum can be calculated as:

$$I^N(\omega) = \frac{\sin^2(N\omega T/2)}{\sin^2(\omega T/2)} I(\omega), \qquad (2.1)$$

where N is the number of periods.

Lasers were initially built to operate at microwave frequencies (the Maser): it was Gordon *et al* who first showed that it was possible to weakly amplify microwaves by stimulated emission in ammonia gas in 1955[43]. Surrounding the amplification medium with a suitably sized metal box provided the necessary feedback for the amplification system to run as a single mode oscillator. Further work was then carried out to try and move the lasing frequency into the visible regime, but since the enclosing box dimensions need to be of the order of a few wavelengths, this meant constructing a box of volume 0.1 μm^3, which was and still is just not possible. However, further work led

to the realisation that a reduction in the number of modes could be reached by confining the light to one direction[44]. Enclosure of the gain medium between two mirrors allows a coherent beam to be built up after a few round trips. In such a system, stimulated emission is created by the spontaneous emission of one photon along the cavity axis after a population inversion has been created. Maiman provided the first report of an operational laser, in 1960[45], which was closely followed by the production of the first gas laser in 1961[46].

Three types of basic laser technology exist: gas, solid state and semiconductor. A gas laser produces laser light by the excitation of some sort of gas via an electric discharge. In a solid state laser, a crystal is optically excited, whilst in a semiconductor laser a semiconductor crystal is excited electrically. Various technologies have been investigated as a way of producing lasing at terahertz frequencies and they are described below.

Molecular gas lasers: This type of source has been around in one form or another since the 1960's, the maser being one such example[47]. However, they are both large and costly and their emission wavelengths are limited to transitions between the energy states.

Free electron lasers: These sources are only available at central research facilities and produce very high output powers of radiation. In fact, they are the brightest sources of terahertz radiation available. They are often based on synchrotron technology: electrons that are accelerated around a ring emit what is known as synchrotron radiation. The fourth generation light source, planned at Daresbury will have a number of dedicated THz beams: these will mainly be used in the study of systems of biological interest.

Quantum cascade lasers: These lasers provide a method of lasing at terahertz frequencies using semiconductor engineering techniques. Conventional semiconductor laser methods for generating terahertz radiation do not exist. This is because the average photon energy in the THz region (of the order of a few meV) is much smaller than the band gap in a typical semiconductor, which is of the order of a few electron volts. In fact, this average photon energy is comparable with the thermal energy at room temperature. Therefore thermal effects alone are enough to excite electrons from

the valence to the conduction bands in such a semiconductor. The difference between Quantum cascade lasers (QCL's) and conventional semiconductor lasers is that QCL's emit photons which have been generated within the conduction (or valence) band. In other words, sub-band transitions are used, and this makes the lasers unipolar: they only operate using one type of carrier (electrons or holes), as opposed to a bipolar conventional semiconductor laser, which emits photons when electrons and holes recombine. Since sub-band transitions are used, the energy of the emitted radiation is independent of the intrinsic material properties.

Quantum cascade lasers are grown using the well established semiconductor technique of molecular beam epitaxy (MBE). A structure is grown containing numerous regions, and various layers exist within each region. Band structure engineering is used to design the individual layers such that they have different bandgaps. Each layer is a few nanometres thick, which is of the same order as the de-Broglie wavelength of the emitted photons and therefore quantum mechanical effects come into play. The low bandgap areas become quantum wells and the high bandgap areas barriers. Electrons are thus confined to the wells, having discrete energy levels, but they also have a finite probability of tunnelling through the barriers.

The simplest type of QCL contains N regions, each having a three level energy band structure. Electrons are injected into the highest energy level through a quantum barrier by resonant tunnelling. On emission of a photon, the electrons de-excite to the intermediate level, from which they can escape to the lowest energy level. Resonant tunnelling of the electrons then takes place between this energy level and the highest energy level of the next region and the process repeats down the N periods. Thus the injection of one electron leads to N emitted photons. Providing the resonant tunnelling from the injecting region to the highest level and the transition from the intermediate level to the lowest level is extremely fast, a population inversion is maintained. Consequently, level #3 is kept full of electrons whilst level #2 is effectively empty.

Initially, QCL's were developed to operate in the mid infrared region of the spectrum[48], but work by Köhler *et al* in 2002 led to the production of the world's first terahertz QCL[49]. In the intervening period, work has been carried out to: lower the frequency of lasing; and increase the temperature at which these devices operate, see the paper by e.g. Tredicucci for a review[50]. Currently, QCL's have been reported operating at a frequency of 1.39 THz in an applied magnetic field[51], a frequency of 1.6 THz in the absence of magnetic field[52] and at a maximum temperature of 164 K, albeit

at the higher frequency of 3.0 THz[53]. A recent private communication has indicated that the lowest possible lasing frequencies are now 1.2 THz in zero field and 0.8 THz in an applied one[54].

2.1.3 Optoelectronic sources

Work that initially began in the 1970's showed the ability of optoelectronic techniques to produce short pulses of radiation. Here, one form of radiation, typically laser light, is converted to another form using some sort of transducer device, most often a semiconductor. Two basic methods exist for generating terahertz radiation in this way: photoconductive sources, which have been used to generate the THz radiation used in all experiments undertaken in this thesis; and non-linear frequency mixing. Photoconductive sources tend to be of higher power, whereas it is easier to generate much higher frequency components using non-linear frequency mixing.

Photoconductive sources: Work by Auston in the 1980's demonstrated that sub-picosecond single cycles of radiation could be both generated and detected using semiconductor devices excited by short pulses of radiation[55]. The idea is actually based on work by Hertz, who realised that a transient polarisation, for example a spark, can create a current surge that can act as a source to radiate electromagnetic waves. If this polarisation transient is not oscillatory, but is in fact a rapid change, caused by for example a pulse, then the radiated wave has no well defined frequency. Instead, the wave occupies a broad spectrum, with the frequency component having maximum amplitude being proportional to the inverse of the time scale of the incoming pulse. All work undertaken in this thesis used such sources, so a complete overview of their history and physical properties is given in section 2.2.

Non-linear frequency mixing: This technique is rather similar to photoconductive sources in that radiation of one frequency is converted to another using some sort of non-linear medium. If a high intensity laser beam is incident on a non-linear medium, mixing of the modes can lead to the generation of new colours.

The polarisation of a non-linear material can be described by a Taylor expansion of the incident field:

$$P(t) = \chi^1 E(t) + \chi^2 E(t)^2 + ..., \qquad (2.2)$$

where the second term describes the non-linear properties of the material, which come into play when the intensity of the electric field is high enough. Excitation of the medium by a short pulse, $E(t) = A(t)\cos(\omega_0 t)$, where $A(t)$ is the pulse envelope and ω_0 is the carrier frequency, allows the non-linear term to be written as the sum of two terms: one responsible for second harmonic generation; and the other describing the average value of the induced polarisation over one cycle. This second term is only proportional to the pulse intensity, $A(t)^2$ and therefore only points in one direction, so the medium is known as an optical rectifier in analogy with the well known electronic device. Optical rectification of a short pulse, having a time-dependent intensity, generates a transient polarisation[56]. The spectrum of the pulse generated by this method contains all possible difference-frequency mixings from among the incident spectral components, and consequently a short incident pulse, containing a broad range of frequencies, will generate a broad spectrum in emission; but since the process relies on the non-linear coefficients it is not very efficient. It has been shown that frequencies in excess of 50 THz can be generated using phase-matched optical rectification, and the phase matching increases the efficiency[57].

Both of the above optoelectronic sources require excitation by some other frequency of radiation, and here ultra short laser pulses are used. It really was the manifestation of this technology, more specifically the ability to self-mode lock lasers in 1991, that has led to the explosion in terahertz research in the last fifteen or so years[58].

2.1.4 Ultrafast lasers

Ultrafast lasers are one of the most exciting and useful developments in the relatively short history of the laser. They are used to produce short pulses of light, at a high repetition rate, which in turn can be used to generate THz radiation by optoelectronic methods.

Short light pulses: As a consequence of the uncertainty relation, a short pulse of light must contain a large number of spectral components. To see this, consider a light pulse, which can be regarded as the product of a plane wave and a Gaussian function, whose spectral content can be calculated by Fourier Transformation. The Fourier Transform of a plane wave, which is monochromatic, is a delta function, whilst the Fourier

Transform of a Gaussian function is also Gaussian. Thus, using the property that the Fourier Transform of a product is equivalent to the product of the individual Fourier Transforms, a Gaussian pulse of light must necessarily have a Gaussian Fourier Transform. In other words, a light pulse has larger spectral content than the single frequency of a plane wave. In fact, a light pulse of given duration must occupy a broad enough spectral width.

Starting from the general time and frequency Fourier Transformations of a pulse:

$$\varepsilon(t) = \frac{1}{2\pi}\int_{-\infty}^{\infty} E(\omega)e^{-i\omega t}dw, \qquad E(\omega) = \int_{-\infty}^{\infty} \varepsilon(t)e^{i\omega t}dt, \tag{2.3}$$

and then by calculating its duration and spectral width via the standard statistical definitions, the inequality $\Delta t\Delta\omega \geq 1/2$ can be found[59]. The equality only holds for a transform limited pulse, which must be Gaussian; such a pulse occupies a minimum number of spectral components. Since it is experimentally easier to measure widths of pulses at their half maxima, the relation used in practice is:

$$\Delta\nu\Delta t = K, \tag{2.4}$$

where K is a constant dependent upon the shape of the pulse assumed. For example, a Gaussian pulse has K=0.414, with K being greater for any other pulse shape. For a given frequency spectrum, only one possible pulse envelope can be constructed having the shortest possible duration, and this can only be transform limited if the spectrum is symmetrical.

It should also be noted that when a light pulse propagates through a medium it undergoes phase distortion due to group velocity dispersion across a wide bandwidth of frequencies. Thus, the pulse becomes longer in time, and gains what is known as a positive chirp, whereby the leading edge of the pulse becomes redder whilst the trailing edge becomes bluer. The wide bandwidth associated with optical pulses allows non-linear effects in crystals to be investigated using relatively low intensity, short light pulses. Pulse propagation in transparent media is discussed more fully in chapter five.

Given that very short pulses of light must occupy a broad spectrum, the natural question that immediately arises is 'How can a laser generate short pulses, given the frequency selection that the laser cavity imposes?' It is true that in general, a laser only oscillates around a few frequency domains, centred on the discrete resonances of the cavity,

$\upsilon_q = {}^{qc}/_{2L}$. However, if a laser operates in its multimode regime its output is no longer constant in time. It becomes dependent upon the phase relation between the modes and, if the modes of the laser can all be made to oscillate in phase, the output of the laser becomes the periodic repeat of a wavepacket.

Pulsed Lasers: A laser operating in its most usual regime oscillates simultaneously over all the allowed resonant frequencies in the cavity which have gains greater than the losses. In other words, it oscillates over all the longitudinal modes. This results in the output intensity being non-constant in time. However, if the phase relations between these modes can be locked, the laser output becomes pulsed. This can easily be seen by considering the following scenario. For a pulse of light containing n modes at angular frequencies ω_i, which have identical phase at some time $t = 0$ and are of equal amplitude E, the ith mode can be described $E_i = E\sin(\omega_i t)$. The total electric field amplitude at $t = 0$ is then $E_T = nE$, since all the modes are aligned. If the modes are regularly spaced in frequency, such that $\omega_{i+k} - \omega_i = k\Delta\omega$, for $k \in Z$, then the amplitude of the wave goes to zero after a time $\Delta t = \frac{2\pi}{n\Delta\omega}$. Further at a time $T = \frac{2k\pi}{\Delta\omega}$, the wave once again reaches maximum amplitude. Thus the laser output becomes pulsed, repeating with period T, with the pulses going to zero at a rate inversely proportional to the number of modes. Therefore, the larger the number of modes in the pulse, the shorter the time in which the pulse takes to go from maximum to minimum amplitude.

For a laser cavity of length L, the resonant frequencies are $\omega_q = \frac{2\pi qc}{2L}$, for $q \in Z$, and the laser produces a periodic succession of pulses, at repetition rate $T = \frac{2L}{c}$, each lasting for a time $\Delta t = \frac{2\pi}{n\Delta\omega}$. Thus, the larger the number of modes the cavity admits the shorter the length of the optical pulse. If the modes in the cavity constructively interfere at some point, they must destructively interfere at all other points, because their wavelengths are all slightly different. Therefore, if the maximum amplitude is at a certain point, destructive interference causes the amplitude to be zero everywhere else in the cavity, except a short distance away from this point; moreover the greater the number of modes, the shorter this distance will be.

Slightly more rigorously, for a laser with an infinite number of phase-locked modes, the total electric field is:

$$E(t) = \sum_{-\infty}^{\infty} E_n \exp(i\omega_n t), \tag{2.5}$$

where $\omega_n = \omega + n\Delta\omega$, $\Delta\omega$ being the frequency interval between adjacent modes. The amplitude can also be written as:

$$E(t) = \exp(i\omega_0 t)\sum_{-\infty}^{\infty} E_n \exp(in\Delta\omega t), \tag{2.6}$$

which is a carrier wave of frequency ω_0, modulated by a time varying function $k(t) = \sum E_n \exp(in\omega t)$. The intensity of the laser pulse is:

$$< I >= E(t)E^*(t) = k^2(t) \tag{2.7}$$

which must necessarily also be periodic.

Mode-locking of lasers: It has just been shown, that if the phase components of the laser can be locked, the laser's output becomes pulsed. When a laser is mode-locked, all the energy in the cavity becomes concentrated in one pulse. In its most usual mode of operation there is a competition between the modes that the laser is trying to amplify, which leads to fluctuations in the mode phase and amplitude. Selection of one intensity maximum with time is equivalent to establishing a phase relation between the longitudinal frequency modes and this causes the laser output to become pulsed. There are three basic techniques that can be used to achieve this and lock the phase relations of the modes in a laser. These are active, passive and self mode-locking.

In active mode-locking, an element is inserted into the laser cavity which induces a modulation to the amplitude of each mode. The frequency of this applied modulation is either that of the cavity losses or of the gain of the amplifying medium. To achieve passive mode-locking, a saturable absorber is inserted into the lasing cavity. The association between the absorbing medium and the dynamics of the gain saturation in the amplifying medium, which can distort the pulse, can naturally mode-lock the laser output. Within a self mode-locked laser the non-linear properties of the amplifying medium are so great that the modes are able to lock without an external influence. For this to happen, the pulse must narrow on each of its round trips through the medium. This phenomenon was first observed accidentally in a Ti:sapphire laser, when a jerk of the optical bench caused the laser output to become pulsed[58].

Ti:sapphire lasers: All experimental work undertaken in this thesis uses a self mode-locked Ti:sapphire laser as the light source. It is this technology that has seen the greatest recent advances in producing short pulses of light. In fact, it took little over a year from the first report of mode-locking using such a crystal by Spence *et al* in 1991[58] to the publication that pulse lengths shorter than 50 fs could be produced using this technology[60]. Pulses shorter than 10 fs in duration can be produced using optimized configurations, but in general, commercial systems are available that produce pulses shorter than 100 fs and of average power in excess of 1 W. Therefore no extra amplification is required, and the system is "easy" to use.

A crystal of Titanium:sapphire [$Ti:Al_2O_3$] has a very wide absorption band in the blue-green part of the spectrum because the titanium atoms are much larger than the aluminium ones. This causes a distortion to the crystal, creating a strong electric field. This field splits an excited atomic state of the crystal into two sub-levels, separated by 50 nm. These crystals provide both very good tunability of the frequency of continuous wave emission and, since sapphire has a very high thermal conductivity[61], such crystals can be pumped with very high powers. Figure 2.2 shows a schematic of a general Ti:sapphire laser. In this laser, the crystal is pumped via a continuous wave argon ion laser through a dichroic mirror, M1. The birefringent filter determines the central wavelength of the pulsed emission, whilst the two prisms compensate for group velocity dispersion in the cavity.

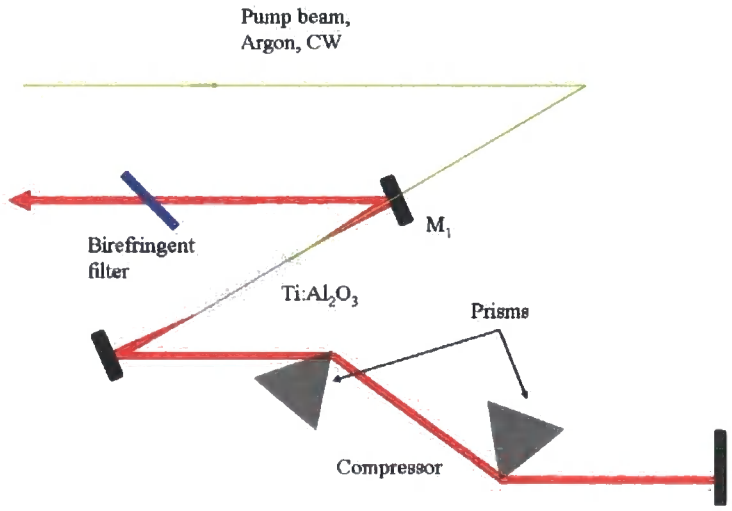

Figure 2.2: Schematic of a Ti:sapphire laser.

These lasers can be mode-locked in numerous ways, but it is their ability to self mode-lock, using the Kerr lens effect, that has made them so useful. For Kerr lensing to take place: the pulsed regime must be more favourable than the continuous regime within the medium; the overall system must posses the property of shortening pulses; and some mechanism must be present to self initiate the mode-lock. In a Ti:sapphire laser, the Kerr effect focuses the higher intensity modes within the crystal, which itself exhibits non-linear behaviour, so has a refractive index dependent upon intensity. This self-focusing of the more intense modes, along with the natural cavity losses, causes behaviour which is similar to that of a saturable absorber in passive mode-locking, and thus self mode-locking takes place. However, self mode-locking will not start in a laser like this without an external influence, which can take the form of either rapidly changing the optical path length, or by jolting one of the mirrors to create an individual intensity pulse.

2.2 Photoconductive sources

It has already been mentioned earlier in this chapter, that all experiments undertaken in this thesis have used radiation generated by sources based on this technology. Therefore, it seems reasonable to give a complete description of both their history and the underlying Physics behind them. A photoconductive source consists of a changing dipole moment within a semiconductor, which then emits short bursts of radiation either along some sort of transmission line or into freespace. The dipole is created by accelerating the electron-hole pairs formed by the laser pulse using either an internal electric field built into the semiconductor via engineering, or an externally applied bias. The rise time of the photocurrent is then similar to the duration of the optical pulse, whilst the decay time depends on the time constant of the carrier lifetime.

2.2.1 History of photoconductors

In 1974, David Auston first reported the production of electrical signals, which had been generated optically, that lasted for the order of picoseconds[62]. Subsequent work a decade or so later, again by Auston *et al,* showed that photoconductors, driven by optical excitations, could be used to produce and detect picosecond pulses of radiation which could propagate through space[55]. Their approach was *"strongly influenced by the symmetry and simplicity of Hertz's original experiments with dipole radiation."* Further work, much of it undertaken by groups led by Grischkowsky in the latter part of the

1980's, showed that sub-picosecond pulses could also be generated by point sources, using a focused laser beam and further, that their profile could be characterised after propagation along both transmission lines and through freespace[63, 64].

The electric field of a dipole is, in general, a non-trivial expression. However, since photoconductive sources radiate energy away from themselves, the electric field of interest is always in what is known as the far field. Short optical pulses can be considered as in the far field regime after propagating a distance of approximately $\tau_p c/n$, where τ_p is the pulse duration[55]. This distance is of the order of a few hundred microns for a 1ps pulse, whilst detection with antennas takes place a few tens of centimetres from the source that is well into the far field. Thus, the electric field measured can actually be approximated as:

$$E_0 \propto \frac{1}{c^2 R}\sin\theta\frac{\partial^2 p}{\partial t^2}, \tag{2.8}$$

in spherical coordinates[65]. Here, R is the distance between the dipole and the point of observation and θ is the angle between the dipole moment, p and its propagation direction. Furthermore, it is also known that if the photocurrent is $i(t)$ in the transmitting gap of the dipole of length l, then:

$$\frac{\partial p}{\partial t} \propto l i(t). \tag{2.9}$$

In other words, the radiated electric field is proportional to the rate of change of current across the gap:

$$E_{THz} \propto \frac{\partial i(t)}{\partial t}. \tag{2.10}$$

2.2.2 Directional properties of terahertz radiation

First, we consider the case of a semiconductor under the influence of some form of electric field, which is being illuminated by an unfocused, collimated laser beam. Figure 2.3 is a schematic of the optical beams and radiated fields.

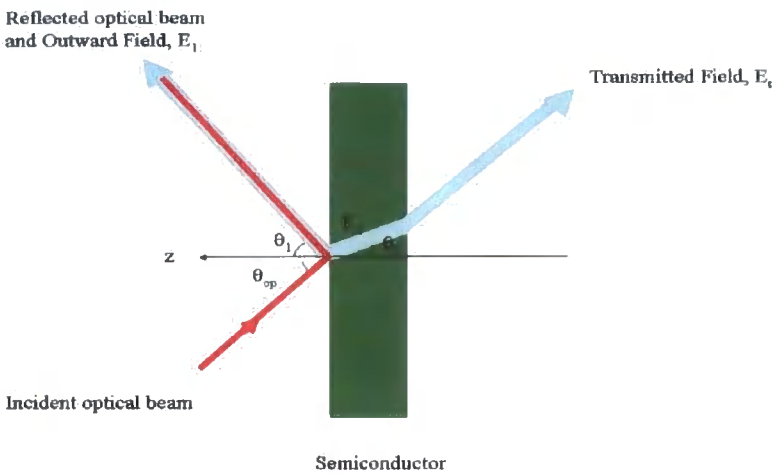

Figure 2.3: Directions of incident, reflected and transmitted beams.

Since the laser beam dimensions are large compared with the wavelengths of the emitted radiation, a generalised form of Snell's Law, obtained by in plane conservation of the wave vector, gives the following for the directions of the reflected and transmitted radiation[66]:

$$n_1(\omega_{op})\sin\theta_{op} \sim n_1(\omega_{el})\sin\theta_1 \sim n_2(\omega_{el})\sin\theta_2. \qquad (2.11)$$

Here $n_1(\omega_{op})$ and $n_1(\omega_{el})$ are the refractive indices of the optical beam and radiated field outside the sample and $n_2(\omega_{op})$ is the index of refraction of the radiated beam in the sample. Since the indices of refraction of the optical beam and the electric field are very similar in air, the reflected optical and terahertz beams are approximately collinear.

2.2.3 Surface fields of semiconductors

Near to the surface of a semiconductor, the Fermi level is "pinned" by surface states, causing the conduction and valence bands to bend near the interface. This leads to the formation of an area of charge depletion, of width l_d, see figure 2.4. This creates a built-in field, normal to the surface edge, which accelerates charge carriers generated by an

above band-gap pulse, with the electrons moving to the surface and the holes to the

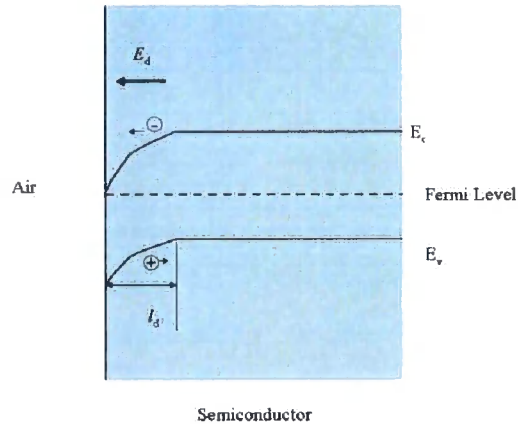

Figure 2.4: Semiconductor band diagram.

wafer[67]. A changing dipole is thus generated, creating a transient current in the surface and hence electric waves are radiated. Using a Hertz vector potential with a plane wave approximation shows that the amplitudes of the reflected and transmitted waves, as shown in figure 2.3 are:

$$E_1 = \eta_2 J_S \frac{\sin\theta_1}{\cos\theta_1 + (n_2/n_1)\cos\theta_2}, \tag{2.12}$$

$$E_t = -\left(n_1/n_2\right) t(\theta_2) E_1, \tag{2.13}$$

where η_2 is the characteristic impedance of the sample, $t(\theta_2)$ is the electric field transmission coefficient and $J_s = \frac{\mu e}{\hbar\omega} W_{op}[1 - R(\theta_{op})]\cos\theta_{op} \int_0^\infty E_d(x) e^{-\alpha x} dx$ is the angle dependent photocurrent across the layer. Here W_{op} is the optical intensity, $R(\theta_{op})$ is the optical reflectivity at the surface and $E_d(x)$ is the built-in field[66].

These equations imply that the radiated field is proportional to the incident optical density, as well as the built-in field and the carrier mobility. Providing that the incident optical density is not too large, the static field will be independent of time and the radiation field proportional to the number of photocarriers. Under higher excitation this relation breaks down. In both cases however, the upper limit of the surface radiated power can be calculated from the surface static energy $E_s \propto E^2 d$. This shows that a

surface with a static field acts as a capacitor, which discharges on excitation by a laser pulse. Theoretical simulations have been undertaken to find ways to improve the efficiency of the emission, and thereby improve the intensity of the terahertz radiation, by application of a magnetic field or using semiconductor prism structures[68].

2.2.4 Terahertz radiation from photoconductive antennas

In a photoconductive antenna, two electrodes are deposited onto a semiconducting substrate and an external electric field applied across the gap between them. Illumination of the gap by an above bandgap optical pulse creates electron and hole pairs, which drift at different rates in the applied field, due to their differing mobilities. This results in a transient current *i(t)* flowing between the two electrodes, which produces a dipole moment:

$$p(t) \propto \frac{\partial i(t)}{\partial t}. \tag{2.14}$$

This drives the emission of terahertz pulses perpendicular to the air-semiconductor surface. Figure 2.5 shows a schematic of terahertz generation and gives an example

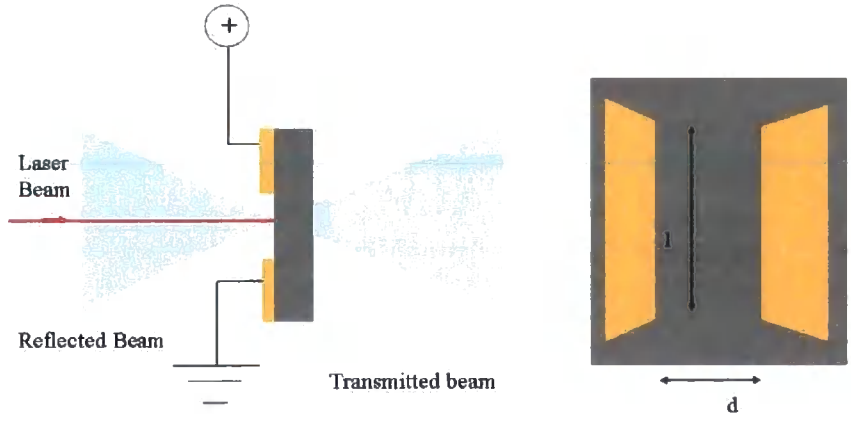

Figure 2.5: Generation of terahertz radiation from a biased photoconductive emitter.

geometry of a photoconductive switch. Typically, the gap, *d*, is a few hundred microns, whilst the electrode length *l* is a few millimetres long. The field emitted by the switch is proportional to the time derivative of the current, so has both positive and negative components. It is dominated by the rising edge of the current transient, which leads to a

fast first half cycle. The second, negative half cycle is much slower and depends on the current decay.

Such an emitter can also be thought of as a charged capacitor. When the switch is not illuminated it stores an amount of electrostatic energy, $E_s = (1/2)CV^2$, where C is the capacitance of the gap[69]. At these times it has a high resistance, of the order of mega ohms. When the gap is illuminated by a laser pulse, the stored energy is depleted in less than 150 fs by the separating carriers, and the resistance of the gap drops by several orders of magnitude. This depletion completely screens the external field.

The field at the surface of a photoconductive emitter, which is parallel to the plane of the photoconductor, can be calculated using the boundary conditions for the electric and magnetic components at the surface, which reduce to those of the steady state solution. Applying Stoke's theorem to Faraday's Law shows that the radiated electric fields at the photoconductor surface are equal, $E_{r,in}(t) = E_{r,out}(t)$,[70] in stark contrast to the case of a Hertzian dipole as given in equation (2.8). Consideration of the magnetic fields allows the surface current to be expressed as a function of the inward radiated electric field:

$$J_s(t) = -\frac{(1+\sqrt{\varepsilon})}{\eta_0} E_{r,in}(t), \tag{2.15}$$

where η_0, is the freespace resistance. This can also be expressed in terms of the bias field, E_b using Ohm's law:

$$J_s(t) = \sigma_s(t)(E_b + E_{r,in}(t)), \tag{2.16}$$

where $\sigma_s(t)$ is the surface conductivity, which is proportional to both the carrier mobility μ, and I_{opt} the optical pulse intensity:

$$\sigma_s(t) \propto \int_{-\infty}^{t} dt' \mu(t-t') I_{opt}(t') \exp\left(-{(t-t')}/{\tau_{car}}\right). \tag{2.17}$$

where τ_c is the lifetime of the excited carriers. Using equations (2.15) and (2.16) the inward radiated field is thus[70]:

$$E_{r,in}(t) = -E_b \frac{\sigma_s(t)\eta_0}{\sigma_s(t)\eta_0 + (1+\sqrt{\varepsilon})}. \tag{2.18}$$

As the time integrated optical intensity increases so does the surface conductivity and hence the inward and outward fields saturate at the maximum of the surface conductivity:

$$\sigma_{s,\max} = \frac{e(1-R)\mu_{tr}F_{opt}}{\hbar\omega}, \tag{2.19}$$

where μ_{tr} is the transient carrier mobility, R is the reflectivity and F_{opt} is the optical excitation fluence, assuming that the lifetime is much longer than the optical pulse width. The far field, which is detected, can be approximated as a function of the displacement along the centre of the radiated beam z:

$$E_{r,far\,\max}(z) \cong -\frac{1}{4\pi\varepsilon_0 c^2}\frac{J_{s,\max}}{\tau_p}\frac{A}{z}, \tag{2.20}$$

where A is the area of illumination[70]. Thus, higher frequency components are diffracted less and remain closer to the beam centre.

Equations (2.18) and (2.19) show that the emitted terahertz field depends upon both the bias applied to the emitter and the optical intensity incident upon it. The transient photoconductivity also varies inversely with the carrier lifetime, and thus by inference this has a bearing on the bandwidth of the emitted radiation. The efficiency of photoconductive antennas depends upon numerous factors including the carrier mobility[71] and the antenna design. Efficiency increases of more than an order of magnitude have been reported by the use of sharp-edged metal electrodes for example[72]. Even though the efficiency is proportional to the carrier mobility it does not depend strongly on the carrier lifetime. As such, it is usually better to use emitters fabricated on materials of high resistivity as opposed to high mobility, making low temperature annealed Gallium Arsenide (LT-GaAs) a very good material for the photoconductors[73]. Its properties (mobility, lifetime and resistivity) can be carefully controlled during the growth process by molecular beam epitaxy. Using high resistivity materials allows higher bias fields to be applied to the emitters, so that higher terahertz fields can be generated.

Much work has been undertaken in the development of photoconductive sources. Low temperature grown Gallium Arsenide has been found to provide the broadest emission spectrum, with bandwidths of over 30 THz being reported using a biased,

asymmetrically excited emitter[74]. To obtain such high bandwidths however, does require the radiation to be collected off the front surface, that contains the electrodes, to prevent absorptions within the substrate. Use of silicon hemispherical lenses, attached to the back surface of the emitter, has been used as a way to improve the brightness of the source[63]. However, this method does somewhat limit the useful bandwidth of the radiation, since the THz radiation must propagate through both the emitter substrate and the lens. Addition of a lens creates a THz beam with a Gaussian profile, emitted from an aperture having diameter equal to that of the lens[75].

2.3 Terahertz detectors

Two distinct types of technology can be used to detect terahertz radiation: incoherent detectors that measure the total energy of the incident radiation; and coherent detectors, that are used in the detection of terahertz pulses.

2.3.1 Incoherent detectors

This type of detector technology has existed for a very long time and works on the principle of measuring the heating effect of the incident radiation. It thus just measures the radiation intensity, or total energy, and provides no phase information. Common examples include the Bolometer, Golay Cell and Pyro-electric detectors. Bolometers are simply some sort of absorber connected to a heat sink, and any radiation absorbed raises the temperature relative to the heat sink. To detect terahertz frequencies they need cooling to cryogenic temperatures, but do provide the most accurate detectors for use in many astronomical applications. Golay Cells provided the standard way to measure infrared radiation for many years, before the advent of solid state devices. Radiation incident on the cell heats a plate in contact with a gas chamber. The gas in the chamber thus expands against a diaphragm, whose change in size can be measured by a strain gauge. Pyro-electric detectors utilize crystals that produce an electric potential when heated by radiation incident upon them.

2.3.2 Coherent detectors

To conveniently and efficiently detect the very low powers emitted by pulsed terahertz sources required the development of a new method of detection. Two main types of coherent detectors exist: electro-optic detectors and photoconductive antennas. The detection scheme used depends upon the terahertz measurements that are being

undertaken and both types of detection technology were used for the experiments undertaken in this thesis.

Electro-optic detection: The principle behind this technique is the Pockels effect, a second order, non-linear effect, whereby certain crystals exhibit non-linear behaviour when subjected to an electric field. This non-linearity then manifests itself as birefringence[76].

The crystal structure of a birefringent material means that it is anisotropic. This means that the speed of the wave passing through the material depends on the direction of propagation through the crystal. Any light ray incident on such a crystal is split into two rays that have mutually orthogonal polarisations, and in general travel at different speeds. Their speed is the same only along the direction corresponding to the optic axis of the crystal. If an incoming ray is incident perpendicular to both the crystal face and its optic axis, the two rays travel through the crystal in the same direction and at different speeds, so the wavelengths of the two rays are different within the crystal. Consequently, the rays emerge with a phase difference, which is dependent upon the crystal thickness and incident wavelength. This principle is used in the manufacture of both quarter- and half-wave plates, which create phase differences of $\pi/2$ and π respectively. A quarter wave plate is used to change the polarisation of light from plane polarised to circular polarised[77].

A typical electro-optic crystal used for terahertz detection is ZnTe. The plane polarised laser beam passes through the crystal unchanged in the absence of a terahertz field. This laser beam then passes through a quarter wave plate and becomes circularly polarised. A Wollaston prism is then used to separate the two orthogonally polarised components for detection using a differential pair of balanced photodiodes. Since the orthogonal components are equal in size, the balanced detector reads zero. When a terahertz pulse is incident on the ZnTe crystal, the crystal exhibits birefringence. Therefore, the polarisation of the laser pulse passing through it becomes elliptical. The quarter wave plate just serves to change the plane of polarisation of the laser beam, which remains elliptical on passing through it. Thus the two orthogonal polarisation components have different intensities when split, which manifests itself as a differential current across the photodiodes. Figure 2.6 shows this concept in action.

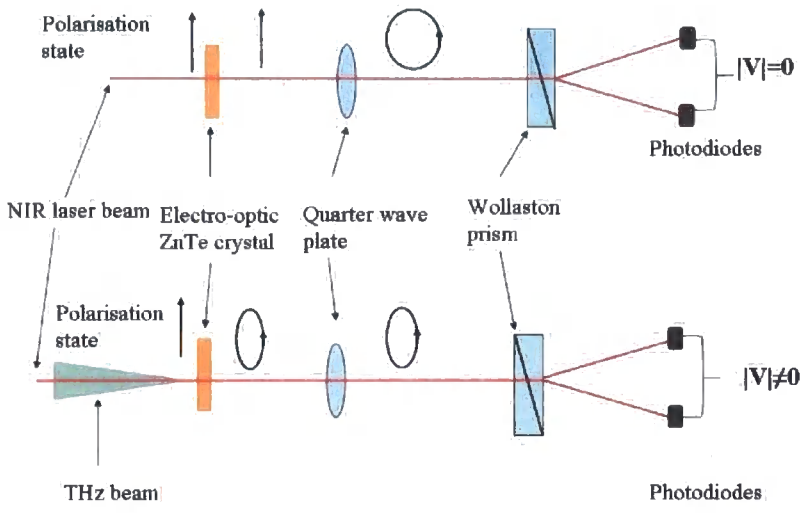

Figure 2.6: Overview of electro-optic detection.

Mathematically, this concept can be thought of in the following way. The polarisation of a crystal under the influence of a static electric field E_0 and time varying field, $E(t)$ can be described as follows:

$$P(t) = \chi^1 E(t) + \chi^2 E_0 E(t). \tag{2.21}$$

This relation implies that the variation in refractive index is proportional to the static field[78]. Since a terahertz pulse lasts for the order of a picosecond, whilst a laser pulse is only femtoseconds in duration, the terahertz field can be regarded as static. Thus the change in current across the photodiodes provides a measurement of the refractive index of the ZnTe crystal at any given point in time. This change in index is a direct measurement of the instantaneous birefringence of the crystal, and because the crystal works via the Pockels effect, this change is directly proportional to the electric field that the crystal is experiencing. As such, the current measured by the photodiodes is directly proportional to the instantaneous terahertz electric field. It should also be noted that since the laser pulse is much shorter than the terahertz pulse, the polarisation at any given time just corresponds to one point of the terahertz electric field. Correct selection of the crystal allows the measurement of large frequency bandwidths; thinner crystals allow the detection of higher bandwidths since the propagation dispersion of the terahertz beam is minimized[79].

Photoconductive antenna detection: This method proceeds in the inverse way to terahertz emission from photoconductors. Briefly, a bow-tie structure is fabricated on a semi-conductor substrate, usually low temperature grown Gallium Arsenide. When the terahertz electric field is incident on this structure a voltage difference is induced across the electrodes. Excitation of the switch, using a laser pulse, causes a current to flow that is proportional to the voltage. The photocurrent across the antenna can be related to the terahertz electric field amplitude[80], the number of photocarriers excited by the gating beam, $N(t)$ and the carrier mobility, μ :

$$J(\tau) = e\mu \int_{-\infty}^{\infty} E_{THz}(t)N(t-\tau)dt. \tag{2.22}$$

The frequency distribution of this antenna can then be found to be proportional to the temporal profile of the number of injected photocarriers. Measurement of the current therefore allows the instantaneous terahertz electric field to be determined:

$$I(t) \propto V(t) \propto E_{THz}(t). \tag{2.23}$$

By delaying the optical detection pulse with respect to the terahertz pulse, the full terahertz electric field can be recorded. A more thorough discussion of receiver design is given in chapter four.

Various studies have been undertaken to compare the terahertz waveforms measured using either electro-optic crystals or photoconductive sampling. The waveforms emitted by various emitters, measured by the two types of detection have been found to have differing shapes, but the photoconductive waveform shape can be derived from the electro-optic waveform if the carrier lifetime is taken into account[81]. Use of high modulation frequencies for the terahertz beam has shown that both types of detection have comparable signal to noise performance and sensitivity, over the frequency range 0.1-3 THz[82]. However, using thin electro-optic crystals gives on the whole a larger frequency bandwidth response in this frequency regime[80]. Kono *et al* first reported the detection of up to 20 THz emitted from electro-optic crystals using a photoconductive antenna[83]. In more recent times, ultrabroadband terahertz systems have been reported using photoconductors for both the emitter and receiver, fabricated on low-temperature Gallium Arsenide[84]. Selection of the correct emitter and detector technology plays a large part in designing terahertz experiments. But on the whole, use of a

photoconducting antenna as the emitter combined with an electro-optic detector gives the best performance[85] for a broadband system.

2.4 Terahertz time domain spectroscopy

Most terahertz research is currently undertaken using a technique known as terahertz time domain spectroscopy, which emerged about 20 years ago[86]. Here, an emitter and a detector are excited by the same above band-gap, pulsed laser beam. After generation of the terahertz wave, it is collected, usually using parabolic mirrors, before being transmitted through or reflected off the sample of interest. The transmitted, or reflected beam, is then collected by more optics before being focused onto the detector, concurrently with the probe beam.

In this technique, the two optical paths are set to be the same length. Since the path lengths are matched, only pulses created by the same part of the laser beam as that incident on the receiver, at any given instant, are detected. In other words, the detection pulse is synchronous with the terahertz pulse. This means that the very low power terahertz pulses, generated via semiconductor methods, can be detected with incredibly high signal to noise ratios, within the large thermal background of radiation which exists throughout all space at these frequencies. Chopping the terahertz beam mechanically, or by applying an alternating electric field to the emitter, allows lock-in detection to be used, which further increases the sensitivity of this technique. By delaying one laser beam with respect to the other, by use of a delay line, the electric field of the whole of the terahertz pulse can be mapped out. This is because the laser pulse lasts for only a few femtoseconds, whereas the terahertz pulse is approximately one picosecond in duration. Thus the laser beam allows the instantaneous terahertz electric field to be measured at a given point of the pulse.

For terahertz time domain spectroscopy to proceed, a reference scan is initially recorded. For transmission measurements, this is in the absence of a sample, whilst for reflection measurements it is the terahertz waveform that has been reflected off a plane mirror, which has replaced the sample. Another terahertz waveform is then recorded with the sample present. The electric field is now different due to absorption within the sample and Fresnel reflections at the surfaces. Using knowledge of how

electromagnetic waves interact with matter, described below, allows interpretation of these results

2.4.1 The interaction of electromagnetic waves with matter

To interpret the spectra obtained using a time domain setup requires an understanding of how electromagnetic waves interact with matter. Numerous processes exist in which radiation and matter can interact and we are concerned with the following: absorption, refraction and scattering. These are described in more detail below.

Absorption: Radiation is emitted by an atom or molecule when it undergoes a change of state to become energetically more stable: an electron in a high energy state, usually the first excited state, decays to a state of lower energy. To conserve energy and momentum the change of electron level, is accompanied by the emission of a photon of energy equal to the energy difference of the states: $\Delta E = E_{exc} - E_g$. The photon's frequency is thus $f = \Delta E/h$, using Planck's energy quantisation relation. Absorption is the inverse of this process, whereby a photon excites the molecule. Examination of the transmission spectrum of a material that has been illuminated by a continuous spectrum of radiation will reveal a number of dark lines. These correspond to the frequencies that have been absorbed by the material.

When a wave is (partially) absorbed by a medium that it is being transmitted through, it must also be attenuated. The sum of the transmitted energy and energy transferred to the medium by excitation is necessarily constant. The attenuation of a wave can be quantified by considering the power fraction of a wave that is absorbed per unit length:

$$\frac{dI}{dz} = -\alpha I(z), \tag{2.24}$$

where α is the absorption coefficient. Solution of this equation leads to the well known Beer-Lambert Law, $I(z) = I_0 e^{-\alpha z}$.

Reflection and refraction: When an electromagnetic wave hits the interface between different media, part is reflected and part is transmitted. The ratio of the amount transmitted and reflected is given by the Fresnel coefficients. These ratios depend on the refractive index of the media concerned (dielectric constant), the plane of

polarisation of the ingoing wave and the angle at which the radiation first hits the sample. If the incident beam hits the sample at non-normal incidence the transmitted wave is refracted, see figure 2.3, and its direction of propagation is changed. For an electromagnetic wave crossing an interface, the boundary conditions on the electric and magnetic fields require that their tangential components are continuous across the interface. If plane waves are considered, the incident field is given by $\bar{E}_I(r,t) = \bar{E}_{0I} \exp(i[\omega_I t - \bar{k}_I \cdot \bar{r}])$, with similar expressions for the reflected and transmitted waves, denoted by subscripts R and T respectively. Matching these fields at the interface shows that when $r = 0$, $\omega_I = \omega_R = \omega_T = \omega$ and when $t = 0$, $\bar{k}_I \cdot \bar{r} = \bar{k}_T \cdot \bar{r} = \bar{k}_R \cdot \bar{r}$. Resolving these vectors in the x direction (assuming that the wave is propagating along the z direction, with the interface plane being at z=0) results in $k_I \sin\theta_I = k_R \sin\theta_R = k_T \sin\theta_T$. Since the refractive index is $n_1 = ck/\omega$ by definition, consideration of the incident and reflected fields reveals that $\theta_I = \theta_R$, the law of reflection, since these waves are travelling in the same medium. Alternatively, considering the incident and transmitted field reveals:

$$\frac{n_1}{n_2} = \frac{\sin\theta_T}{\sin\theta_I}, \tag{2.25}$$

where n_1 is the refractive index of the first medium, and n_2 is the refractive index of the second medium, containing the transmitted wave. This is Snell's law, which states that the direction of propagation of an electromagnetic wave incident at the boundary of two media (having different dielectric constants) changes on entering the second medium.

The reflectance and transmittance are defined by the following relations:

$$R = \frac{E_{0R}^2}{E_{0I}^2}, \qquad T = \frac{n_2}{n_1}\frac{E_{0T}^2 \cos\theta_T}{E_{0I}^2 \cos\theta_I}, \tag{2.26}$$

which are related to the Fresnel coefficients:

$$r = \frac{E_{0R}}{E_{0I}}, \qquad t = \frac{E_{0T}}{E_{0I}}. \tag{2.27}$$

The Fresnel coefficients can be found by considering a plane wave incident at the interface between two media of differing dielectric properties under the following boundary conditions:

I. The component of the electric field parallel to the plane of incidence must be continuous.

II. The component of the magnetic field parallel to the plane of incidence must be continuous[87].

This means that the coefficients depend upon the polarisation of the field. If the wave is polarised parallel to the plane of incidence they are:

$$r_p = \frac{\cos\theta_I - \frac{n_1}{n_2}\cos\theta_T}{\cos\theta_I + \frac{n_1}{n_2}\cos\theta_T}, \qquad t_p = \frac{2\frac{n_1}{n_2}\cos\theta_I}{\cos\theta_I + \frac{n_1}{n_2}\cos\theta_T}. \quad (2.28)$$

but if the wave is polarised normal to the plane of incidence they become:

$$r_n = \frac{\frac{n_1}{n_2}\cos\theta_I - \cos\theta_T}{\frac{n_1}{n_2}\cos\theta_I + \cos\theta_T}, \qquad t_n = \frac{2\frac{n_1}{n_2}\cos\theta_I}{\frac{n_1}{n_2}\cos\theta_I + \cos\theta_T}. \quad (2.29)$$

Since the angles are always real, and the coefficients relate the ratios of transmitted and reflected fields to the incident field, it can be seen that the transmitted field and the incident field are always of the same sign. In other words they are in phase. However, the reflected field's phase depends upon the relative sizes of the incident and transmitted angles, which of course depend upon the relative refractive indices. If the second medium is optically more dense than the first (has a higher refractive index), then $\theta_T < \theta_I$, so the normal fields must always have opposite signs, which corresponds to undergoing a phase change of π. For perpendicular polarisation, once the sum of the incident and transmitted angles becomes greater than 90° the fields change sign. This can most easily be seen if the ratios are written as:

$$r_p = \frac{\tan(\theta_I - \theta_T)}{\tan(\theta_I + \theta_T)}, \qquad r_n = -\frac{\sin(\theta_I - \theta_T)}{\sin(\theta_I + \theta_T)}. \quad (2.30)$$

using Snell's Law, equation (2.25). Similar considerations hold if the first medium is the more optically dense[88].

If the wave is polarised parallel to the plane of incidence the reflectance and transmittance become, using equations (2.26) and (2.28):

$$R_p = \left[\frac{\cos\theta_I - \frac{n_1}{n_2}\cos\theta_T}{\cos\theta_I + \frac{n_1}{n_2}\cos\theta_T}\right]^2, \qquad T_p = \frac{4\frac{n_1}{n_2}\cos\theta_I\cos\theta_T}{(\cos\theta_I + \frac{n_1}{n_2}\cos\theta_T)^2}, \quad (2.31)$$

with similar expressions holding for the perpendicular polarisation. In both cases $R+T=1$. Further, if the wave is incident normally to the boundary, its polarisation state cannot be distinguished and the reflection and transmission coefficients reduce to:

$$R = \left(\frac{n_1 - n_2}{n_1 + n_2}\right)^2, \qquad T = \frac{4n_1n_2}{(n_1 + n_2)^2}. \quad (2.32)$$

Scattering: This process can either be elastic or inelastic. Elastic scattering occurs when: the photon energy is too low to cause excitation; or the photon is absorbed and immediately re-emitted at the same frequency. Classical descriptions of elastic scattering exist if: the wavelength of the incident radiation is much greater than the average particle size in the medium, otherwise known as Rayleigh scattering; or when the wavelength of the radiation is of the same order as the scattering particles, Mie scattering. In inelastic scattering, the photon energy is large enough to cause a transition within the atom and hence the emitted photon is of lower energy to the incident photon. This is known as Raman scattering.

2.4.2 Interpretation of terahertz waveforms

In a terahertz time domain experiment, two waveforms are required. The reference field, $\overline{E}_{ref}(t)$, transmitted through freespace and the sample field, $\overline{E}_{sam}(t)$, which has interacted with the sample. The sample field is in general: shifted in time, due to the refractive index difference between the medium and freespace; smaller in size due to absorptions within the sample and the Fresnel reflections of the wave at the sample's surface; and of a different shape due to dispersion caused by the non-uniform variation of the sample's absorption as a function of frequency.

The complex transmission of the sample, as a function of frequency, can be calculated in two ways: by taking the ratio of the Fourier Transformations of the reference and transmitted fields; and by appealing to the Fresnel coefficients. If the Fourier transformed fields are:

$$\overline{E}_{ref}(\omega) = \varepsilon_{ref}(\omega)e^{i\varphi_{ref}(\omega)}, \qquad \overline{E}_{sam}(\omega) = \varepsilon_{sam}(\omega)e^{i\varphi_{sam}(\omega)}, \tag{2.33}$$

the complex transmission is given by;

$$T(\omega) = \frac{\overline{E}_{sam}(\omega)}{\overline{E}_{ref}(\omega)}. \tag{2.34}$$

This can also be defined via:

$$T(\omega) = t_{12}t_{21}\exp\left[i\frac{\omega d}{c}\{\tilde{n}(\omega)-1\}\right]FP(\omega), \tag{2.35}$$

where t_{12} and t_{21} are the Fresnel coefficients for transmission at each face, $\tilde{n}(\omega) = n + i\kappa$ being the complex refractive index, and $FP(\omega)$ is the Fabry-Perot term,

which describes multiple reflections within the sample. For thick samples, this term can be neglected, as the presence of multiple internal reflections in the time domain data can be avoided. The Fresnel transmission coefficients in the case of normal incidence, are $t_{12} = 2/(n+1)$ and $t_{21} = 2n/(1+n)$, where n is the refractive index of the second medium, and the first medium is assumed to be free space, having refractive index of unity. These are the same for both polarisations. Equations (2.33) and (2.34) allow the real part of the refractive index to be found:

$$n(\omega) = 1 + \frac{c}{\omega d}(\varphi_{sam} - \varphi_{ref}), \tag{2.36}$$

whilst the extinction coefficient is given by:

$$\kappa(\omega) = -\frac{c}{2\omega d}\ln\left(\frac{1}{t_{12}t_{21}}\frac{\varepsilon_{sam}}{\varepsilon_{ref}}\right). \tag{2.37}$$

This can be related to the absorption coefficient, $\alpha = 4\pi\kappa/\lambda$, so that the absorption coefficient of the material is:[89]

$$\alpha = -\frac{2}{d}\ln\left(\frac{(n+1)^2}{4n}\frac{\varepsilon_{sam}}{\varepsilon_{ref}}\right). \tag{2.38}$$

2.5 The Durham transmission terahertz spectrometer

Transmission experiments reported in this thesis were carried out using a standard terahertz time domain spectrometer pumped by an ultra-fast Ti:sapphire laser (Coherent Inc.). The laser had the following characteristics: bandwidth 45 nm, which corresponds to pulse lengths of 20 fs assuming Gaussian profiles; average pulse power of 450 mW; a 76 MHz repetition rate; and it was centred at a wavelength of 790 nm. Pulses from the laser were initially negatively chirped by passing them many times off special multilayer mirrors. This negative chirping compensates for the positive chirp introduced by all the other optics used to steer the laser beam into the terahertz setup. Thus, when the laser beam reaches the terahertz emitter and receiver, it has a much smaller positive chirp than would be the case without the presence of the compensating mirrors and consequently, it is less dispersed and has spread out less in time. To help prevent the laser beam waist from growing as it propagates along the optical bench it is passed through a telescope system immediately after exiting the compensation mirrors. Figure 2.7 is a schematic of the lasers and associated optics.

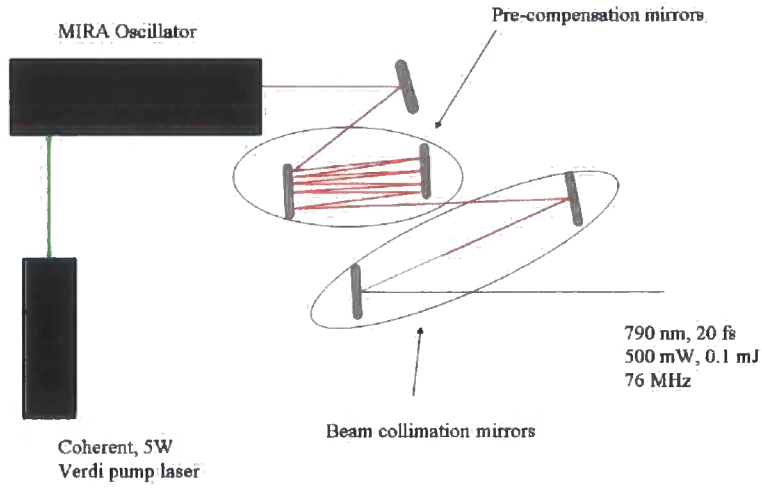

Figure 2.7: Schematic of lasers and compensation mirrors.

Using a beam splitter, 70% of the laser power was then transmitted along what becomes known as the pump path and incident on the THz emitter, whilst the other 30% was reflected at right angles to the pump path, to form the probe beam. Before reaching the emitter, the near infrared beam passed along a mechanical optical delay line, which allowed the lengths of the terahertz path and the detection path to be changed with respect to one another and therefore the whole temporal electric field of the terahertz pulse to be measured.

The laser beam was focused, using a lens of focal length 12.5 cm, on to the edge of one of the electrodes, which were biased at 270 V DC to generate THz radiation. After collection and focusing of the THz radiation using parabolic mirrors, coherent detection was performed using electro-optic sampling techniques. All parabolic mirrors used were of diameter 5 cm. The collection mirror had focal length 5 cm, the two intermediate mirrors had 10 cm focal lengths and a mirror of focal length 7.5 cm focused the radiation on to the detector. The probe laser beam was incident concurrently with the THz pulses on to a 1 mm thick Zn-Te crystal (Ingcrys Ltd). Lock-in detection, using a 1 kHz mechanical chopper placed in the pump arm, was used to measure the electric field of the THz pulse. Figure 2.8 shows a schematic of the experimental set-up,

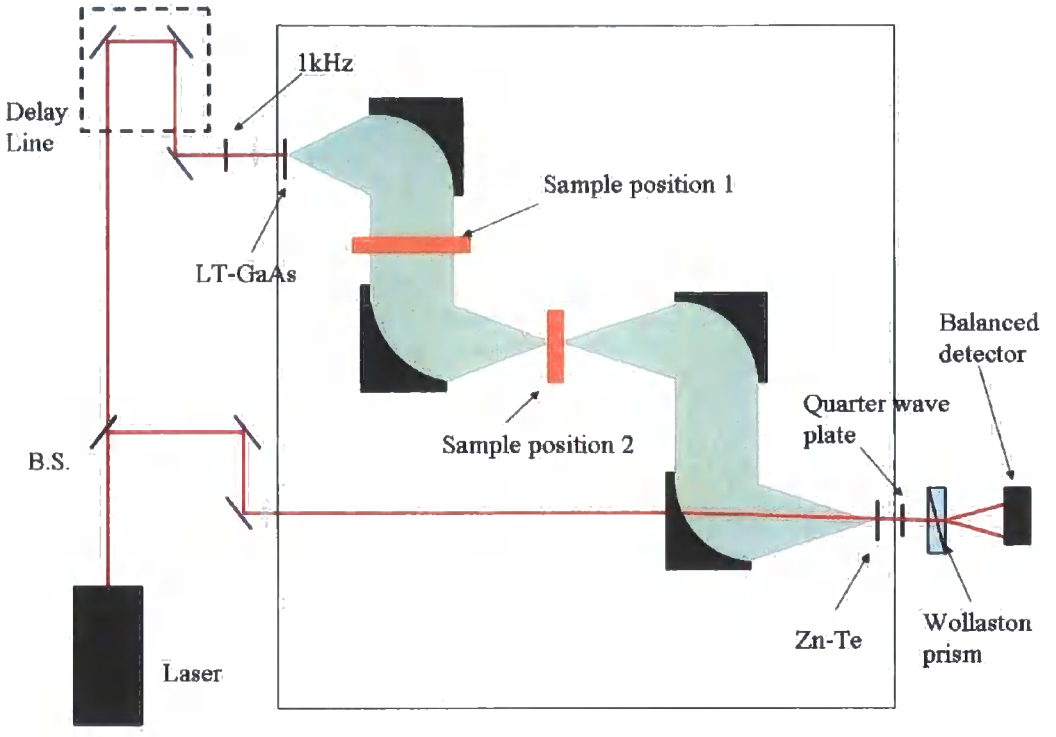

Figure 2.8: Schematic of terahertz time domain system.

which is also pictured in figure 2.9. It should be noted that the transmission measurements were carried out using both focused (sample position 2) and

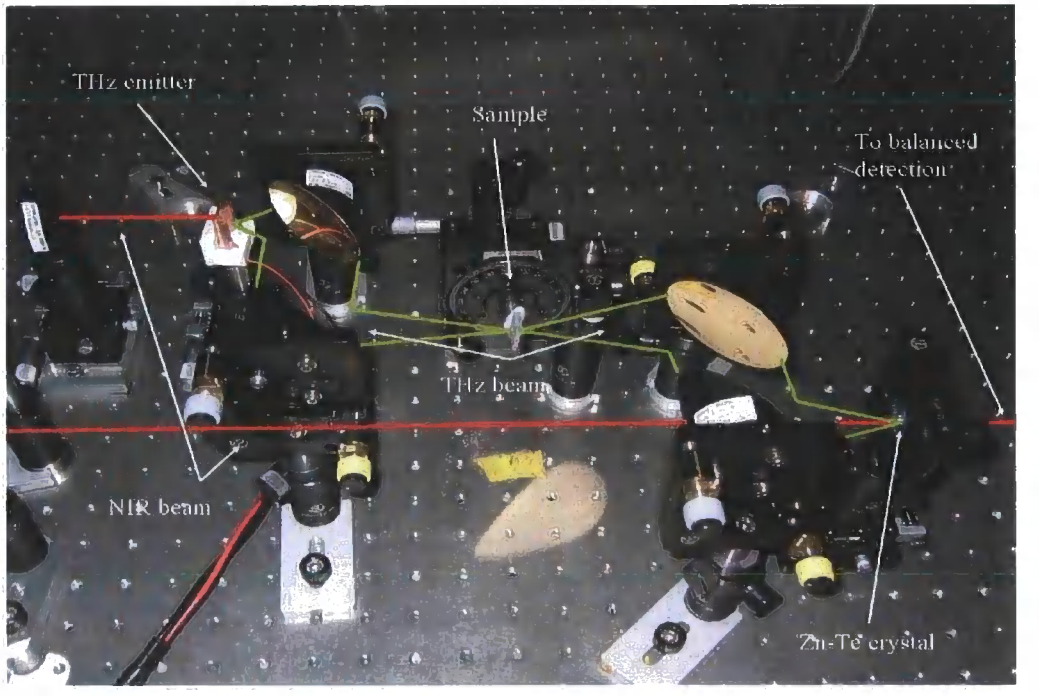

Figure 2.9: Picture of the "business" end of a Terahertz Time Domain Spectrometer.

unfocused beams (sample position 1). Pulses of usable bandwidth 3.5 THz, with peak power at 0.9 THz and signal-to-noise ratio of 4000:1, were routinely obtained with this arrangement. The whole system was enclosed in a dry nitrogen atmosphere to negate the effect of water absorption on the terahertz pulse. Water is a polar molecule so readily absorbs THz.

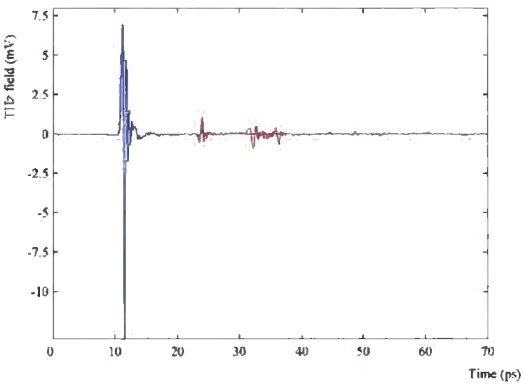

Figure 2.10: Typical terahertz waveform: raw data (red), after the application of Gaussian smoothing (blue).

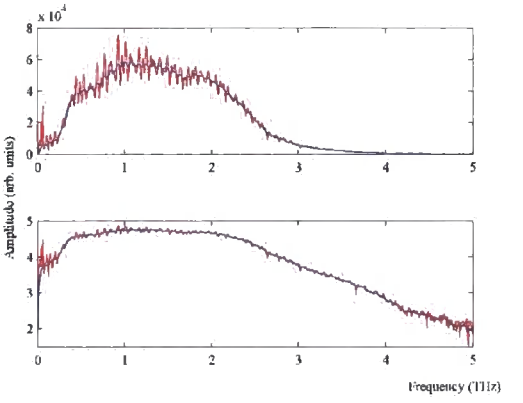

Figure 2.11: Spectra of terahertz pulse: raw data (red), after the application of Gaussian smoothing (blue).

Figures of a typical THz pulse and its associated spectra obtained from this system, with nitrogen purging, are shown above. The red waveform in figure 2.10 is that recorded, the small peak, delayed by approximately 12 ps is due to a reflection of the generated terahertz pulse in the emitter substrate. The blue waveform is the same terahertz pulse after the application of Gaussian smoothing, with a smoothing constant of 10 ps. The associated frequency spectra are shown in figure 2.11, with the lower spectrum plotted on a logarithmic scale. As can be seen, this system produces terahertz pulses, with useable bandwidth extending out to over 3 THz.

The THz spectrum of water vapour, calculated from a pulse which has propagated through an unpurged atmosphere, is shown in the upper part of figure 2.12 and a number of water absorption lines can be seen at the characteristic absorption frequencies[90]. For example, 1.7 THz, 2.7 THz and 3.0 THz. These are more clearly shown in the transmission spectrum in the lower part of the figure, which is found by taking the ratio of the Fourier Transform of the THz pulses recorded in both unpurged and purged atmospheres.

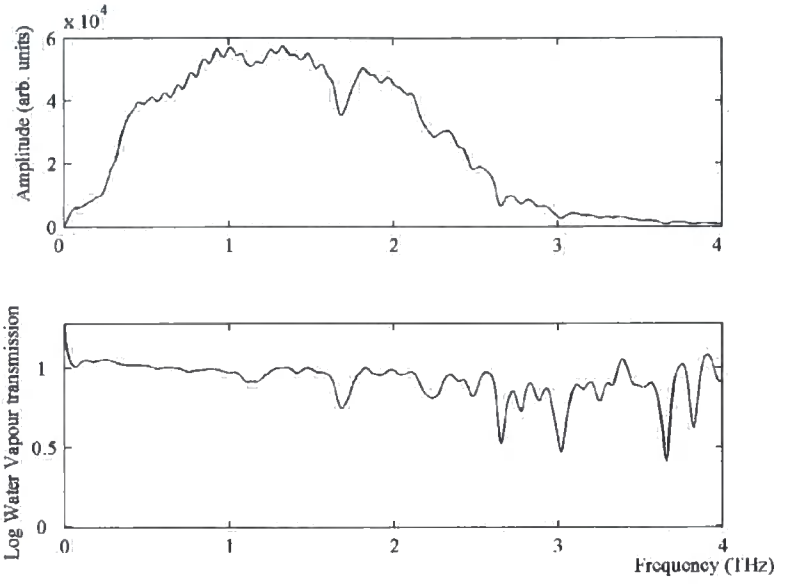

Figure 2.12: Terahertz pulse spectra without nitrogen purging.

2.5.1 Characteristics of a terahertz source used at Durham

A typical terahertz emitter used for the work in this thesis consisted of two chrome-gold electrodes fabricated on low temperature annealed Gallium Arsenide, separated by $d = 400\ \mu m$ and having length $l = 4$ or 8 mm. The behaviour of one such terahertz emitter is outlined below. Good knowledge of the emitter's behaviour allows it to be run safely over an extended period of time without electrical breakdown occurring.

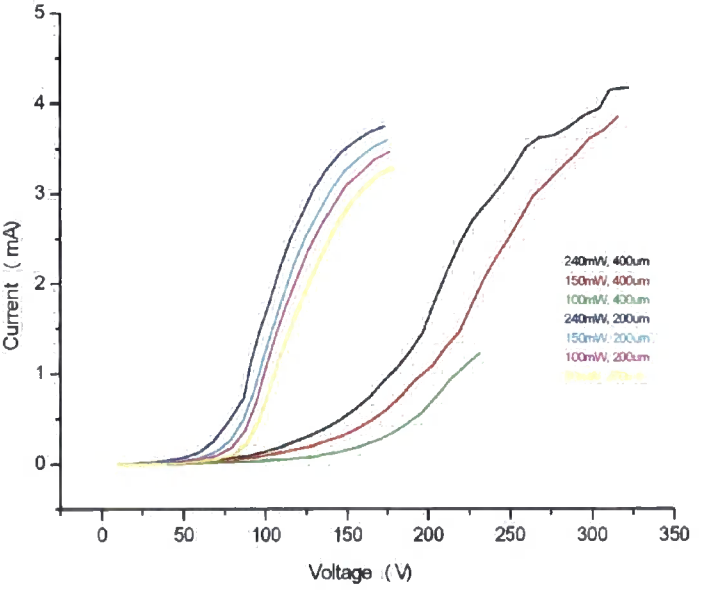

Figure 2.13: I-V curves for 200 µm and 400 µm gap emitters.

In figure 2.13, the I-V curve of two terahertz emitters, fabricated on LT-GaAs are shown, one having photoconductive gap of 200 μm and the other a gap of 400 μm. The current through the switch increases linearly with applied bias voltage in both cases, with both sets of curves levelling out when a bias field of approximately 750 kVm^{-1} is reached. This was determined to be the maximum safe operating bias field for the emitters.

Measurements were also made to investigate how the peak terahertz electric field varied with bias, and this is shown in figure 2.14 for the 400 μm gap emitter used above for both an increasing and decreasing voltage. These measurements were carried out using a photoconductive antenna as the receiver.

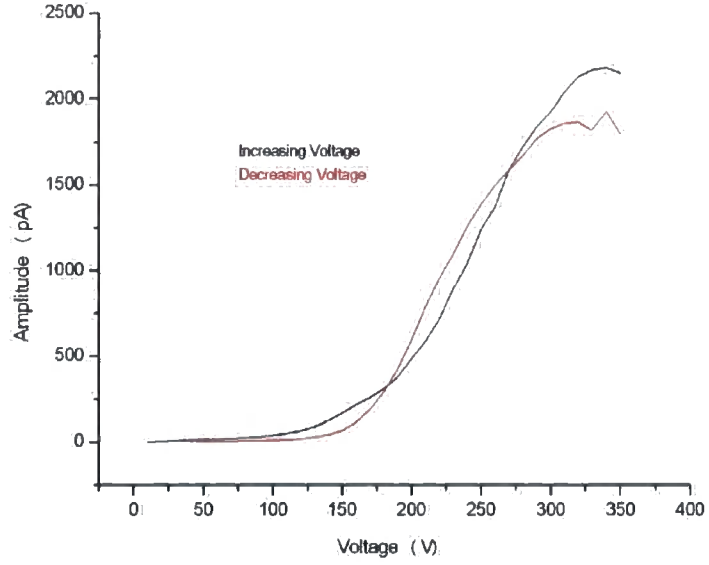

Figure 2.14: Peak terahertz amplitude with voltage for 400 μm emitter.

Finally, as it is known that the terahertz field can be increased by asymmetric excitation of the gap by the laser pulse, measurements were made to investigate how the peak electric field changed as the laser spot was scanned across the photoconductive gap.

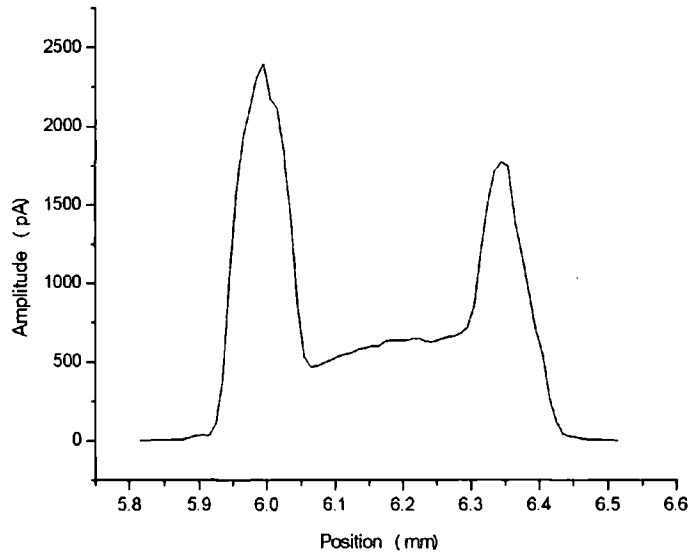

Figure 2.15: Peak terahertz field, with excitation spot position.

Figure 2.15 shows the variation of peak field with position for a 400 μm emitter, biased at 220 V and measured using a photoconductive antenna. Here the maximum emission amplitude takes place when the laser pulse is focused onto the anode of the emitter.

2.6 Summary

This chapter has introduced modern methods for the efficient generation and detection of terahertz radiation. In particular, it has concentrated on the "two-stage" approach to generation, whereby one form of radiation, short pulses of coherent laser light, are converted to terahertz radiation by their interaction with semiconductor structures. After introducing the various sources, it was shown how the excitation of suitable semiconductor structures, with suitable short pulses of near infrared light can lead to the generation of pulses of radiation.

Having understood how terahertz generation and detection proceeds, a discussion was given on how to combine an emitter and a detector, driven by a laser pulse, into a suitable system to undertake terahertz time domain spectroscopy. Various considerations must be taken into account when designing the emitter and detector, but it has been found that large aperture emitters, fabricated on low-temperature grown GaAs, provide the best emitters for the bandwidth most commonly sought after, 0.2 – 3.5 THz. For detection, the most stable performance is seen using electro-optical

methods, and in our case a 1mm thick ZnTe crystal. However, use of a thinner detection crystal along with backward collection of the terahertz radiation would allow broader bandwidths to be obtained.

Finally, a description of the transmission terahertz time domain spectrometer, built at Durham was given. The performance of this system was discussed and example measurements of the characterisation of a terahertz source given.

3. Transmission of terahertz radiation through non-homogeneous materials

This chapter is concerned with understanding how terahertz radiation propagates through materials that are inherently random in nature. It is the first step to understanding how THz radiation is scattered by targets of interest. Terahertz frequency sensing and imaging systems have many potential applications in a wide range of areas such as: medicine and biology, security and surveillance and process control. Although significant efforts have been expended on the development of imaging systems[9, 10], somewhat less attention has been paid to the issue of propagation through, or scattering from, realistic target materials which might be investigated with such systems.

Understanding the interaction of THz radiation with a wide range of irregularly structured materials is an essential part of the design of systems for THz sensing and imaging. Scattering can be used to advantage in imaging but can also cause spurious effects in the detected signal. On one hand, it might be used to advantage to determine the characteristic size, texture and location of an object concealed within a matrix of other material[91]. On the other hand, it may produce false signatures in spectra when interference takes place within a scattering structure (e.g. fibres in clothing or granules of powder), or diminish and alter the return signal from a suspect item secreted below garments. Scattering effects are particularly relevant in the THz region. Here, the wavelength, and the size and separation of scattering centres, are often commensurable.

The work in this chapter begins with a brief discussion of the scattering and propagation of electromagnetic waves through a dielectric medium. Since THz pulses contain a wide spectrum of frequencies, wavelengths which are both much less and greater than the average particle size propagate through the medium[92]. Thus both Rayleigh scattering and the Mie solution are applicable, and these phenomena are outlined. After this, a review is given of some of the other work which has been undertaken in the general area of THz scattering. Exact solution of Maxwell's equations for wave propagation through an array of scatterers is prohibitively difficult. It would therefore be highly desirable to have some kind of empirical approximation methods to predict this behaviour. One such method, "The Phase Distribution Model,"

(PDM), is then presented[93]. The predictions of this model can be tested by: comparison with exact theory; comparison with numerical solutions of the Maxwell equations; and experimental methods. Sections 3.4 and 3.5 of this chapter describe these tests. Finally, a discussion is given on the feasibility of the construction of a stand-off terahertz detection system for the detection of for example hidden contraband, using these results.

Some of the results presented in this chapter have been published in: J.R. Fletcher, G.P. Swift, J.A. Levitt D. Dai, and J.M. Chamberlain *Propagation of terahertz radiation through random structures: An alternative theoretical approach and experimental validation* J App Phys **101** 013102 (2007). I am grateful to Dr. John Fletcher for the initial development of the Phase Distribution Model, which has been used to make predictions of the propagation of terahertz radiation through various experimental phantoms.

3.1 Scattering of electromagnetic waves

Much work has been done in other frequency regimes to describe the scattering of electromagnetic waves by random media. In particular, the propagation of radio waves through the atmosphere has been extensively studied both for radar and communication applications. A thorough review of wave propagation and scattering by random media is given in Ishimaru[94].

Scattering of EM waves is one of the two basic phenomena that occur when a wave illuminates a particle, the other being absorption. Plane waves provide the simplest way to describe them. For the general case of a wave being scattered by some particle having typical dimension D, (e.g. diameter) two broad regimes exist for the description of the amplitude and phase of the electromagnetic field with distance, R from the scatterer. When $R < D^2 / \lambda$ these field quantities are complex, but for $R > D^2 / \lambda$ the field can be described by a spherical wave. The incident and scattered fields are used to describe the scattering behaviour, which is most conveniently expressed in terms of cross-sections[95].

For a single particle, its scattering cross-section is defined to be the total observed scattered power at all angles:

$$\sigma_s = \int_{4\pi} \sigma_d d\omega = \frac{\sigma_t}{4\pi} \int_{4\pi} p(0,i) d\omega. \tag{3.1}$$

Here σ_d is the differential cross-section, $p(0,i)$ is the phase function and $d\omega$ is the differential solid angle. This phase function just represents the amount of scattered power. The absorption cross-section can be defined for dielectric scatterers as the volume integral of the losses inside the particle:

$$\sigma_a = \left(\int_V \frac{1}{2} \omega \varepsilon_0 \varepsilon_r'' |E|^2 dV \right) \Big/ S_i . \tag{3.2}$$

Here ε_r'' is the coefficient of the complex part of the dielectric constant and S_i is the flux density of the incident wave. The sum of the two above cross-sections gives the total cross-section:

$$\sigma_t = \sigma_s + \sigma_a . \tag{3.3}$$

This total cross section represents the total power loss from the incident wave due to scattering and absorption and is closely related to the behaviour of the scattered wave in the forward direction.

Simple expressions for some of these cross-sections can be derived for single particles if their size is much greater (or less) than the incident wavelength[95].

- If: Particle size >> λ then it can be shown that the total cross-section approaches twice the geometric cross-section, whilst the absorption cross-section approaches some constant value which is less than the geometric cross section.
- If: Particle size << λ then the scattered cross-section is proportional to the volume squared and inversely proportional to the fourth power of the wavelength. The absorption cross-section is inversely proportional to the wavelength and proportional to the volume. This is more commonly known as the Rayleigh regime.

It has already been indicated in the introduction to this chapter that two scattering phenomena are particularly important when discussing the scattering of broadband THz pulses. They are Rayleigh scattering and Mie Theory. These will be considered in turn.

Rayleigh scattering: This phenomenon describes the scattering characteristics of a small particle. The best known example is the blue sky. Shorter, blue wavelengths are scattered more by air molecules, water and ice in the atmosphere than the longer red

wavelengths. Expressions can be found for the scattering and absorption cross-sections for small dielectric objects, having simple geometries[95]. For example, for a dielectric sphere, having radius a, the scattering cross-section is:

$$\frac{\sigma_s}{\pi a^2} = \frac{8(ka)^2}{3}\left|\frac{\varepsilon_r - 1}{\varepsilon_r + 2}\right|^2, \tag{3.4}$$

whilst the absorption cross-section is:

$$\frac{\sigma_a}{\pi a^2} = \frac{4}{3}ka\varepsilon_r''\left|\frac{3}{\varepsilon_r + 2}\right|^2. \tag{3.5}$$

These equations are valid providing that $a < 0.05\lambda$. The two cross-sections are in fact expressed as a fraction of the geometric cross-section, πa^2.

Mie scattering: This solution of the wave equation was found in 1908 and is the exact solution for the scattering of a plane electromagnetic wave for an isotropic, homogeneous sphere. Therefore it should be referred to as the Mie solution of the Maxwell equations, as opposed to Mie theory. Here, the total cross section is:

$$\frac{\sigma_t}{\pi a^2} = \frac{2}{\alpha^2}\sum_{n=1}^{\infty}(2n+1)\{\mathrm{Re}(a_n + b_n)\}, \tag{3.6}$$

whilst the scattering cross-section is:

$$\frac{\sigma_s}{\pi a^2} = \frac{2}{\alpha^2}\sum_{n=1}^{\infty}(2n+1)(|a_n|^2 + |b_n|^2), \tag{3.7}$$

where $\alpha = ka$. The coefficients a_n and b_n are expressed in terms of Bessel and Hankel functions:

$$a_n = \frac{\psi_n(\alpha)\psi_n'(\beta) - m\psi_n(\beta)\psi_n'(\alpha)}{\zeta_n(\alpha)\psi_n'(\beta) - m\psi_n(\beta)\zeta_n'(\alpha)}, \tag{3.8a}$$

$$b_n = \frac{m\psi_n(\alpha)\psi_n'(\beta) - \psi_n(\beta)\psi_n'(\alpha)}{m\zeta_n(\alpha)\psi_n'(\beta) - \psi_n(\beta)\zeta_n'(\alpha)}, \tag{3.8b}$$

where $\beta = mka$, $\psi_n(x) = \sqrt{\pi x/2}\,J_{n+\frac{1}{2}}(x)$ and $\zeta_n(x) = \sqrt{\pi x/2}\,H^{(1)}_{n+\frac{1}{2}}(x)$.

This solution is valid over all wavelength to particle size ratios. The expression "Mie theory" now refers to solutions of Maxwell's equations for scattering by stratified spheres or by infinite cylinders also[95].

3.1.1 Multiple scattering

In a medium containing many scattering centres, multiple scattering events will take place. Two extremes exist. They are wave scattering from 'tenuous' and 'dense' collections of particles[96]. In a tenuous medium, the incident wave reaches the detector after interaction with only a few particles and the scattered wave is due to only a single scattering event. As the particle density increases, the directly propagating wave can no longer be assumed to be identical to the incident wave. Instead it has been attenuated by both scattering and absorption. Note that the scattered wave in this regime is only scattered once by the particle, but the wave incident on the particle has previously been attenuated by scattering and absorption. This is known as first order multiple scattering. On the other hand, when a wave interacts with a dense distribution of scatterers, diffusion approximations can be applied. Between these two extremes, the particle density is such that multiple scattering events take place and it is this which is often most interesting.

3.2 History of terahertz scattering experiments

Much work has been done to investigate the propagation through and the scattering of THz radiation from random arrays. Pearce and Mittleman[92] began by investigating the ballistic transmission of THz radiation through arrays of Teflon spheres having diameter 0.794 mm. In this work the scattering mean free path (MFP) was compared with results from Mie theory: the spectral range of the pulse components allows the MFP to be observed and compared over two orders of magnitude. These results were further compared with a quasi-crystalline approximation[97]. This approximates the solution of the multiple scattering equations over all possible scatterer configurations, and includes two-particle correlations. It is very obvious from this work that there is considerable disagreement between the experiments and the two differing theoretical approaches. The same authors also used similar experiments to undertake scale modelling of scattering[98]. At THz wavelengths, it is easy to study scattering from objects of millimetre dimensions before they are scaled because of the invariance of Maxwell's equations to length. Similarly, Cheville and Grischkowsky have used scale model experiments at THz frequencies to simulate radar[99].

Pearce and Mittleman extended their work to look at the diffusion of single cycle pulses through the same samples[100]. Using correlation functions allowed individual scattering events to be characterised in these measurements[101], with more recent developments centring around the further developments of statistical approaches to characterise multiply scattered terahertz pulses[102, 103].

Chau and Elezzabi on the other hand have been concerned with investigating THz propagation through assemblies of sub-wavelength alumina spheres. They conclude that terahertz pulses can propagate through such arrays for distances far greater than the skin depth[104]. Further work by Mujumdar *et al* found that the effective medium approximation, a first order truncation of the multiple scattering equation solution (as opposed to the second order quasi-crystalline approximation) underestimates the acquired pulse phase on propagation through these assemblies[105].

3. 3 The phase distribution model

A model has been developed to describe the propagation of radiation through media which have relatively small changes in refractive index. In this case, the medium can be regarded as a number of phase changing layers, and reflections within it can be neglected. Similar methods have been outlined in the literature to describe the transmission of radio waves through the ionosphere[106, 107]. The model uses a phase distribution function to summarise the optical properties of the layers of the randomly structured medium. These layers, of thickness d, must satisfy the following two conditions:

1. The thickness needs to be great enough so that there is no average correlation between the scatterer positions in adjacent slices. Any waves that are multiply scattered in successive layers will not contribute coherently to the forward propagation. The thickness should therefore not be less than the correlation length for the scatterer density.
2. On the other hand, the layer should be thin enough so that simple approximations can be used to calculate the phase distribution.

Use of this phase distribution, $P(\varphi)$ allows the fractional transmitted amplitude of the unscattered wave to be written as:

$$F = \int P(\varphi) e^{i\varphi} d\varphi. \tag{3.9}$$

If the mean free path of the directly propagating beam is L, the transmitted intensity through a layer, of thickness d, is:

$$|F|^2 = \exp(-d/L). \tag{3.10}$$

This can also be found from the phase distribution function using equation (3.9).

Since distribution functions are being used, statistical methods can be employed and the problem is reduced to finding suitable approximations for their calculation. The simplest method uses the projection approximation, in which the phase change, φ, in a single layer is given by:

$$\varphi(\rho) = 2\pi(n-1)t(\rho)/\lambda, \tag{3.11}$$

where $(n-1)$ is the refractive index difference between the scatterers and their surroundings and $t(\rho)$ is the thickness of the layer. The phase change in any layer can vary between zero, when no scatterers are present, and some maximum value $\varphi_{max} = 2\pi d(n-1)/\lambda$, when the layer is completely filled. An example of the projection approximation and the relevant phase distribution is shown in figure 3.1.

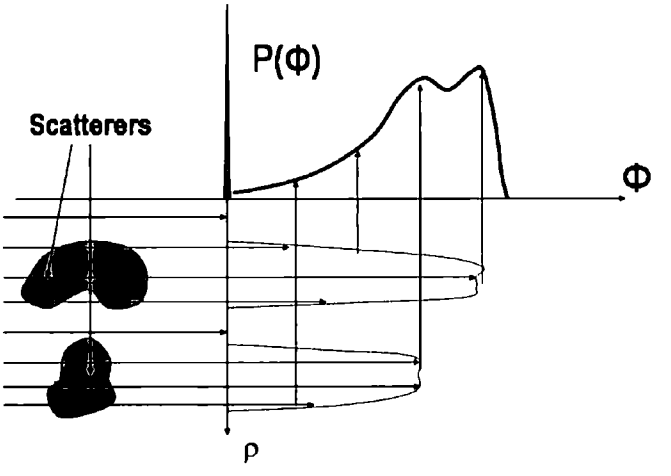

Figure 3.1: Projection approximation for phase distribution, *P*.

3.3.1 Example phase distributions

It is possible to analytically calculate the phase distribution for simple shapes such as spheres and cones by direct integration. If the scatterer has circular symmetry, φ is dependent on the radial coordinate r, within the geometric cross-section, πa^2 and the phase distribution for the scatterer is:

$$P_S(\varphi) = -\frac{d(r^2/a^2)}{d\varphi}, \qquad 0 \le \varphi \le \varphi_{\max}. \tag{3.12}$$

Sphere: $$\varphi_{sp}(r) = \varphi_{\max}\sqrt{1-(r/a)^2}, \qquad P_{sp} = 2\varphi/\varphi_{\max}^2. \tag{3.13}$$

Paraboloid: $$\varphi_{par}(r) = \varphi_{\max}[1-(r/a)^2], \qquad P_{par} = 1/\varphi_{\max}. \tag{3.14}$$

Cone: $$\varphi_{cone}(r) = \varphi_{\max}[1-(r/a)], \qquad P_{cone} = \frac{2}{\varphi_{\max}}\left(1-\frac{\varphi}{\varphi_{\max}}\right). \tag{3.15}$$

For more general, complicated shapes, the projected optical thickness can be evaluated numerically.

3.3.2 Absorbing scatterers

If the scatterers are absorbing, they have a complex refractive index $(n+i\kappa)$ and the projection approximation must allow for attenuation in the scatterer. The amplitude is reduced to:

$$a(\bar{\rho}) = \exp\left[\frac{-\kappa\varphi(\rho)}{n-1}\right], \tag{3.16}$$

and the transmitted amplitude is thus:

$$F = \int P_S(\varphi)\exp\left[\varphi\left(i-\frac{\kappa}{n-1}\right)\right]d\varphi, \tag{3.17}$$

where P_S is the distribution for the same shape of scatterers without dielectric loss.

3.3.3 Application of phase model to attenuating samples

The above formulae can be used to predict the attenuation of waves by various samples and comparison between the theory and experiments is given in section 3.5. However, certain considerations must be taken into account regarding attenuation from fabrics and powder; these are now outlined.

Fabrics: A woven fabric consists of orthogonal warp and weft yarns, so the phase changes produced are dependent upon orthogonal coordinates. Therefore, the total transmission is simply the product of that through the warp and weft separately, which

reduces the problem from a three-dimensional model to two separate two-dimensional calculations. Each yarn can be modelled as a cylinder with some effective refractive index. The predicted transmission is strongly dependent on the ratio between the yarn diameter and yarn gap. There is a phase difference between waves transmitted through the yarns and those transmitted through the gaps, which is proportional to frequency. As the gap size increases, these waves destructively interfere, and this can be seen in figure 3.2, where the parameter G represent the ratio of yarn gap to yarn diameter. Here, the effect of increasing the gap width can be seen on the transmission as a function of the maximum phase change induced on passing through a yarn.

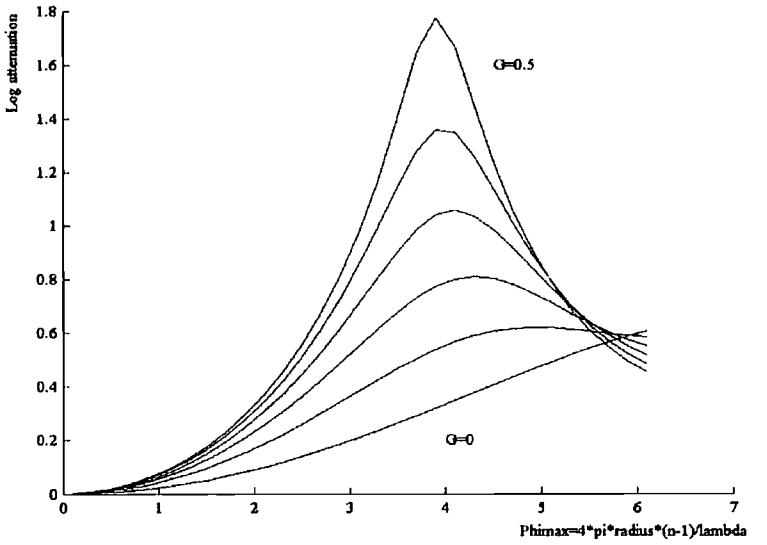

Figure 3.2: Effect of yarn gap on attenuation.

Powders: No simple phase distribution can be written down for a powder consisting of a collection of randomly shaped grains. By taking the slice thickness to be the same as the largest grains the maximum phase change can be found. The moments of the distribution are then proportional to this i.e. $M_r \propto \varphi^r$, and can be found by a frequency expansion of the layer transmission, equation (3.10). Using this, the following formula can be found for the mean free path:

$$L \sim \frac{\lambda^2}{dc(1-c)(\pi(n-1))^2}, \tag{3.18}$$

where c is the volume fraction and d is the average particle size.

3.4 Comparison of model with other results and theories

The validity of the phase model can be tested by comparing its predictions with those from other models, namely Mie theory and the numerical solution of the Maxwell equations.

3.4.1 Comparison of phase model with Mie theory

As outlined in section 3.1, the Mie solution is an exact solution of Maxwell's equations for scattering from a sphere. The scattering cross-section predicted by this solution has been compared with the cross-section from the phase model.

If an object with geometrical cross-section, S, and total scattering cross-section, Q, intercepts a wavefront of area, W, the fraction of the incident power remaining in the unscattered beam, I, is given by:

$$I = 1 - \frac{Q}{W}. \tag{3.19}$$

This is identical to $|F|^2$. The phase distribution for such an object is:

$$P(\varphi) = [(W - S)\delta(\varphi) + SP_S(\varphi)]/W, \tag{3.20}$$

with P_S as above. Thus, using equation (3.11) it is found:

$$I = 1 - \frac{Q}{W} = 1 - \frac{2S}{W}\left[1 - \int P_S(\varphi)\cos\varphi d\varphi\right] + O\left(\frac{S^2}{W^2}\right). \tag{3.21}$$

To measure the scattering meaningfully the area of the scatterer must be much less than the area of the wavefront, and the scattering cross-section is thus:

$$Q = 2S\left[1 - \int P_S(\varphi)\cos\varphi d\varphi\right] \tag{3.22}$$

Substitution of the projection approximation for the phase distribution of simple shapes means that the model can be compared with Mie theory exactly. For example, using equation (3.13) for an isolated sphere, of radius a, the cross-section is:

$$Q = 2\pi a^2\left[1 - \frac{2\sin\varphi_M}{\varphi_M} + \frac{2(1-\cos\varphi_M)}{\varphi_M^2}\right]. \tag{3.23}$$

Figure 3.3 shows this cross-section compared to the Mie theory result for a sphere having refractive index 1.33. Both the positions and magnitudes of the peaks are well produced for refractive indices below 1.5. However, at long wavelengths the cross-section is an order of magnitude (or more) too small. This is because the PDM only

predicts a cross-section proportional to frequency squared. It can be corrected by assuming an effective refractive index as described in the published paper on these results[93]. A similar result is shown for dielectric cylinders in figure 3.4. This result indicates that the approximation gives good agreement for refractive indices below about 1.5 and it becomes exact as it approaches unity.

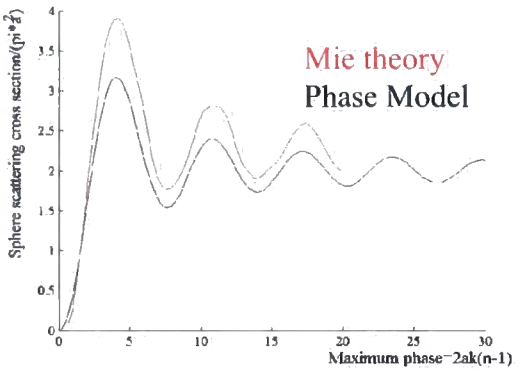

Figure 3.3: Total scattering from a dielectric sphere.

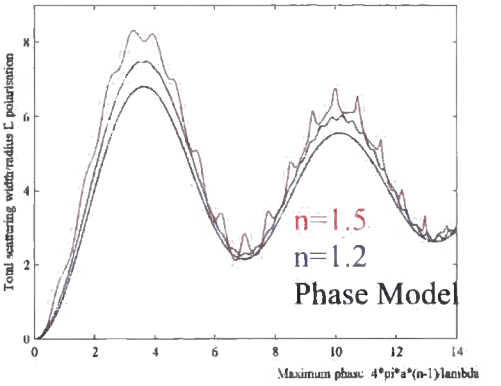

Figure 3.4: Total scattering from a dielectric cylinder.

3.4.2 Comparison with numerical simulations

Numerical solution of Maxwell's equations can be used to check models of wave propagation. In general, this method is time consuming, so is of limited use in a realistic situation, but it provides an excellent way of validating models. These calculations were performed on two dimensional random arrays of dielectric cylinders, using a combination of transfer matrix and multiple scattering techniques, implemented in the publicly available *Pendry Code*[108]. A finite-element method was used to solve numerically the equations on a defined mesh of points. Boundary conditions are set on the external plane of points in the mesh, and a transfer matrix can be defined that propagates the electromagnetic field onto the next plane of points. Such a procedure is iterated until the opposite external plane of points is reached. The transmission and reflection properties of the structure are then derived from the total transfer matrix.

Good agreement was seen between the model and the exact calculations at long wavelengths, but at short wavelengths the two results diverged somewhat. This is because the Phase Distribution Model calculates the transmitted field amplitude averaged over random scatterer positions: thus, the scattered amplitude averages to zero; but the forward wave amplitude does not. Conversely, the exact calculations determine the amplitude for a particular arrangement of random scatterers, which

contains contributions from both a broad background of multiple-scattered waves and a superimposed peak from the unscattered waves.

3.5 Experimental validation of the theory

Terahertz transmission was investigated through random structures with both known and unknown properties to validate the above model. All of the experiments reported here were carried out using the standard spectrometer, described in section 2.5. It should be noted that transmission measurements were carried out using both a focused beam, sample position 2 (SP2) and a parallel beam, sample position 1 (SP1) as shown in the schematic in figure 2.8.

3.5.1 Experimental objects tested

Various phantoms and everyday objects had their THz transmission properties measured. They included: arrays of cylinders; collections of powders; and clothing fabrics. The properties of each of these are now described in turn.

Arrays of cylinders: It is well known that many fabrics which go to make up e.g. clothing are made by weaving threads together. These threads themselves are constructed from much smaller fibres, but the threads can be approximated by cylinders. Arrays of cylinders can thus be used to mimic the structure of fabrics, with the advantage that, even though the arrangement of the cylinders within the array is random, their actual positions are known.

Construction of the arrays was undertaken by Ogel Models Ltd., who used a stereolithographic technique to build each array layer by layer by curing the resin Si-50 using ultraviolet light. This resin has a THz refractive index of 1.65±0.05, shown in figure 3.5 which was obtained from transmission measurements through a cured, planar piece of the resin, having thickness 0.33 mm. The erroneous, rapidly decreasing value of the refractive index, below approximately 300 GHz, is due to a lack of source power. The cylinder arrangement for each structure was determined using a random number generator to place a given number of cylinders within the area of the phantom.

Six arrays of cylinders were designed and constructed, each having a volume fraction of between 10 and 50 percent of the sample filled with identical cylinders. The diameter of the cylinders varied from phantom to phantom in the range 0.4 to 1.0 mm. Figure 3.6 shows a plan view of one such phantom, along with side and top profile

photographs. The array contains cylinders of diameter 0.3 mm, occupying a volume fraction of 28% of the sample.

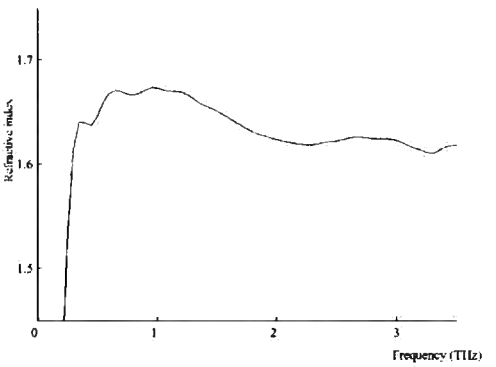

Figure 3.5: THz refractive index of Si-50.

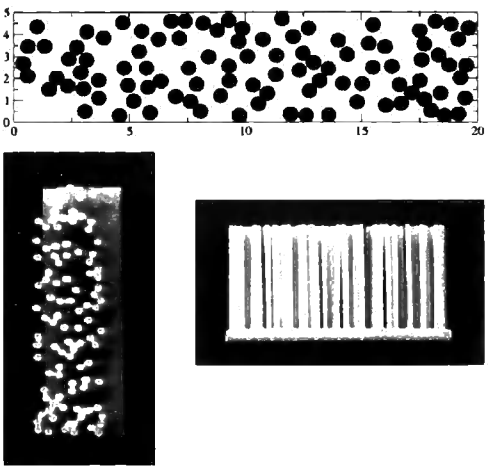

Figure 3.6: Plan view and photographs of phantom with cylinder diameter 0.3 mm and volume fraction 28%.

The table below summarises the properties of each of the cylindrical arrays:

Phantom	Dimensions (mm × mm)	Cylinder Diameter (mm)	Volume Fraction
1	5 × 20	0.4	0.1
2	1 × 20	0.4	0.5
3	5 × 20	0.3	0.28
4	3 × 20	1.0	0.4
5	5 × 20	0.5	0.2

Fabrics: Having investigated the transmission of terahertz radiation through random structures of known properties, measurements were then undertaken to investigate the propagation of THz in realistic materials. These included the following clothing fabrics: cotton shirt, fleece jacket and tweed jacket. Their structures could be determined by use of scanning electron microscopy.

Cotton shirts are the fabrics having the simplest structure: they consist of two sets of perpendicular yarns, the warp and the weft. Figure 3.7 is a magnified photograph of the tested fabric. The warp and weft parameters, which are required to undertake the modelling, can be directly measured from the SEM image of the fabric shown in figure 3.8, with a much magnified version of it in figure 3.9. In this particular shirt the warp and weft yarns are both of diameter 180 μm, whilst their spacings are 250 μm and 330

μm respectively. The SEM image reveals that the individual yarns are made up from bundles of fibres. However, these are too small to be resolved at THz frequencies.

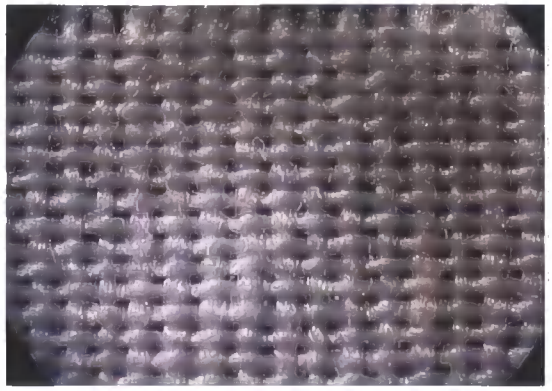

Figure 3.7: Magnified photograph of shirt fabric.

Figure 3.8: SEM image of shirt fabric.

The maximum phase changes for such yarns are relatively small, so a simple analytical expression for the phase distribution can be derived by evaluating the low order moments. For the case of parallel yarns of diameter d, and repeat distance w:

$$I = 1 - \varphi_M^2 \left[\frac{2y}{3} - \left(\frac{\pi y}{4} \right)^2 \right] + O(\varphi_M^4), \tag{3.24}$$

where $y=d/w$. The transmission is then the product of the warp and weft factors.

Figure 3.9: Magnified SEM of one (shirt) yarn.

Figure 3.10: SEM image of tweed.

Similarly to shirt fabrics, tweed is based on a warp-weft structure, but the yarn size is much greater, approximately 1.10 mm, with a spacing of 1.20 mm for both warp and weft. An SEM image of this is presented in figure 3.10. It should also be noted that the fibres in the yarns are much thicker than in the case of the shirt (approximately 0.06 mm). Therefore, it is no longer possible to treat the yarns as uniform cylinders in the modelling. Instead, the simplest model treats the tweed as a collection of wool fibres occupying an assumed volume fraction of 0.5.

The piece of fleece fabric (figure 3.11) had no long range fibre structure on the THz scale, which can be seen on examination of the SEM image in figure 3.12. Here, it can be observed that the fleece is constructed from a random array of fine fibres having no long range structure. The tufts on the surface of the fabric provide the main contribution to the optical thickness. The following expression summarises the phase distribution:

$$P = \frac{1}{\varphi_S}\left[1 + f\left(\frac{2\varphi}{\varphi_S - 1}\right)\right], \tag{3.25}$$

where f is the shape factor. This can vary between +1 and -1, corresponding to shapes from semi-ellipsoids to cones. For the modelling below, the tuft height was assumed to be 3.5 mm and the shape factor was 0.3

Figure 3.11: Optical image of fleece.

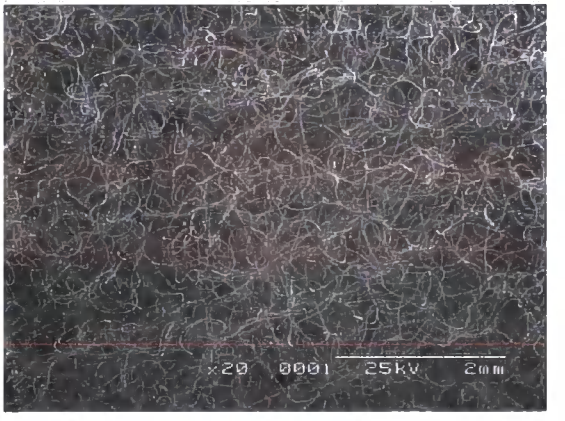

Figure 3.12: SEM image of fleece.

To complete the modelling, an estimate of the refractive index of the various fibres at THz frequencies is also required. The only work in the literature by Bjarnason *et al* investigated the merits of using THz technology over millimetre wave and mid-infrared for the stand-off imaging of common clothing samples[109]. They found that on average, clothing has an attenuation of 10 dB at 1 THz, and its average refractive index is 1.5. In the work presented here, a simple estimate was obtained for these indices from the observed delay of a THz pulse on passing through the materials, providing that their thickness is known, which is possible using a micrometer. Using this method, the refractive indices were found to be 1.28, 1.15 and 1.05 for the shirt, tweed and fleece respectively. This estimate is valid providing the fabrics are non-dispersive in the THz region.

Random powders: Street samples of both drugs of abuse and explosives are usually not pure. Instead, they are mixtures of compounds containing both impurities and cutting agents. Consequently, samples of these drugs will contain powders and particulates of various sizes, which will both scatter and (or) absorb THz radiation. An investigation of THz transmission through both highly-absorbing and non-absorbing powders was undertaken in an initial attempt to model the propagation of THz radiation in such situations.

Small diameter glass balls provide an ideal phantom for the investigation of THz transmission through highly absorbing powders. Two sizes of sphere were investigated, having mean diameters 227 μm and 462 μm. Polytetrafluoroethylene (PTFE) powder was used as the non-absorbing powder. The mean diameters of the grains were 100 μm, 55 μm, 12 μm and 1 μm. For both sets of measurements, a quantity of the powder was placed in a piece of milled out PTFE, having internal width 2 or 3 mm and wall thickness approximately 0.5 mm. PTFE was used for both the non-absorbing powders and to construct the sample holder since it is non-absorbing over the frequency range of a standard THz spectrometer.

3.5.2 Comparison of the phase distribution model and experiment: arrays of cylinders

Generalising the predictions of the propagation of a wave around a single cylinder, or through a layer of parallel yarns in a fabric, it is expected that when a wave passes through an arrangement of cylinders some frequencies will be attenuated, whilst others will be transmitted without too much loss. This is due to destructive interference between waves propagating through the cylinders and the gaps. The PDM can be used to make predictions of the frequency dependent attenuation of an array of cylinders having given diameter and occupying a certain volume fraction. It is only these two input parameters (vis the diameter and volume fraction occupied by the scatterers) which are required for the model. These factors determine the number of regions of high and low transmission and the frequencies at which they occur. Figure 3.13 shows transmission through a phantom containing 10% scatterers of diameter 0.4 mm, whilst figure 3.14 shows transmission for a phantom containing 40% scattering material of diameter 1.0 mm. The frequencies of high and low transmission, as predicted by the model, provide a reasonable description of the experimental data. Transmission was investigated for both a focused and unfocused THz beam, with the unfocused

measurements having the THz electric field both perpendicular (**H** polarisation) and parallel (**E** polarisation) to the cylinders. Using both a focused and an unfocused beam resulted in similar transmission spectra. However, for the least dense phantom, differences in the experimental transmission amplitudes are seen between the various spectra. This can be attributed to: there being more THz power over a small area of the phantom when the focused beam is used; and the dielectric cylinders causing more scattering of the wave in **E** polarisation. Polarisation effects are discussed in detail in chapter six.

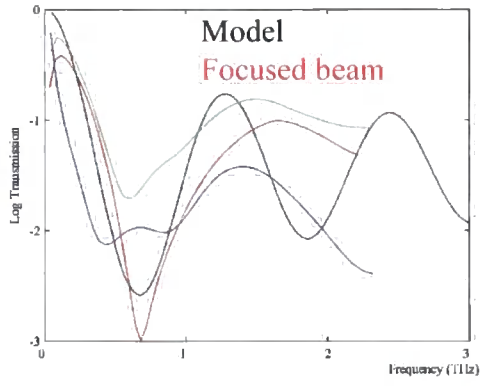

Figure 3.13: THz transmission through array of cylinders with 10% volume fraction and diameter 0.4 mm.

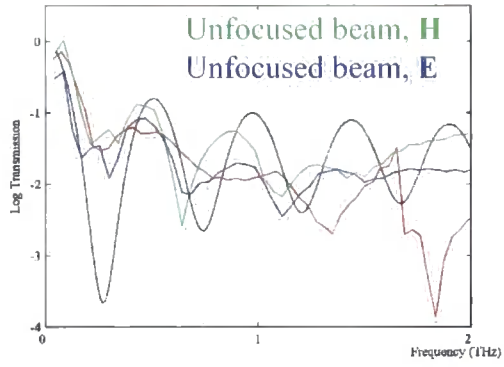

Figure 3.14: THz transmission through array of cylinders with 40% volume fraction and diameter 1.0mm.

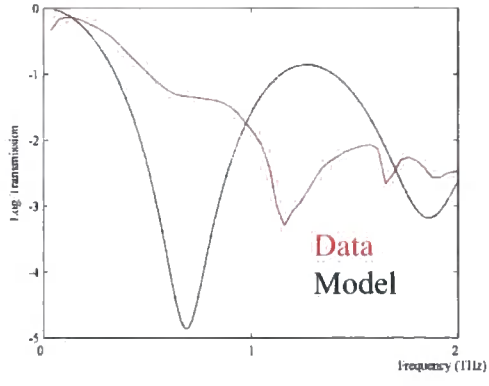

Figure 3.15: THz transmission through array of cylinders with 50% volume fraction and diameter 0.4 mm.

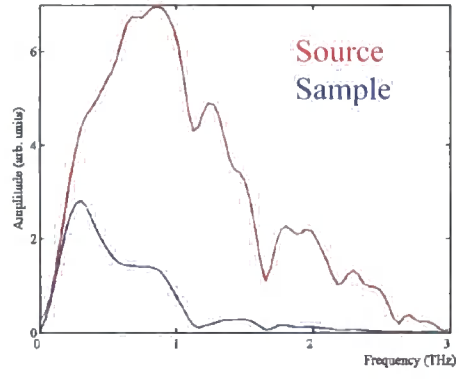

Figure 3.16: Source and sample spectra for transmission through cylinder arrays of 50% volume fraction and cylinder diameter 0.4 mm.

Figure 3.15 shows the THz transmission through the most concentrated array of cylinders. Here, the results begin to show the expected trend over the first 750 GHz or so, before diverging. Examination of the source and sample spectra (figure 3.16) reveals that there is no real transmission above 1 THz, so any transmission calculation above this frequency is unreliable.

3.5.3 Comparison of the phase distribution model and experiment: textiles

Figure 3.17 shows the attenuation of the THz beam on passing through the fabrics described above with the results of modelling with the phase distribution in black. Note, the dotted line of the tweed is when modelling took place using the simple analytic

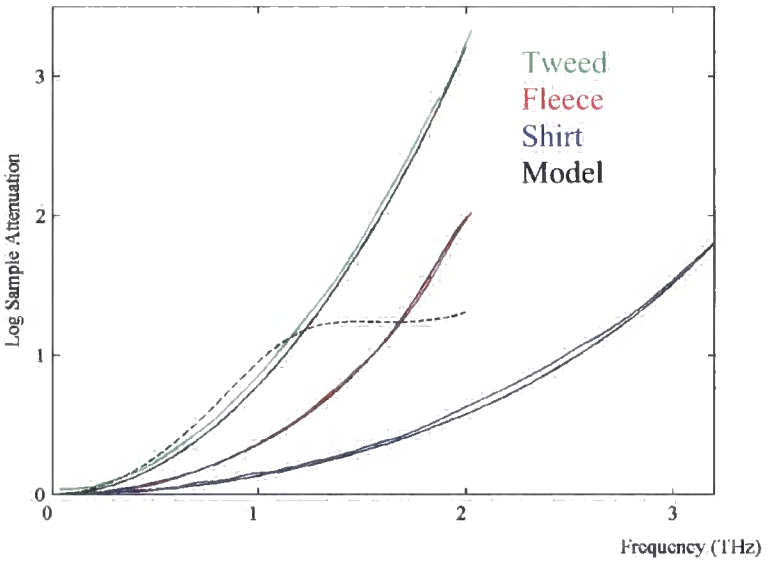

Figure 3.17: THz transmission through common clothing with modelling.

expression, based on the low order moments. This breaks down above 1 THz. In the absence of definitive information at THz frequencies, the effective indices have been empirically adjusted to give the best fit. For example the shirt empirical index is 1.25, the fleece index is 1.042 whilst the tweed index is 1.55 assuming a collection of random fibres, and 1.25 when the simple analytic expression is used.

3.5.4 Comparison of the phase distribution model and experiment: random powders

Terahertz transmission through the PTFE powders can be seen in figure 3.18, with the phase model's predictions for the two larger diameter powders. It should be immediately noted from the figure that the 12 μm diameter powder was more attenuating than the 55 μm powder and a similar result (not shown here) was seen for the 1 μm powder. Using the pulse delay formula allowed the effective refractive index and volume fractions to be calculated. For example the 100 μm powder had a volume fraction of 0.43, whilst the 55 μm powder's volume fraction was approximately one

third of that, and the 12 μm and 1 μm powders had volume fractions of 0.20. This indicates that these small diameter powders are clumping together and are not evenly dispersed.

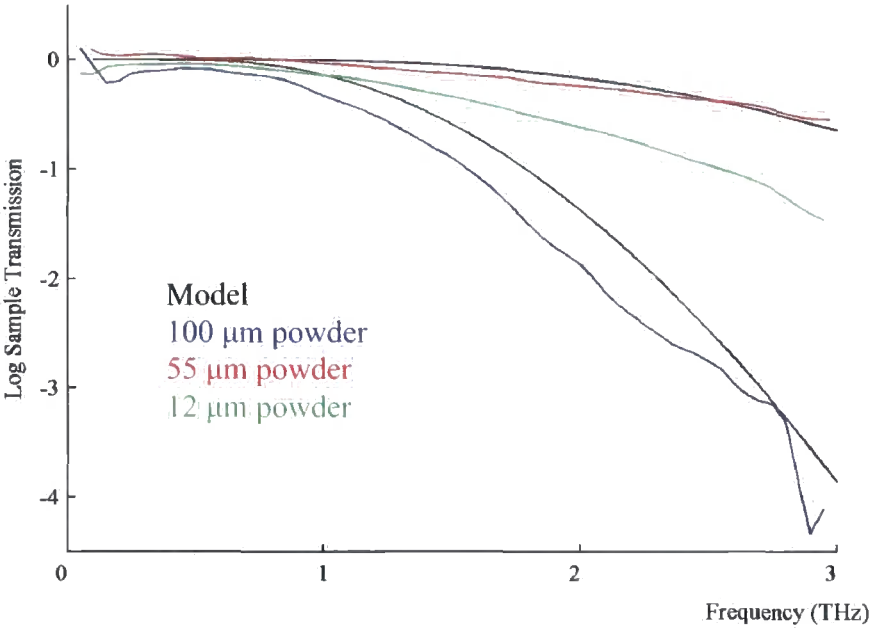

Figure 3.18: THz transmission through dielectric powders.

In the case of the absorbing glass balls, no THz frequency components above approximately 0.6 THz are transmitted as can be seen in figure 3.19, for example, which shows the transmission through both 2 and 3 mm thick cells containing balls of average diameter 227 μm. A similar result was seen for larger diameter balls. At a frequency of 0.6 THz the simple mean free path formula indicates that the mean free path through the balls is of the order of a few millimetres for both diameters, which is larger than the cell dimensions. As the frequency increases, the MFP falls, and therefore higher frequency components are more likely to be multiply scattered. Since the cut-off frequency is the same for both diameters of balls and both sample cell thicknesses it can be concluded that absorption and dielectric loss dominate over multiple scattering.

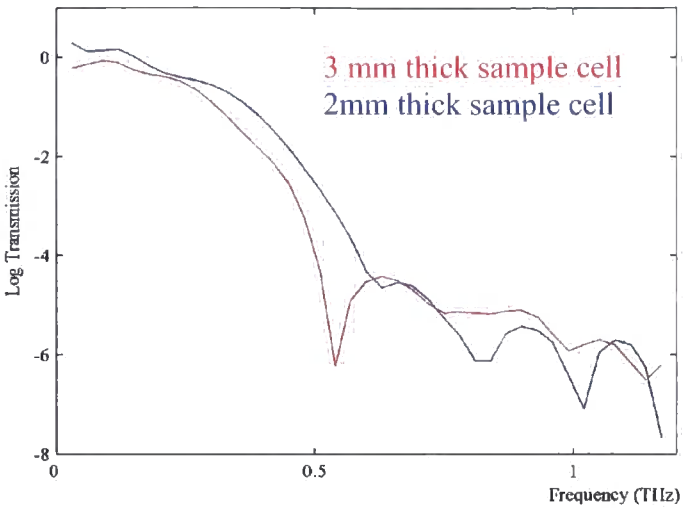

Figure 3.19: THz transmission through absorbing spheres.

3.6 Possibility of using terahertz radiation in a standoff detector system

Using the attenuation properties of fabrics obtained above, it is possible to make an estimate on the ability of a terahertz spectrometer to detect powders, for example drugs of abuse or explosives, concealed behind layers of clothing. A generic stand-off detection system is shown in figure 3.20. The source at A emits some form of terahertz beam, which then propagates through the air and a garment. At C, the THz beam passes into the target where it is scattered, before re-emerging at point D. After a second pass through the garment the THz beam propagates through the air to the detector at F.

To undertake this analysis a THz system is considered with a quantum cascade laser as its source, and detection is via a bolometer. A system based on such technology affords the highest, (relatively portable) THz powers with good detection capability. However, because QCL's only operate over a narrow frequency range, use of such a system would not provide the spectral identification advantages of a broadband pulsed system.

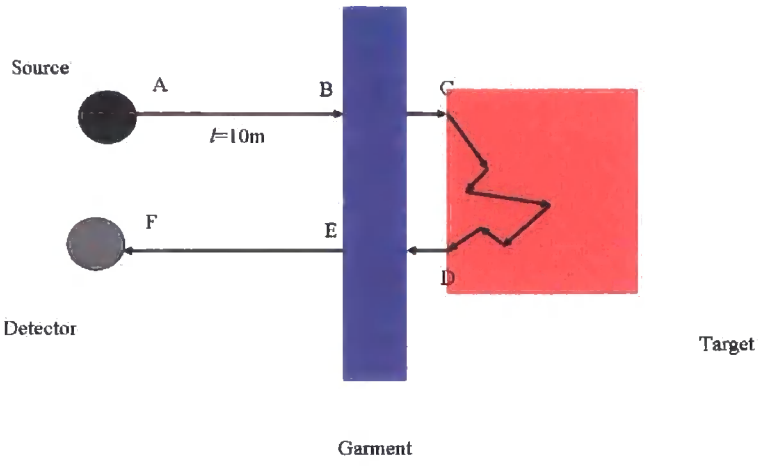

Figure 3.20: Schematic of stand-off detection system.

The source QCL is assumed to produce an output power of 1mW operating at 1.5 THz, whilst the minimum detectable signal by the bolometer is taken to be 1 pW. Note, that a considerably lower power could be detected if heterodyne detection was used. If the path length AB is 10 m, the beam is attenuated by approximately 22 dB, if we assume that the system is operating in the low absorption window. At 1.5 THz, a typical thick garment has attenuation of 13dB, taking a value between that of tweed and fleece.

Two extreme cases exist for detection of THz which has interacted with the sample and they are considered in turn:

1. The THz radiation passes (without scattering) through the clothing before being reflected from the surface of the target. It should first be noted that this specular reflection from the target does not occur in practice, but instead represents one extreme situation. The reflectance for some powdered sample, having refractive index of 1.5, is approximately 4% from the Fresnel equations (2.26). Therefore, a simple relationship exists between the total signal power at A and at F:

$$P_F = 0.04 \times 10^{-(2 \times cloth\ attenuation/10)} \times 10^{-(2 \times air\ attenuation/10)} \times P_A. \qquad (3.26)$$

This implies that $P_F = 4$ pW, and it is thus possible to detect the reflected signal. It should be noted however, that there would be considerable difficulty in determining

if a drug was present, since the minimum detectable quantity of drug produces fingerprint signals of the order of 3 % of the maximum.

This analysis can be generalised to relate the cloth attenuation (in dB), the distance AB (l) and air attenuation (in dB per metre) to the minimum detectable signal. For a signal to be detected:

$$38 \geq l \times (\text{air attenuation}) \times (\text{cloth attenuation}). \tag{3.27}$$

2. Diffusion of the THz radiation takes place in both the clothing and the target. For a typical target material, consisting of powder of average grain size of a few hundred microns, the simple mean free path formula indicates that MFP $\approx$ 0.5 mm at 1.5 THz. Therefore diffusion is a realistic model for THz propagation through a drug package having volume of 1 cm^3. In this case, there will be little energy loss in the clothing, but there is loss in the target at its characteristic fingerprint frequencies. Diffusion causes the energy of the beam to diverge in all directions, so the fraction reaching the detector is determined by the solid angle subtended by the collection optics at the target.

Consider a detection scheme with the conditions outlined above, with the added property that the area of the detection optics is A. To detect a signal, the following must be satisfied:

$$\text{Total loss (in dB)} = 2l \times 2.2 + 10\log\left(\frac{4\pi l^2}{A}\right) \leq 90. \tag{3.28}$$

For the case of A = 25 cm^2 and l = 10 m, the loss is 101 dB, so the signal is not received. Collection optics having area of the order 400 cm^2 would be required to detect the signal, and optics of this size are probably too large to be practical.

This very simple analysis indicates that stand-off THz detection of drugs (or explosives) concealed behind typical garments, requires stand-off distances of less than 10 m and/or very good collections optics. The collected signal size is considerably reduced by the significant attenuation effects within the target.

3.7 Summary and conclusions

This chapter of the work has discussed THz transmission through various non-homogeneous media. Understanding the effects of scattering is very important if broadband THz spectrometers are to be commercially exploited. From the broadband nature of the emitted pulses, non-identical spectral components will be absorbed and scattered differently to one another. These effects can give false positives in spectral signatures and reduce the detectable dynamic range of the signal, but can also be used to identify objects hidden in a matrix of other material.

After a discussion of the various scattering phenomena that are important to terahertz measurements, previous work in this general area was outlined. This indicated that conventional theoretical arguments do not provide a good fit to the results. Therefore, a simple model (PDM) has been developed to describe THz propagation in random media. This model has the inherent advantage in comparison with complete numeric solution of Maxwell's equations in that it provides reasonable predictions of THz transmission essentially instantaneously. These predictions are realised via simple algorithms using the MATLAB software package.

This model was tested by comparison with: exact results of scattering cross-sections using the Mie solution and numeric solution of Maxwell's equations; and various experimental measurements. These measurements on inhomogeneous materials, which are of interest as 'targets' in security and surveillance systems, are satisfactorily reproduced using the PDM. THz transmission through arrays of cylinders indicates that there are frequency regions of low and high transmission due to interference effects. The transmission peaks are satisfactorily reproduced for cylindrical arrays having a wide range of properties. A very good description up to 3 THz is provided by the Phase Distribution Model for THz transmission through both: a number of common fabrics; and non-absorbing powders. Using the results of these measurements and simulations it has been possible to provide a reasonable estimate of the feasibility of using THz as a "stand-off" detection technique. This analysis indicated that THz techniques would be far more appropriate in situations where the stand-off detection distance is not too large. It has also shown that considerable thought needs to be given to the design of the collection optics.

4. Signal processing methods for terahertz radiation

This chapter of the thesis presents work carried out as part of the TeraNova programme, to develop signal processing methods for terahertz pulses. At present, most THz research is undertaken using pulsed source and detector systems[110]. Whilst such systems have many advantages (e.g. their large spectral bandwidth allows the identification of unknown samples using spectral fingerprints) they also have various drawbacks. By their very nature, the emitters and detectors of such systems, usually based on semiconductor structures, produce various echoes and artefacts. These echoes and artefacts do not cause too much of a problem when measuring the frequency dependent transmission of a sample, but do cause confusion for example, if the temporal form of the pulse is being used to determine the sample's internal structure. The pulse returned from the sample may contain components having different delays, which can become confused with echoes from the source. Signal processing has the advantage of being able to suppress these unwanted echoes and allows, amongst other things, the determination of the presence of small objects or voids within a larger sample.

The signal processing methods discussed in this chapter extend and adapt mathematical strategies used in radar. In brief, the technique works by reconstructing the experimental data to produce a simple, single cycle input pulse, having frequency content within the bandwidth of the physical system and then showing the effect that the sample under test has on this reconstructed input. After outlining the mathematics of the signal processing technique, known as "THz pulse reconstruction," a series of experimental validations are given. These include: investigating THz transmission and reflection through slabs to mimic voids in media; and the response of various compounds to a sharply terminated input pulse.

Some of the results presented in this chapter have been published in: J.R. Fletcher, G.P. Swift, D. Dai, P.C. Upadhya and J.M. Chamberlain *Pulsed THz signal reconstruction*, App Phys **102** 113105 (2007). I am grateful to Dr. John Fletcher for the initial development of the signal processing algorithm, which has been used in the analysis of the experimental results. This mathematical method has also been patented[111].

4.1 Motivation for the development of terahertz signal processing techniques

In a THz TDS system a transducer device is used to convert one form of radiation (usually ultrashort pulses of infrared laser light) into THz radiation. Detection of this radiation proceeds in the inverse way to generation. A full explanation of such systems has already been presented in chapter two of the work. The radiation produced by such systems has been used to characterise the optical properties, over a wide spectral range, of a diverse range of materials, including: semiconductors[32, 34]; drugs of abuse[15]; explosives material[12]; and materials of biomedical interest[31].

In a typical pulsed THz spectroscopy system, a laser-triggered photoconductive source is used to generate the radiation, with detection taking place using either electro-optic or photoconductive sampling techniques[85]. In such a system there is little control over the time-dependence of the output pulse.

After generation of the initial pulse of radiation using a photoconductive source, which is radiated into freespace by the carrier acceleration, a number of subsidiary oscillations and after-runners are also radiated, many of which are unavoidable. These arise from the dynamics of the electron-hole pairs, amongst other things, within the semiconductor. Since THz radiation is generated in both directions by a photoconductive source, the radiation transmitted through the sample will be reflected within the substrate[74]. This results in delayed echoes of the initial THz pulse being emitted. These are also dispersed because they have propagated for a longer distance within the semiconductor substrate. Propagation through the atmosphere results in absorption at the resonant frequencies of water molecules[90]. Moreover, these are not independent effects. For example, echo pulses from the source can also excite water vapour oscillations, and echoes can arise in other places, notably in the detector. If the THz pulse is transmitted through a dispersive region, such as a waveguide, its different frequency components suffer varying phase changes and delays, further compounding the complexity of the signal. Consequently, the signal finally detected has a more complicated form than would be expected from the carrier motion alone.

It is very easy to see how these echoes from the source can cause confusion about the sample's structure if the source echoes overlap with pulses from the sample. The situation is further complicated if some of the signals returned from the sample are weak, for example pulses returned from interfaces with a low refractive index difference or pulses which have been multiply reflected with the sample. In this case, the weak signals may be obscured by the source after-runners.

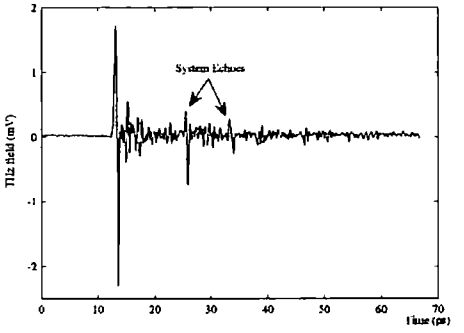

Figure 4.1: THz waveform, photoconductive emitter, electro-optic sampling, unpurged.

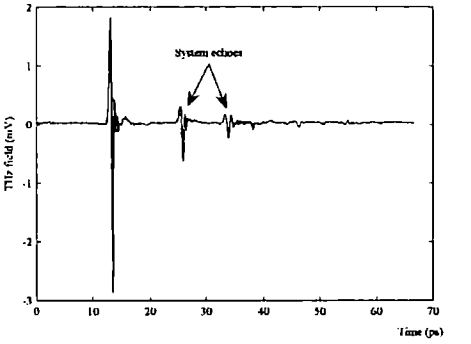

Figure 4.2: THz waveform, photoconductive emitter, electro-optic sampling, purged.

Figure 4.1 shows the electric field generated using a photoconductive switch, and detected with an electro-optic crystal for a THz pulse propagating through the atmosphere. Figure 4.2 is the identical THz pulse, but this time the atmosphere has been purged of water vapour, using nitrogen. Both of these pulses were generated using the standard transmission setup, described in chapter two. Comparison of the two waveforms shows that water vapour oscillations are quite powerful, and that the second and third system echoes merge into them.

To make the reflection measurements presented later in this chapter (section 4.4) and also to enable a THz scattering system to be built (chapters five and six), spectrometers using photoconductive switches as detectors, as well as sources, are required. Such systems are described in more detail in the appropriate places within the work, and it suffices here to show the typical electric field of a THz pulse generated and detected using such an arrangement. Figure 4.3 shows this waveform. This waveform excellently illustrates some of the experimental problems associated with the temporal form of THz waveforms: the first system echo is apparently of larger amplitude than

the main pulse. It should also be noted that when using a photoconductive antenna for

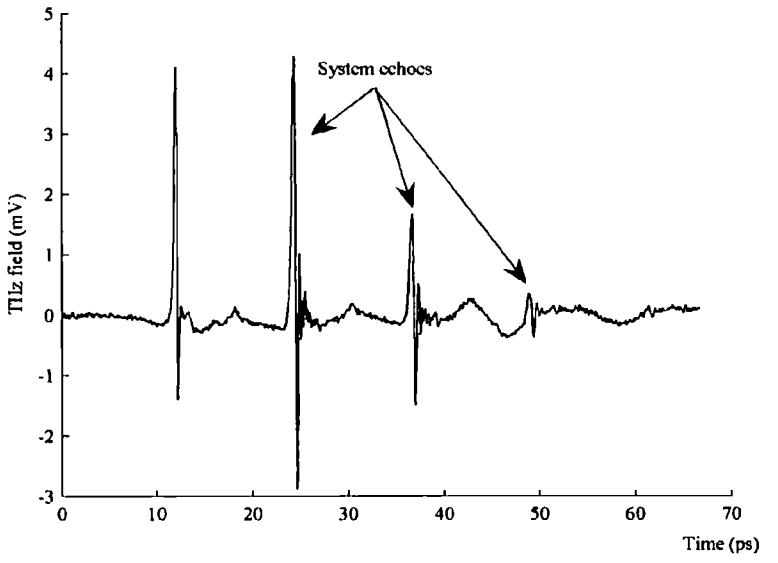

Figure 4.3: THz waveform, photoconductive emitter and detector.

THz detection instead of an electro-optic crystal, the effect of water vapour absorptions within the atmosphere are apparently less noticeable. This is because when this method of detection is employed, the signal to noise ratio of the system is less than for electro-optic detection. Therefore, the oscillations due to the propagation of the pulse through the atmosphere disappear into the background signal more quickly.

As already described in the introduction, these after-runners are not disabling when measurements of the frequency dependent transmission of a specimen are being made. In such a measurement, the main criterion is the frequency content of the incident and transmitted signals. However, if a system is built whose function is to use the time delays of the pulses returned by a sample to help build up a picture of its internal structure, it would be desirable to have a single simple source pulse. Such a pulse would remove confusion arising from sample and source echoes, especially when the sample echoes are weak. The pulse reconstruction algorithm described below addresses these problems. Numerical processing of the sample signal, together with a reference signal, which has been separately recorded, removes the undesired effects of the source after-runners. As a result of this reconstruction method, the pulse recorded from the sample shows what the sample signal would have been had it been illuminated by a single, simple input pulse, having spectral content within the bandwidth of the source.

The reference signal is produced in such a way that it includes all the distorting effects of the system, but without the influence of the sample. In transmission measurements, the reference signal is simply that detected without the sample in the THz beam path, whereas in a reflection measurement, the reference signal is obtained by replacing the sample with a plane mirror.

4.1.1 Other forms of terahertz signal processing

THz signal processing is still very much in its infancy. However, some other work has been done in this general area. Dragoman and Dragoman[112] have applied optical signal processing techniques, such as fractional Fourier Transforms and spectrograms to THz pulses. In the work that Mittleman's group undertook on imaging, which is described in more detail in chapter six, an algorithm was developed to process numerically THz temporal waveforms, reflected from layered structures[113]. This processing, which involves division of the Fourier Transforms of the reference and sample waveforms by a low pass filter, as well as application of Fourier deconvolution, produces a temporal waveform consisting of sharp spikes corresponding to the positions of pulses reflected from the various interfaces.

4.2 Principle of pulse reconstruction

Pulsed THz sources are, by their nature, very low in power; it is only the incredible sensitivity of coherent techniques that allows them to be detected with so great a dynamic range. When THz pulses impact on a sample they only induce a first order response, i.e. the response of the sample is linearly proportional to the input field. Therefore, the signal, $s(t)$, emerging from the sample can be simply written as a convolution of the electric field of the source pulse, $f(t)$, arriving at the sample with the impulse response function, $g(t)$, for the sample:

$$s(t) = g(t) \otimes f(t). \tag{4.1}$$

The response function, for a unit impulse at $t = 0$, is in general a sum (or integral) of delayed impulses at times $t_p \geq 0$ with amplitudes A_p,

$$g(t) = \sum_p A_p \delta(t - t_p). \tag{4.2}$$

Thus, the signal emerging from the sample is of the form:

$$s(t) = \sum_p A_p f(t - t_p). \tag{4.3}$$

By applying a suitable transformation to the source pulse, a reconstructed input pulse, $\tilde{f}(t)$, can be generated, which has frequency content within the actual source bandwidth. This transformation can be calculated by taking a convolution of a transformation generating function, $u(t)$, with $f(t)$, and it is represented by:

$$\tilde{f}(t) = u(t) \otimes f(t). \tag{4.4}$$

Application of this transform generating function to the pulse which has propagated through the sample produces the reconstructed sample signal:

$$\tilde{s}(t) = u(t) \otimes s(t) = \sum_p A_p \tilde{f}(t - t_p). \tag{4.5}$$

Therefore, the reconstructed sample signal, $\tilde{s}(t)$, is the actual response that the sample would have if it was illuminated by the reconstructed source pulse, $\tilde{f}(t)$. The transformation generating function can be chosen in many ways, but it should result in a new input that satisfies several conditions, which are now discussed.

4.2.1 Input pulse choice

The purpose of the pulse reconstruction method is to "clean-up" the temporal form of the THz electric field. A necessary requirement of such software is to clarify the observation of time-separated return signals from the sample. Since these may be quite closely spaced, the reconstructed input signal must be both well localized in time, and not contain any significant fore- or after-runners. Conversely, it should be remembered that the frequency content of a pulse is dependent upon its width. Therefore, the length of the input pulse is limited by the bandwidth of the source and so a trade-off exists: keeping the length of the input short enough so that it can resolve time intervals between sample echoes; but at the same time ensuring that the input is not so short that its frequency spectrum extends significantly beyond the range of the THz source.

The noise content of the reconstructed sample signal increases as the input signal becomes shorter. Therefore, when choosing the transformation, $u(t)$, which acts on a given source signal, $f(t)$, to produce the new sample input, $\tilde{f}(t)$, a compromise between time resolution and noise filtering is required. Choosing a reconstructed input, whose frequency spectrum goes to zero above some chosen cut-off frequency optimises this by eliminating any higher frequency noise components. By minimising the fore- and after-runners of the reconstructed input as much as possible, the problem of hiding

weak signals in the presence of stronger ones is reduced. Similar problems have been overcome in the radar frequency range and the solution to these problems is discussed in the literature[114].

Thus, to use this technique of signal processing, a set of input functions, which has sufficient flexibility to allow for variations in the spectra of different THz sources ideally needs developing. Of course, besides the obvious high frequency cut-off of a THz source, most of them are also deficient in power below a certain frequency and so have a low frequency cut-off. A set of input functions, based on the binomial distribution, have sufficient flexibility to provide for the various cut-offs of individual sources.

Binomial forms: The behaviour of the spectrum of the reconstructed input pulse, $\tilde{f}(t)$, as it approaches the high frequency cut-off, f_c, determines the amplitudes of any subsidiary fore- and after-runners of its temporal form, $\tilde{f}(t)$. Problems arise with large subsidiary amplitudes if the spectrum goes discontinuously to zero. So, by designing a reconstructed input whose spectrum, along with its first few derivatives, go smoothly to zero at the cut-off frequency, the reconstructed input will only have a few small subsidiaries close to the main peak.

The frequency spectrum, $\tilde{F}(\omega)$, of the reconstructed input, $\tilde{f}(\omega)$, is taken to be:

$$\tilde{F}(\omega) = e^{i\omega t_0}\left[\cos\left(\frac{\omega}{4\pi}\right)\right]^p\left[\sin\left(\frac{\omega}{4\pi}\right)\right]^q, \qquad |\omega| \le 2\pi f_c, \qquad (4.6a)$$

and:

$$\tilde{F}(\omega) = 0, \qquad |\omega| > 2\pi f_c, \qquad (4.6b)$$

where t_0 is the time of arrival of the main part of the source pulse. The cut-off frequency is taken to be less than the effective range of the source as already outlined. Suitable choice of the arguments of the trigonometric factors means that the frequency spectrum is continuous at the cut-off frequency. The other two degrees of freedom when designing the form of the reconstructed input pulse come in the choice of values of the two non-negative integers p and q. These are chosen to suit the spectrum emitted by a particular source, and in most cases p can be taken to be a small integer with

$q = 0$. The input pulse therefore has a single maximum and is of width $\sim f_c^{-1}$. The integer q can usefully taken to be non-zero when the source also has a low frequency cut-off, below which it is lacking in power. For q non-zero, the input pulse becomes cyclic, having $(q+1)$ half-cycles. As the quantity $(p+q)$ becomes larger in value, the subsidiary oscillations of the temporal reconstructed input are more strongly attenuated. This must be taken into account when looking for the presence of a weak pulse near a strong one.

Generation of the spectrum of the reconstructed input is possible by numerically solving equations (4.6a) and (4.6b). Expansion of the trigonometric factors, expressed in their complex exponential form produces the required binomial coefficients. However, it is more convenient to generate the spectrum of the reconstructed pulse by using the fast Fourier Transform of some simple 'seed' function. This seed is most easily generated by convolving together p identical factors of type A, with q identical factors of type B, where:

$$A = \left[\delta(t) + \delta\left(t - \frac{1}{2f_c}\right)\right] \Big/ 2, \tag{4.7a}$$

$$B = \left[\delta(t) - \delta\left(t - \frac{1}{2f_c}\right)\right] \Big/ 2. \tag{4.7b}$$

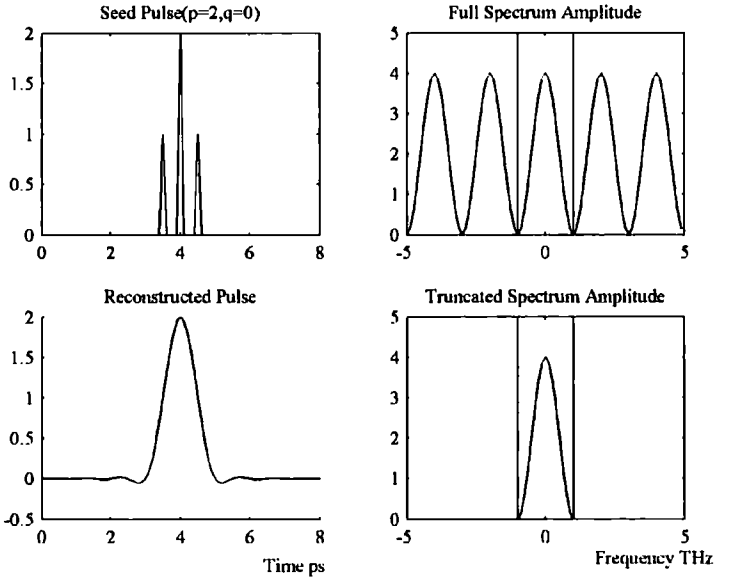

Figure 4.4: Example seed and reconstructed source pulse forms.

The convolution results in a seed function, consisting of a collection of δ functions, having binomial amplitudes. If the factor q is non-zero, these coefficients also have

oscillating signs. Once the spectrum has been generated, it is cut-off (sent to zero) above $\pm f_c$. Inversion of the Fourier Transform then produces the temporal input pulse. Figure 4.4 shows an example of seed and pulse forms.

4.2.2 Reconvolution of the filtered signal

Equation (4.4) relates the temporal form of the source pulse to the required transformation, and this can be written as:

$$U(\omega) = \frac{\widetilde{F}(\omega)}{F(\omega)} \tag{4.8}$$

in the frequency domain. Using equation (4.5) allows the form of the reconstructed sample spectrum to be found:

$$\widetilde{S}(\omega) = S(\omega)\frac{\widetilde{F}(\omega)}{F(\omega)}. \tag{4.9}$$

In the above two equations, the capital letters represent Fourier Transforms.

4.2.3 Elimination of artefacts from the reconstruction

The signal processing method, which has just been described, is a powerful technique for the analysis of THz waveforms in the temporal domain. Sections 4.3 to 4.6 of this work show its application to experimental problems. However, if the method is simply applied as stated above, a number of spurious effects can still appear in the reconstruction. These arise from: signal truncation, whereby the scan length is not sufficiently long to record a sample echo with long delay; and the effects of noise due to water vapour, since these resonances are present in both the source and the sample signals. By the addition of further processing techniques to the numerical method, these spurious effects can be eliminated.

Signal truncation: By the very nature of their mathematical construction, Fourier Transforms are periodic. Consequently, the fast Fourier Transforms used numerically to process the signals have the implicit assumption of periodicity beyond the recorded range. If the experimental sample signal is truncated before an echo component having large time delay is recorded, spurious signals appear in the reconstructed sample signal, which precede the incident pulse. Application of a suitable exponential convergence factor can remove these artefacts. Firstly, the recorded source signal (the reference signal used in the reconstruction) and sample signal are multiplied by a decreasing

exponential, $\exp(-bt)$. After applying the signal processing technique, the reconstructed signals are multiplied by an increasing exponential, $\exp(bt)$. The application of these exponential functions minimises the effects of this truncation. Parameter b is chosen so that the recorded signals are reduced smoothly towards zero at the end of the time scan.

Water vapour absorption: As is well known, when THz radiation passes through the atmosphere, it is sharply absorbed at several resonance frequencies[90]. These resonant absorptions have the effect of reducing the THz signal to noise ratio at their relevant frequencies, and this noise is apparent in both the source and the sample. Inspection of equation (4.9), used to determine the frequency spectrum of the reconstructed sample pulse, shows that the reconstruction will contain narrow bandwidth noise at the water vapour resonances. At these discrete resonant frequencies one noisy spectral component is divided by another spectral component, which has also been reduced to noise at that point, but the other frequencies will not be affected. Therefore, the reconstructed pulse spectrum consists of isolated noise peaks at the water vapour resonances, with lower noise over the remainder of the frequency range. The simplest way to remove this noise is by application of a narrow band filter.

The Fourier Transform of the reconstructed sample pulse is a rapidly oscillating function. However, if its phase factor, $\exp(i\omega t_0)$, is removed, the rapid oscillations of the real and imaginary parts are reduced everywhere in the reconstruction, except at the water vapour resonances. At these discrete frequencies they may be anomalously large positive or negative values. Since the resonances are very narrow band, the effect of the noise peaks they create can be removed from the reconstruction by replacing the discrete value of the reconstructed amplitude by the average of the reconstructed amplitudes on either side of this point. In other words, $a(n)$ is replaced by $\frac{1}{2}[a(n+1)+a(n-1)]$ when

$$[a(n)-a(n-1)][a(n)-a(n+1)]>C, \tag{4.10}$$

where $a(n)$ is the nth component of the real or imaginary part of the Fourier Transform. The cut-off level, C, chosen above which the filter is applied, must be large enough so that only anomalous values are altered whilst the remaining values are unchanged. Once the filtering has taken place, the phase factor is replaced and the reconstructed sample spectra can be "reconvolved" to produce the reconstructed output

pulse. It should be noted that this form of filter does not reduce the information content of the reconstructed signal.

4.2.4 Choice of parameters

The technique of pulse reconstruction described above has sufficient flexibility to allow it to be successfully used in a wide range of applications. The choice of parameters used in the mathematical method is dependent upon the application in mind for the technique. Currently, the best choice for the parameters is obtained by inspection of the reconstructed pulse and its spectrum. However, a number of general principles exist, which can be used when the first reconstruction attempt is carried out.

By taking the parameter p to have a value of two, most signals can be suitably reconstructed. A value of two means that the amplitudes of the subsidiary oscillations of the reconstructed source pulse signal are less than 3% of the main peak. In an application which requires the detection of a weak signal in the vicinity of a strong pulse, the value of this parameter will need increasing. This has the effect of reducing the fore- and after-runners of the input pulse, and thus the strong pulse seen in the reconstructed signal, even further. It has already been explained that the parameter q affects the number of half cycles in the main reconstructed pulse. Thus, by taking $q = 0$ the reconstructed source pulse is a single positive peak with small oscillations, dependent on the value of p, either side of it. It is very easy to determine the relative signs of the pulses returned from the sample. However, for sources which are not very powerful at low frequencies, taking $q = 0$ may result in the appearance of excessive noise at the low frequency end of the spectrum of the reconstructed signal. This noise can be reduced by taking a larger value of q, which gives an incident source pulse with $(q+1)$ half-cycles of alternating signs. Such an incident source pulse contains less low frequencies and so reduces the noise in this regime. However, incident pulses with more than one half-cycle can lead to confusion in the interpretation of close or overlapping sample pulses, with positive half-cycles partially cancelling negative ones.

The other parameter which can be changed from reconstruction to reconstruction is the cut-off frequency, f_c, which controls the time resolution limit $\sim 1/f_c$. It is chosen to satisfy the maximum frequency response of the source and detector. Too high a cut-off

frequency results in excessive noise at high frequencies within the reconstruction. In this case, the spectra of the actual source, $F(\omega)$ will have small random values within the range where the reconstructed spectra, $\widetilde{F}(\omega)$ is non-zero. As the cut-off frequency is lowered, the noise is correspondingly reduced, since more of the very low powered high frequencies generated and detected by the system, are zeroed in the reconstruction algorithm. However, since the inverse of the cut-off is proportional to the time resolution of the system, reducing the cut-off decreases the temporal resolution of the reconstruction method. Within the numeric reconstruction algorithm, outlined in section 4.2.5, the cut-off frequency is defined by a parameter, r. Increasing the value of r, reduces the cut-off frequency. In fact, the cut-off frequency is defined to be the Nyquist frequency of the system divided by r. The Nyquist frequency is half of the sampling frequency of a discrete signal processing system, which in our case is half of the maximum frequency of the discrete Fast Fourier Transform.

The convergence factor parameter, if required, is taken to be a small multiple of the inverse time scan length. It is apparent in the reconstructed pulses if a convergence factor is needed, since on inspection, a spurious precursor is seen before the main pulse that is directly transmitted through the sample. However, it is preferable to increase the scan length to remove the signal truncation, if possible, as opposed to using a convergence factor.

To remove the effects of water vapour absorptions from scans which have taken place in a non-purged atmosphere, a cut-off level needs setting for the filter. This is done by averaging the left side of equation (4.10) over the length of the data and operating the cut-off when the local value exceeds the average by a chosen factor (e.g. 15). It is possible to check the results of the filtering by examination of the spectrum of the reconstructed signal. Some spectra contain one single very large anomaly, with several smaller anomalous values at other frequencies. The first application of the filter will thus only remove the largest noise component, and a further second application of the filter is required to remove the remaining smaller anomalies.

4.2.5 Numerical application of the reconstruction technique

As has already been explained, the reconstruction process takes place numerically and proceeds in the following way:

1. Two vectors of the A and B factors, defined in equations (4.7) are produced. These are convolved together (p factors of type A and q factors of type B) to produce the seed pulse.
2. The spectra of the source and sample pulses are calculated by Fast Fourier Transform. Note, if the waveforms have been detected using a photoconductive antenna, they are first numerically levelled, to remove the non-zero, slowly varying background.
3. The seed pulse is Fast Fourier Transformed.
4. A truncation of the source and sample spectra is undertaken to remove high frequency noise. All spectral components having frequency above the cut-off are sent to zero.
5. Deconvolution of the source and sample spectra takes place, to produce the spectral content of the reconstructed pulses, as follows:

$$\text{Reconstructed (source/sample) spectrum} = \frac{\text{Truncated (source/sample) spectrum} * \text{Seed spectrum}}{\text{Complete source spectrum}}.$$

6. The deconvolved sample spectrum is dephased, before narrowband noise is removed by application of the appropriate filters, after which the sample spectra is rephased.
7. The deconvolved source and rephased sample spectra are then converted back into the time domain by inverting the Fourier Transforms.

After application of the above numerical methods, echoes and oscillations in the initial recorded source and sample pulses have been removed and two "clean" temporal pulses exist. A simple reference pulse, whose spectral content is within the bandwidth of the actual source, and the response of the sample to this reconstructed reference signal.

4.3 Validation of the pulse reconstruction method using transmission measurements

Numerous experiments have been undertaken to validate this mathematical algorithm. The first of these involved measuring reflections of THz radiation within a sample that

would in someway mimic a void (defect) or impurity concealed within a larger matrix of some other material.

As is well known, pulse reflections will take place at the various interfaces within a layered sample, with the amplitude of the pulse being given by the Fresnel equations (2.27) for each reflection. In the case of transmission measurements, pulses reflected within the layers must undergo two reflections to exit the sample in the same direction as the incident beam. Two applications of the Fresnel equations are required to determine the amplitude of the various pulses delayed within the structure. Figure 4.5 shows examples of possible reflection paths within a two-layered sample (with separation δ) but it should be noted that this is not exhaustive.

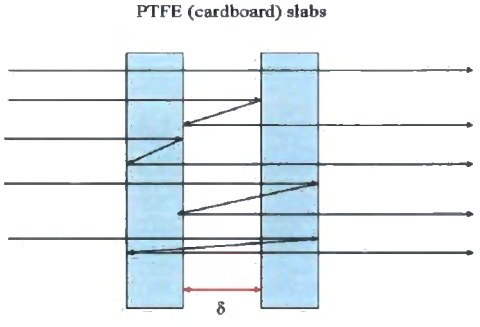

Figure 4.5: Example pulse paths for reflections at interfaces of media having a refractive index difference.

Measurement of the transmitted pulses, reflected twice in the sample, provides a method of measuring the positions and thicknesses of the layers. As the gap is altered between the layers, pulses reflected twice within the various gaps will at times begin to merge and overlap, and thus get lost in the background structure of the incident pulse. The results now presented show that use of post-detection software routines can "clean-up" the THz signals significantly, making it possible to determine much smaller gap sizes than is possible from investigating the raw data alone.

Transmission of THz pulses was investigated through two slabs of various materials, with a varying gap between them, using the standard THz transmission setup previously described in chapter two. The first, stationary, slab was placed with its back surface

(furthest from the emitter) at the THz beam focus, whilst the second slab was placed nearer to the receiver on a translation stage, allowing the gap between the slabs to be varied from 5 mm to 10 μm. Two different materials were chosen to make the slabs from: PTFE sheet and cardboard. For the PTFE, which has a refractive index of 1.42 in the THz region, two different sets of measurements were performed. First, transmission was investigated through two identical pieces of manufactured PTFE sheet of thickness 1.55 mm, whilst the second set of measurements was performed using two slabs of PTFE cut from a block, having non-identical thicknesses of 2.39 and 2.45 mm. The card pieces were identical, of thickness 340 μm having a THz frequency refractive index 1.36.

To enable the application of the post signal reconstruction software, two signals need to be recorded. A reference scan, taken without the sample in the system followed by the THz signal transmitted through the layered object under investigation.

4.3.1 Transmission through slabs of PTFE

The initial measurements presented here are for THz transmission through the two identical sheets of PTFE, cut from the manufactured sheet. Figure 4.6 shows a reference pulse from the THz spectrometer (blue) and the THz pulse transmitted through the PTFE slabs with a 1mm gap between them in an atmosphere of air (red). Figure 4.7 shows the identical pulses, but this time when the experiment has taken

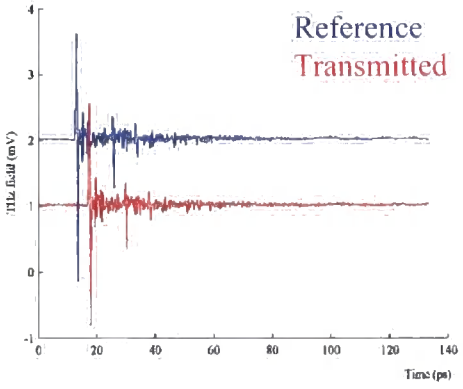

Figure 4.6: Reference THz pulse and pulse transmitted through PTFE sheets with a 1 mm gap (unpurged atmosphere).

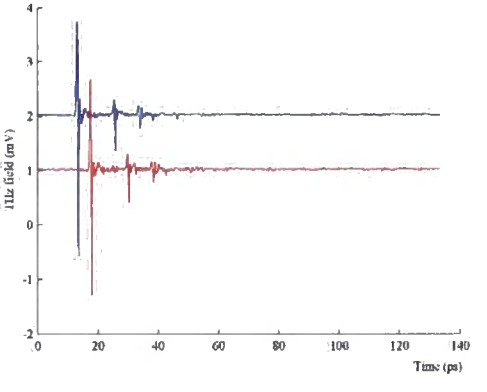

Figure 4.7: Reference THz pulse and pulse transmitted through PTFE sheets with a 1 mm gap (purged atmosphere).

place in a purged atmosphere. A simple calculation, using the Fresnel equations, indicates that any reflections taking place within the sample will be of an amplitude of

the order of 3% of the directly transmitted amplitude – at each reflection just over 17% of the incident pulse amplitude is reflected.

Inspection of the signals reveals that they are essentially the same, with the transmitted sample signal being a delayed version of the reference one. The numerous oscillations between the main pulse and the system echoes in figure 4.6 are a result of absorption by atmospheric water vapour. These absorptions conceal the presence of signals reflected twice within the sample. When the experiment takes place in a purged atmosphere, the absorptions are removed and the echo THz pulses from the experimental system can be much more clearly seen. Slight differences between the shapes of the source and sample signals can be made out when the experiment has taken place in a purged atmosphere; but the changes are very small and it is impossible to attribute them to anything.

Reconstruction of the experimentally recorded signals then took place. Figure 4.8 shows the reconstruction of the unpurged reference pulse and the pulse transmitted through the two slabs having a gap of 1 mm between them. The parameters used for this reconstruction were $p = 2$, $q = 0$, $r = 3$. Again, the blue pulse is the reconstruction of the source, whilst the red pulse is the reconstruction of the sample signal. Clearly, the input signal has been "cleaned" of both water vapour absorptions and system echoes, whilst the structure evident in the reconstructed sample signal at longer times is due to internal reflections and absorption processes within the sample. Any phase changes introduced by the sample correspond to simple time delays since PTFE is non-dispersive over the frequency range of the transmission spectrometer.

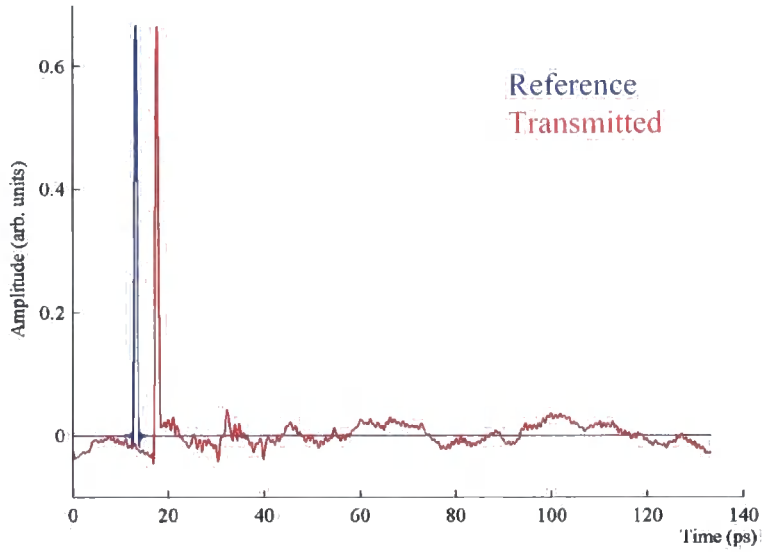

Figure 4.8: Reconstructed source and sample signals, transmitted through PTFE sheets with a 1 mm gap, obtained in an unpurged atmosphere.

An enlargement of the first 60 ps of the reconstructed signals is shown in figure 4.9 below. The black pulse (offset for clarity) represents a theoretical simulation of the response of the system to the seed pulse, which has been formed using the reconstruction parameters stated above, calculated via a transfer matrix method. The peaks in this signal correspond to internal reflections at the system interfaces. Thus, the

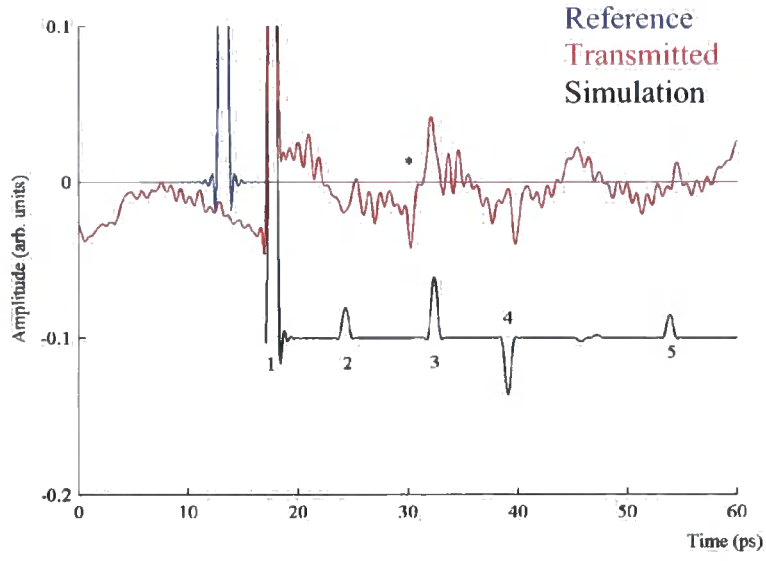

Figure 4.9: Enlarged reconstruction signals, with simulation using transfer matrix method for transmission through PTFE sheets with 1mm gap in an unpurged atmosphere.

peaks of this simulated pulse are: (1) after 17.6 ps the directly transmitted pulse; (2) after 24.3 ps is the pulse which passes through the first slab, is reflected twice in the air

gap and then passes through the second slab; (3) at 32.4 ps the pulse which is reflected twice inside one of the slabs, but passes directly through the other; (4) with delay 39.1 ps the pulse which passes through the first slab, is reflected from the front (or back) surface of the second slab, and then the front (or back) surface of the first slab; and (5) after 53.9 ps passes through the first slab, is reflected from the back surface of the second slab, off the front of the first slab and finally is detected. The reflected peak labelled (4) has undergone a relative phase reversal, since an odd number of reflections at air to slab (low to high refractive index) interfaces are required to produce it. It should also be noted that the amplitudes of the reconstructed peaks are in agreement with the predictions of the Fresnel equations. Of course, peaks (3) and (4) have twice the amplitude of peaks (2) and (5) since two possible identical reflection paths contribute to these reflections. One other peak exists in the actual reconstructed signal at 30.2ps, marked (*). Its origin is unknown, but is probably due to leakage of a system echo through the reconstruction algorithm.

The table below lists the time values of the maximum amplitudes of both the simulated and experimentally reconstructed signals, for transmission of a THz pulse through two sheets of PTFE with a 1mm gap.

Simulated (ps)	**Actual (ps)**	**Description**
17.63	17.60	Directly transmitted pulse
24.33	25.20	Reflection in air gap
32.43	32.20	Reflection in one slab
39.13	39.80	Reflection in one slab and air gap
53.93	54.40	Reflection at outer extremities of structure

From this table, it is clear that internal reflection delays found using the reconstruction process are in good agreement with the peak times expected after simulation of a pulse through a layered structure using a transfer matrix method. The slight discrepancies, which tend to be more noticeable at later times, arise because the experiments are carried out using a focused beam. After undergoing multiple reflections the beam begins to diverge, decreasing the overall collection efficiency of the setup which smears out the pulses. It is also apparent that, without the "cleaning-up" procedure applied to

the signals after they have been detected, these small internal reflections would not be seen.

Figure 4.10, below shows the same reconstructed sample pulse (red) but after it has undergone further signal processing, by application of the narrowband filtering process to remove the outlying points. The black pulse in this figure is the identical, filtered reconstruction, but this time applied to pulses recorded in a purged nitrogen atmosphere. The vertical blue bars represent the calculated pulse times, which are simple to calculate, being the time that an electromagnetic wave takes to travel through the relevant optical thickness. From these two curves, it is clear that conducting the experiments in a purged atmosphere has no real advantages if post detection signal processing routines are applied. Both sets of results clearly reveal the pulses reflected within the sample system. However, the non-zero background is slightly reduced, and also flattened when the experiments are carried out in the purged atmosphere.

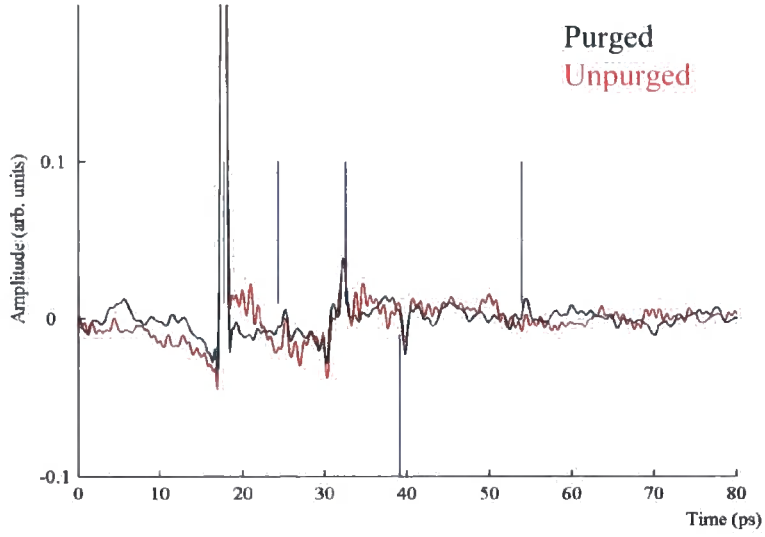

Figure 4.10: Filtered reconstructed sample signals, for transmission through PTFE sheets with a 1 mm gap.

Figure 4.11 shows the relative delays of sample reflections obtained after reconstructing experimental data for experiments in which THz pulses have propagated through two sheets of PTFE with a varying gap between them, ranging from 10 μm to 5 mm. In it the experimentally determined delays are represented by the circles, with the

black lines showing the times of the expected delays. The two curves running parallel

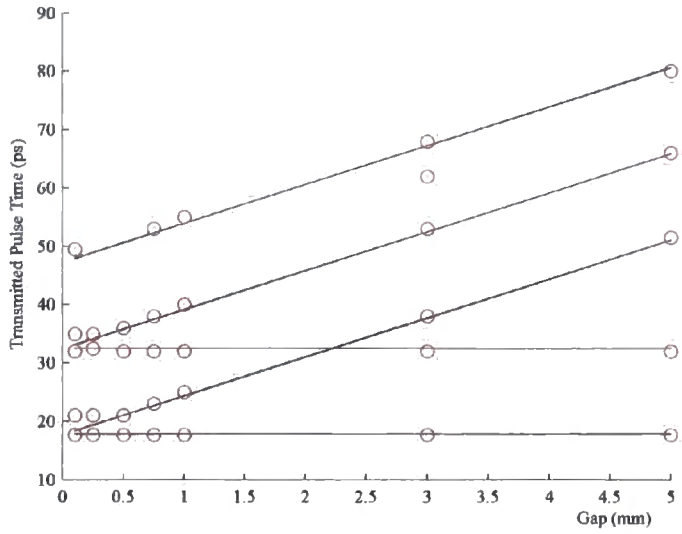

Figure 4.11: Experimentally obtained delays for pulses transmitted through two sheets of PTFE with a varying gap between them.

to the x-axis represent the directly transmitted pulse and a pulse reflected in one slab, delays which are constant with gap size. The lines representing the delays, which increase with gap size, are for reflections in the air gap and zero, one and two PTFE slabs respectively. A resolution of 500 μm between the two slabs is easily seen with this setup.

A similar set of measurements was taken for transmission through two slabs of PTFE having non-identical thickness. The results obtained were very similar to those found for transmission through identical sheets of PTFE, but in these measurements the pulses reflected within the different slabs have slightly different delays. One such measurement is shown below, for the two slabs having thickness 2.39 mm and 2.45 mm respectively, with a 0.5 mm gap. This figure (4.12) just shows the reconstructed sample signal, with parameters $p = 2$, $q = 1$, $r = 3$, and the expected times of the reflected pulses, obtained from the optical delays. Different values of the reconstruction parameters have been used to show how a non-zero q value can lead to confusion in the interpretation of the results if the structure of the sample under test was not known.

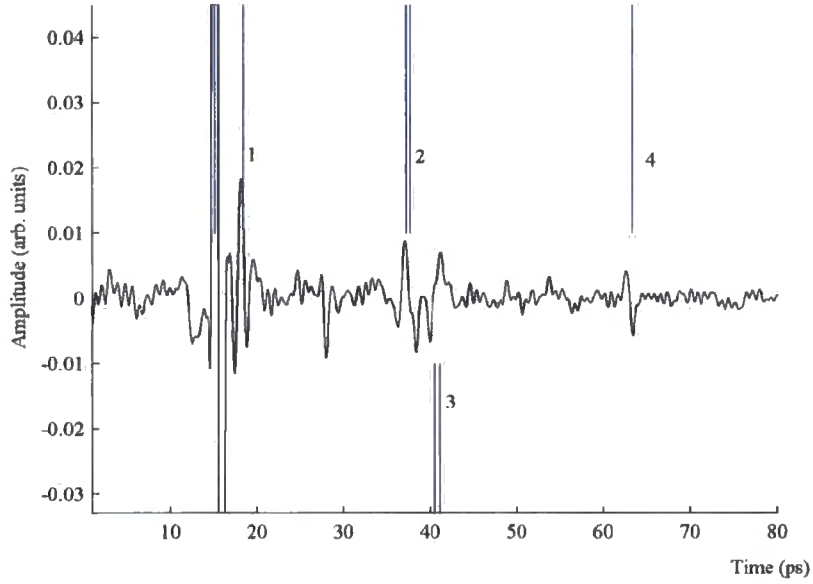

Figure 4.12: Reconstructed signal for pulse transmitted through two non-identical slabs of PTFE.

In the above figure, pulse (1) is that reflected in the air gap; the pulses (2) are those reflected once in each slab; whilst the reconstructed pulses (3) are those which have been reflected in the air gap and one slab respectively; and pulse (4) is that reflected within the structure as a whole. Since the thickness difference between the two slabs is relatively small (60 μm) the pulses reflected from within each slab only partially overlap. This can be seen by: the presence of two simulated times at pulses (2) and (3); and the splitting of the experimental reconstruction in two, with a small section of zero amplitude pulse (where destructive interference has taken place) between the first and second half cycles.

4.3.2 Transmission through sheets of cardboard

A further set of validation experiments was carried out for THz transmission through the two identical sheets of cardboard. Again, similar results were seen to those presented above. Comparison of the reference waveform with that transmitted through the sample again indicated that the transmitted wave was essentially just a delayed copy of the original. This time, the reflected pulses have even smaller amplitudes relative to the directly transmitted pulse, just being some 2.3% of it. Figure 4.13 shows the relative delays for each gap size between the two sheets. The red circles indicate the experimentally obtained delays, with the black lines being the calculated delays. It is immediately apparent that the experimental delays for any pulses reflected in the gap

and zero, one or two sheets of cardboard are: quite good for small gaps, but are longer

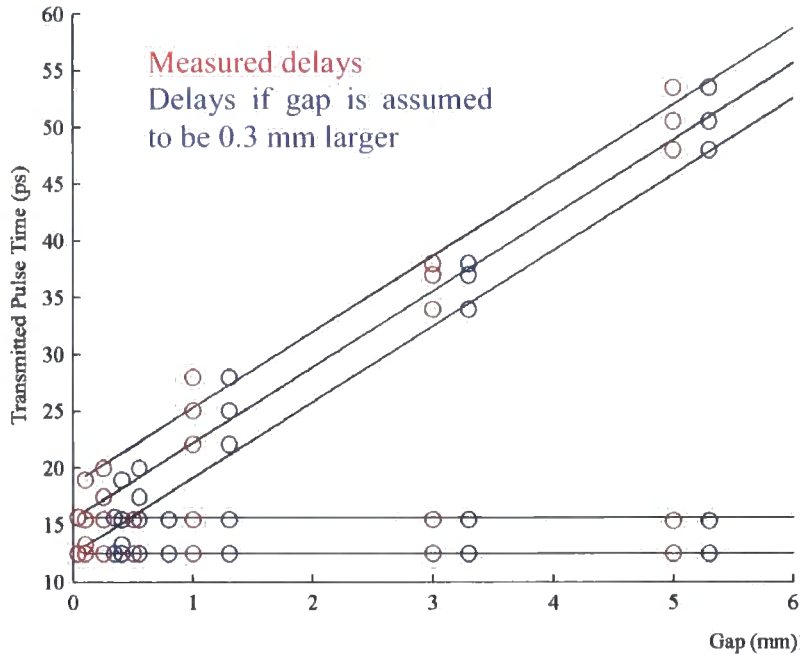

Figure 4.13: Experimentally obtained delays for pulses transmitted through two sheets of cardboard with a varying gap between them.

than expected when the gap is larger. For gaps of size greater than 1mm, a much better match is seen if the experimental gap is assumed to be 0.3 mm wider, indicated by the blue circles.

The root cause of this inconsistency is assumed to arise from the lack of rigidity of the cardboard sheets. At small gaps, the two sheets of cardboard are well aligned, but as the gap is increased, one (or both) cardboard layers must 'bow' within its support, thus altering the distance between the pieces at their centres, where the THz beam passes.

4.4 Validation of the technique using reflection measurements

A second set of measurements was undertaken to validate the reconstruction method, but this time a form of reflection geometry was used. Reflection measurements are more akin to measurements that would be taken in a realistic situation. A description of the design, construction and testing of this system is given in section 4.4.1. To investigate the minimum gap size between slabs that can be resolved using the reconstruction technique, THz pulses were focused onto the back surface of slab of a PTFE sheet. A second slab of PTFE was then mounted on a translation stage behind

this front slab, so that gap sizes of between 5 mm and 10 μm could be set between the back surface of the front slab and the front surface of the back slab. The reference signal required for the reconstruction from these measurements was recorded by replacing the front slab with a mirror, which reflected the THz beam.

Once again, pulse reflections take place at various interfaces within the layered sample, with the Fresnel equations giving the pulse amplitude. Only one reflection is required at an interface for a reflected pulse to be recorded in this set-up. Consequently, only one application of the Fresnel equations (2.27) is required to determine the expected amplitudes of the delayed pulse. However, for this scenario, phase reversal of the pulse takes place at interfaces from low to high refractive index, as indicated by the equations. Figure 4.14 shows examples of possible reflections within a two-layered sample, but similarly to the transmission case this is not exhaustive.

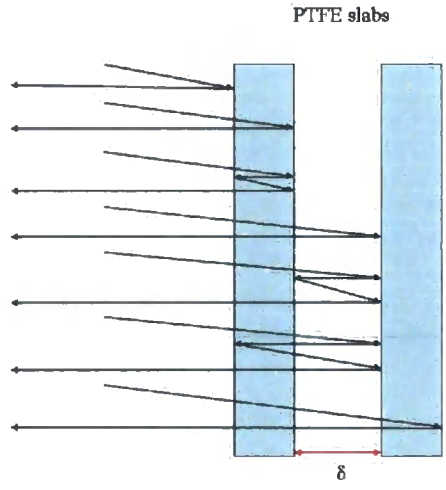

Figure 4.14: Example pulse paths for reflections at interfaces of media having refractive index difference.

4.4.1 Design and construction of a terahertz reflection spectrometer

The THz frequency reflections reported here were carried out using a modified THz frequency TDS arrangement, shown schematically in figure 4.15. The emitter geometry

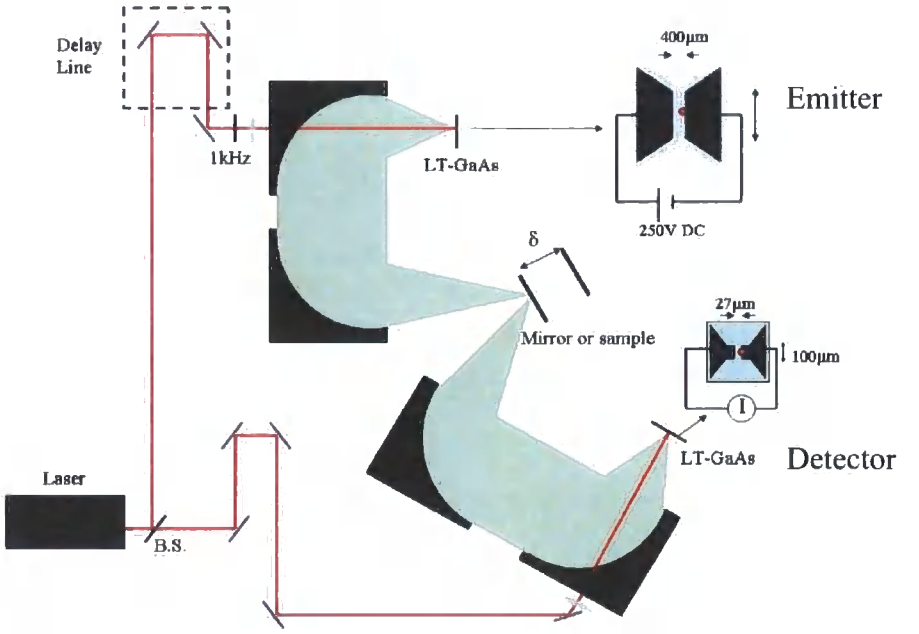

Figure 4.15: Schematic of THz reflection spectrometer.

shown was similar to that used in all experiments, whilst the detector geometry is the modified design, described in section 4.4.2. Figure 4.16 is a photograph of the THz

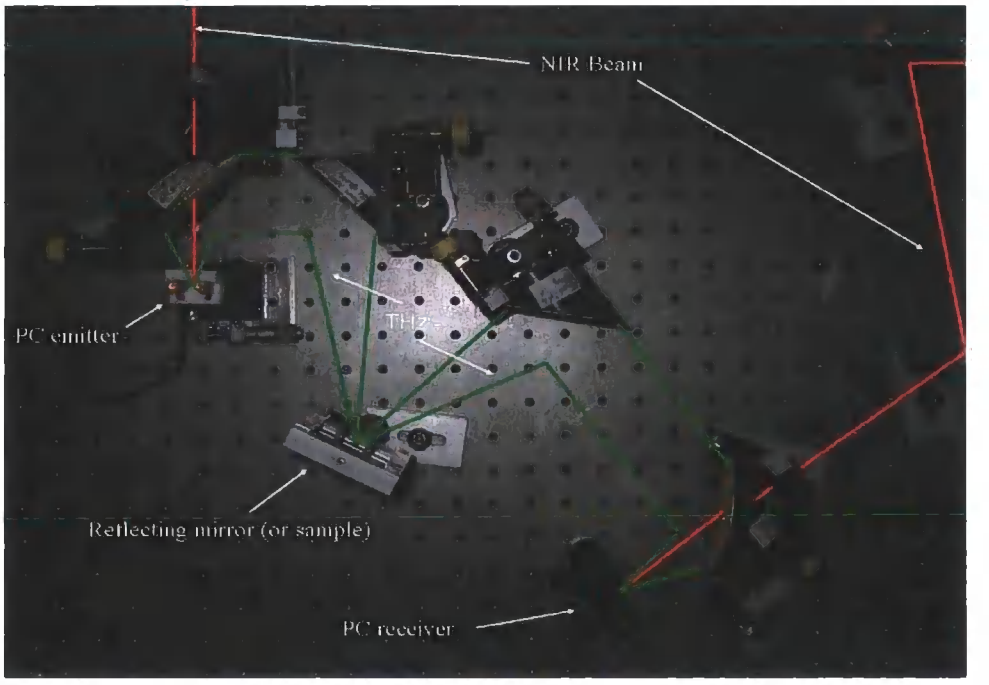

Figure 4.16: Photograph of THz optics in reflection spectrometer.

optics, showing the relative positions of the infrared and THz beams. After generation of the THz frequency radiation, using a photoconductive emitter with 400 μm gap, it was collected and collimated using a parabolic mirror of focal length 5 cm. It was decided to collect the THz radiation using reflection geometry to prevent losses of spectral content within the substrate[74]. After collection and collimation of the beam, the

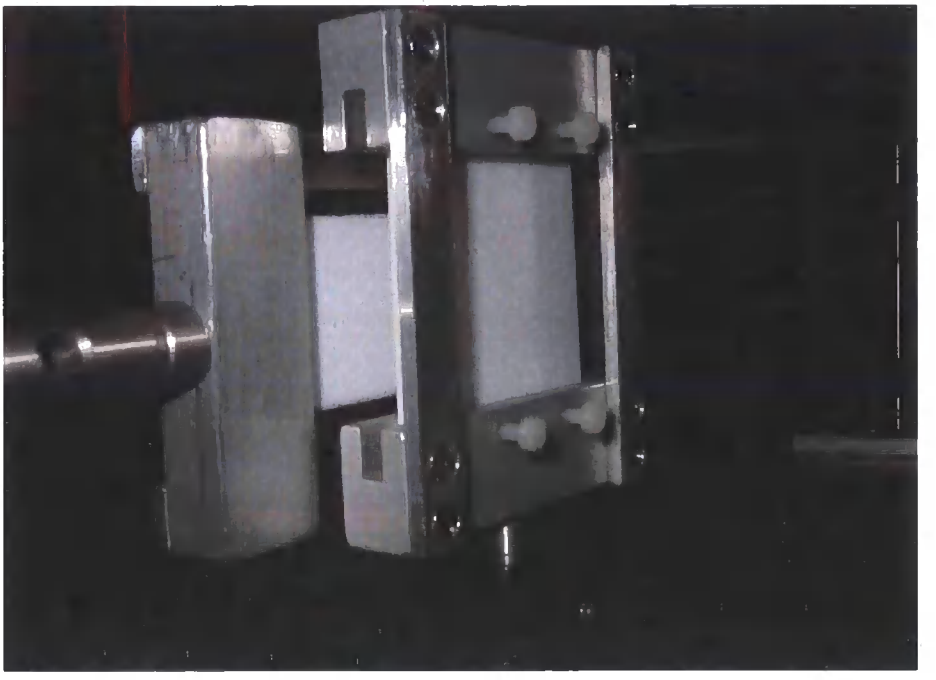

Figure 4.17: Photograph of reflecting mount.

THz pulses were focused onto the reflection point, angled at 27° to the normal, using a 15 cm focal length mirror. The effective spot size of the THz beam at this point was 3 mm. Reflection of the THz radiation took place from either a mirror or the sample of interest. Both of these objects could be inserted into a specially constructed mount, which can be seen photographed in figure 4.17. This mount was designed so that a block containing a reflecting mirror could be interchanged with a slab of the sample. The supporting framework was on the front side of the mount, which meant that a second slab of material could be brought into contact with the back side of the first slab for the determination of gap size resolution.

It should be noted here that the slight discrepancy between the surface of the reflecting mirror and the front surface of the slabs under investigation is not disabling for our measurements. Accurate positioning of the sample's surface with respect to the surface of the mirror, used to obtain the reference measurements, is only required if optical

constants are to be determined from the measurements. Any difference between the relative positions of the sample and reference mirror will introduce an error in the reflectance phase. Since the dielectric function is strongly dependent on this phase, a small error can significantly alter the recorded dielectric constant and hence refractive index of the sample[115]. One such method to overcome this problem has been described by Khazan *et al*, where a convertible transmission-reflection spectrometer is described. In this system, the reflection path length is identical to the transmission path length, so a pulse transmitted through free-space can be used as the reference[116].

After reflection of the radiation - from the mirror, in the case of the reference pulse, or the slabs of interest, for the measurements – the expanding beam was collected and collimated using a further parabolic of focal length 15 cm, before finally being focused onto the detector using a parabolic mirror of focal length 7.5 cm. The photoconductive detector used for these experiments was fabricated on Low Temperature annealed Gallium Arsenide, and consisted of two bow-tie electrodes having a gap of 12 μm by 12 μm. This particular geometry was initially selected for the first set of photoconductive receivers made in an attempt to detect the broadest possible bandwidth with them. Gating of the detector took place using near infrared pulses split from the main pump beam. This probe beam was incident on the receiver, at the point which optimised its impedance, to create an excess of electron-hole pairs. When the THz pulses were also incident on the receiver electrodes, their electric field accelerated the electron-hole pairs, inducing a current across the electrodes, which was measured using a lock-in amplifier. This lock-in amplifier was referenced to the frequency at which the THz beam was being chopped (approximately 1 kHz). By delaying the arrival of the femtosecond laser beam at the emitter, using a delay line, the whole electric field of the THz pulses could be recorded.

Similarly to the transmission system, the whole of the THz optics could be enclosed in a dry box to allow measurements to be made in a purged nitrogen atmosphere if required. This purging removes the effect of water vapour absorption within the laboratory atmosphere.

4.4.2 Optimisation of terahertz reflection spectrometer

Initial testing of the above spectrometer system indicated that there was a considerable amount of electrical noise. This arose from the use of photoconductive receivers. Various methods were tried to resolve this issue, with the eventual solution involving: a new receiver design; minimal laser power on the receiver; and use of a pre-amplifier. The new receiver design was again fabricated on LT-GaAs, but this time the bow tie electrodes were of length 100 μm and width 27 μm, as shown in an inset of figure 4.15. The current induced by the THz radiation was initially pre-amplified, using a commercially available pre-amplification unit (Stanford model 570). This process amplifies the THz pulses, whilst having little effect on the background signal (due to the dark current in the receiver, laser fluctuations etc.) and thus improves the signal to noise ratio of the system as a whole. It was found that the best system performance resulted from placing the detector as near to the pre-amplifier as possible.

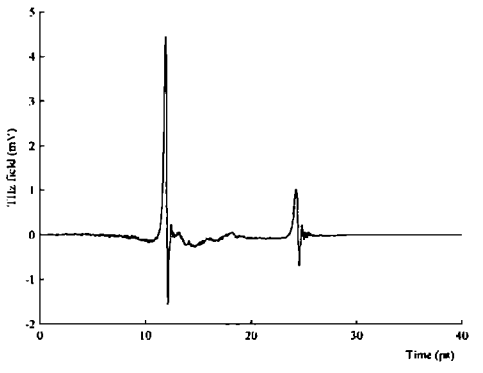

Figure 4.18: Smoothed THz reflected waveform.

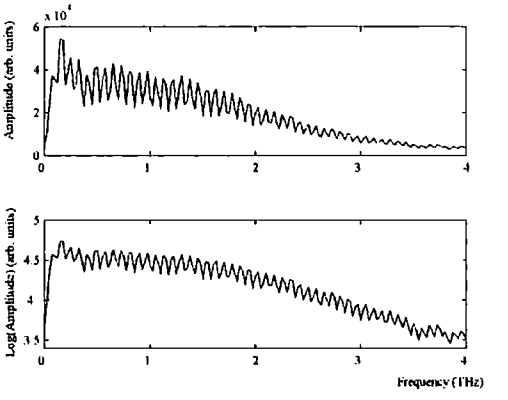

Figure 4.19: Spectral content of pulses generated by the reflection system.

Figure 4.18 shows an optimised THz waveform recorded from this system, whilst figure 4.19 is its associated frequency spectrum. This waveform has been levelled and smoothed using a Gaussian smoothing function. As can be seen, using the modified photoconductive receiver along with pre-amplification of the induced current across it leads to the detection of THz pulses having signal to noise ratio of approximately 1200 and a spectral bandwidth of 3.5 THz. However, the frequency component having maximum power output is rather low in the bandwidth range.

4.4.3 Reflection from sheets of PTFE

The original and reconstructed pulses presented below were obtained from an experiment in which two parallel sheets of PTFE were separated by 1 mm. Figure 4.20 shows the reference reflected pulse (blue) and the pulse reflected from the sample (red).

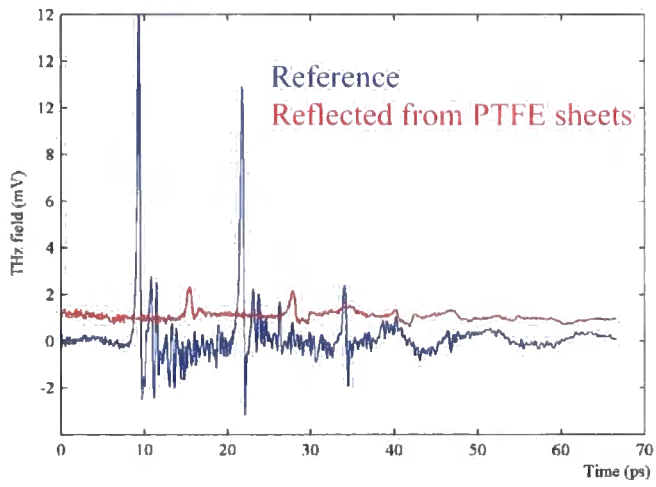

Figure 4.20 Reference reflected THz waveform, with waveform reflected from two sheets of PTFE, separated by 1mm.

These signals have been numerically levelled to remove the very slowly varying non-zero background, which results from using a photoconductive detector. This levelling removes any DC component from the Fourier Transforms. It should be noted that the reflected signal from the sample is much weaker than the reference signal; in fact its amplitude is approximately 15% of the reference amplitude, in good agreement with the Fresnel equations. Similarly to the transmission measurements, both signals are affected by atmospheric water vapour absorption, but to a lesser extent than when electro-optic crystal detection is used, as expected for photoconductive detectors. An enlargement of the reflected waveform from the PTFE sheets is shown in figure 4.21. A number of clearly defined system echoes can be seen in this system as well as some phase reversed pulses. Reflections from the front surface of the PTFE sheet are of the same phase as the reference signal, since the THz pulse is incident on an interface having low to high refractive index change, whilst back surface reflections have a relative phase reversal, since n_1 and n_2 have changed in size.

By careful inspection of the sample reflected waveform, it may be possible to identify the surfaces responsible for these reflected signals. Possible candidates for reflected

signals are shown, indicated by arrows in figure 4.21. The negative half cycle of the first system echo after 29 ps is seen to be split in two, this indicates that a reflected pulse from the sample is concealed at this point, having a delay of slightly more or less than the system echo. Another reflected pulse can also be identified at around 35 ps. However, without prior knowledge of the properties of the sample under test it is not possible to certainly identify the structure.

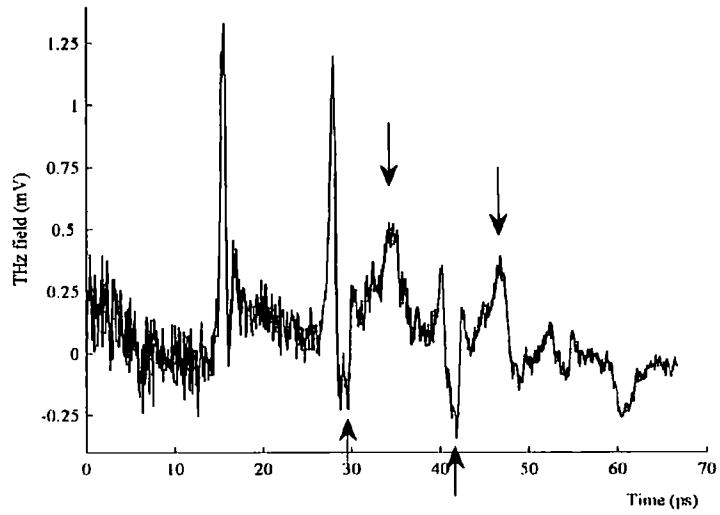

Figure 4.21: THz signal reflected from two sheets of PTFE with 1 mm gap.

The reconstructions of the source and sample signals are shown in figure 4.22, with the blue pulse being the reference reconstruction and the red pulse, that being returned by the sample. For this reconstruction, the parameters used in the signal processing routine are $p = 2$, $q = 0$, $r = 6$; the higher value of r, used here, corresponds to a lower cut-off frequency. Various other combinations of reconstruction parameters were tried, but it was found that applying a numeric high pass filter to the signal processing routine, instead of taking a non-zero q parameter in the reconstruction, resulted in a better removal of the low frequency noise. The black pulse in this figure is a simulation of the response of the PTFE sheets to a pulse, having same shape as the seed (reconstructed source), calculated using the transfer matrix method.

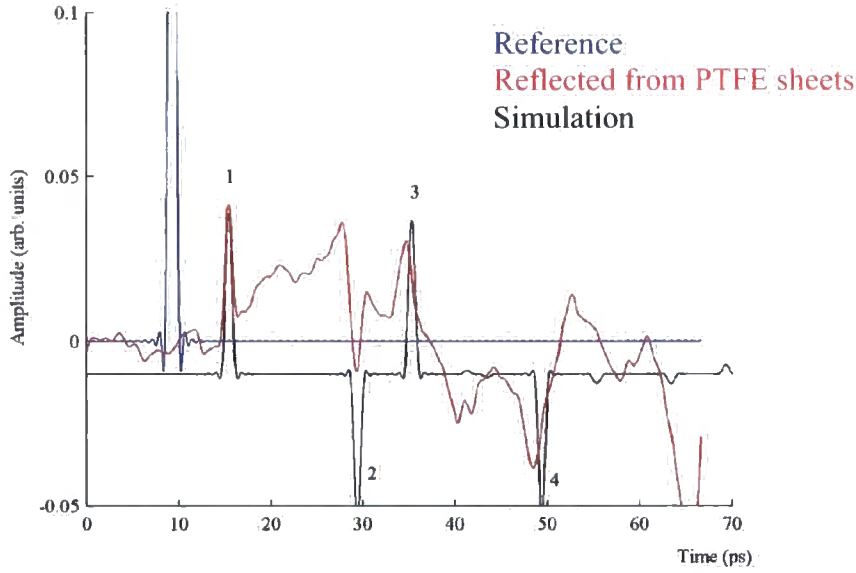

Figure 4.22: Reconstructed pulses for reflection from 2 PTFE sheets with a 1 mm gap.

Once again, application of the reconstruction algorithm has "cleaned" the source and sample pulses of both water vapour absorptions and, especially, the system echoes. Any structure in the sample signal after the first reflected pulse, from its front surface, is due to reflections at slab boundaries and absorption processes within the sample. Peak (1) at 15.4 ps is the reflection from the surface of the first sheet of PTFE: this is delayed from the reference signal because the surface of this is not quite at the same point in space as the reflecting mirror, so a path length increase has been introduced. As explained earlier, this slight difference in path lengths is not disabling for these measurements, since an accurate calculation of the phase is not required. The second phase reversed pulse (2), after 29.4 ps is the reflection from the back surface of the first sheet. Pulse (3) 35.3 ps is the reflection from the front of the second sheet; and pulse (4) 49.4 ps is the reflection from the back surface of the second sheet. The table below lists the times of the expected reflected pulses, those experimentally found using the reconstruction method and their description. Once again, the mismatch in time of the pulse reflected from the back surface of the second slab, which becomes more noticeable as the gap is increased, is due to the experimental beam incident on these interfaces diverging away from its focal point. As a consequence, the reflected pulses at long delays are not collected as efficiently at the detector.

Simulated (ps)	Actual (ps)	Description
15.40	15.40	Pulse reflected from front of sample
29.40	29.33	Reflected pulse from back of first slab
35.33	34.73	Reflection from front of second slab
49.40	48.40	Pulse reflected from back of second slab

Application of the smoothing filter to the reconstructed reflected signal is shown in figure 4.23, with the bars representing the calculated reflection times. When calculating these reflection times the relative optical thickness of each layer needs taking into account, since the THz wave is incident on the interface at a non-zero angle. Formulae for calculating the extra optical path length for a beam travelling through media, having been incident at some non-zero angle can be found in Born and Wolf[117]. In this case, the further filtering only serves to average the base line of the reconstruction to zero, since the source spectrum does not go to zero at the water vapour resonances.

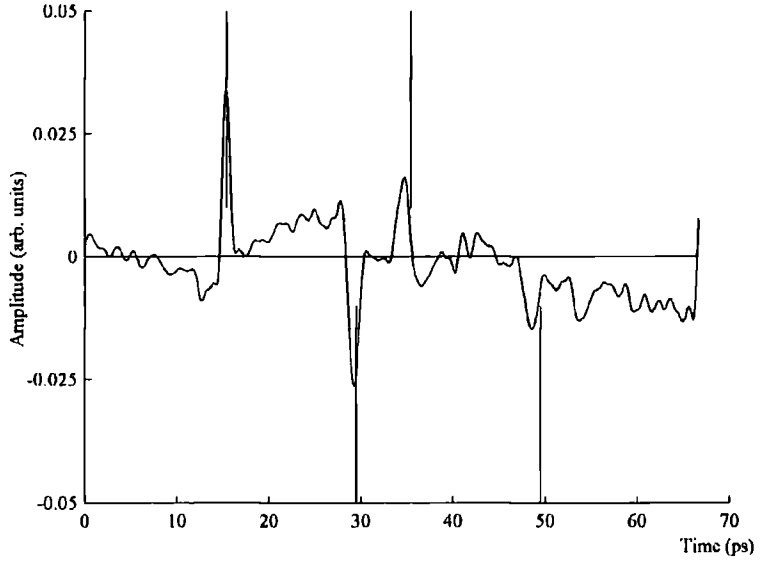

Figure 4.23: Reconstructed signal for reflection from two PTFE sheets with 1 mm gap after further filtering.

The reconstruction method was applied to experimentally obtained reflected pulses from sheets of PTFE having varying gaps and the results are shown in figure 4.24. The circles are the experimentally determined delays, with the lines being the expected delays. In this figure, the two lines parallel to the horizontal are for the delay times for pulses reflected from the front and back surface of the first, stationary slab. The lines whose delay increases with distance are for the reflected pulses from the back, movable

slab. From this data, it is clear that the experimentally determined delays are in very good agreement with the expected delays.

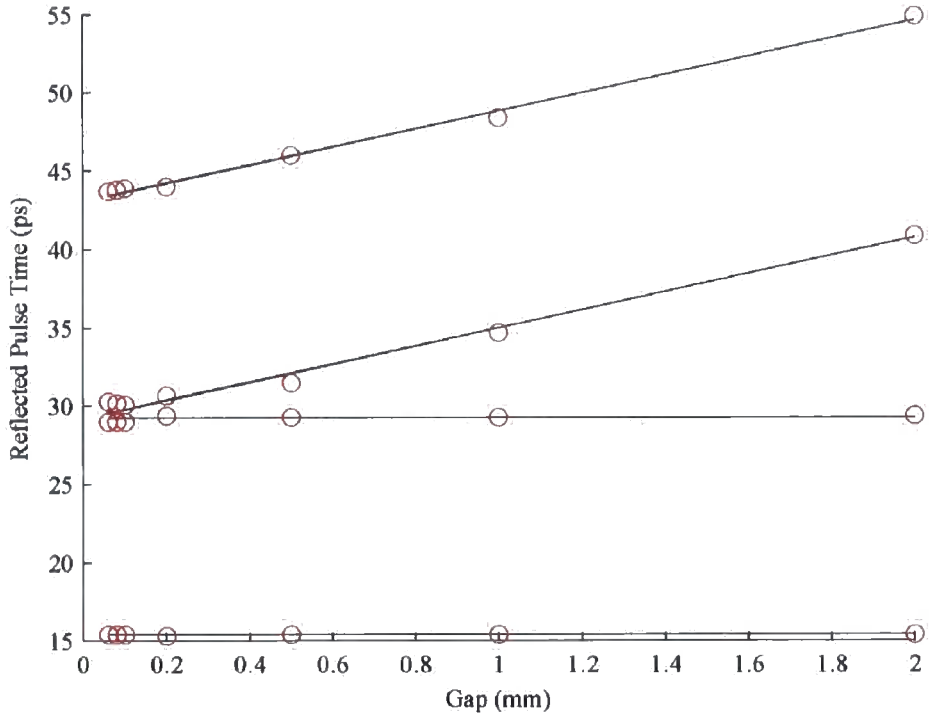

Figure 4.24: Experimentally obtained delays for pulses reflected by two sheets of PTFE with a varying gap between them.

The minimum gap size which can be determined from this data is 100 μm, having used a reconstruction with the parameters $p = 3$, $q = 0$, $r = 7$ Below this gap size, the gap can only be inferred from the reflected pulses from the front surface of the first slab and the back surface of the second slab, using previously obtained knowledge of the thickness of the sheets from the larger gap measurements. For small gaps, the pulses reflected at the gap interfaces become smeared out, meaning that the actual gap is not clearly resolved. This smearing out of the pulses reflected within the gap is due to their finite experimental width: in principle, a shorter THz pulse, thus having larger bandwidth, would be able to determine a smaller gap. The reconstructed signal for pulse reflections from a gap of 40 μm is shown in figures 4.25, with a simulated reflected pulse. This clearly shows that the experimental pulse has become smeared out with respect to the simulated one.

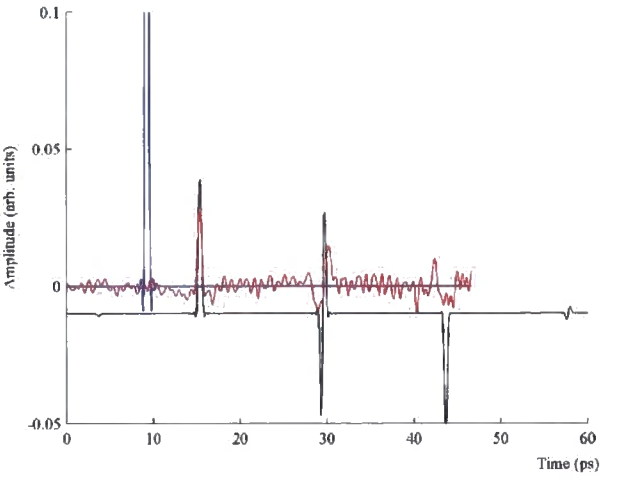

Figure 4.25: Pulses reflected from PTFE sheets, separated by 40 μm.

4.5 Further capability of the pulse reconstruction method.

In a standard terahertz time domain spectroscopy measurement, the time dependences of the THz electric field are recorded before and after interaction with the sample. These are then Fourier Transformed to give the transmission spectrum of the sample, which can be used to identify and characterise a range of substances such as: drugs of abuse[15]; explosives[14]; biological sample[22]; and semiconductors[32]. By calculating the frequency spectra, not all of the information contained within the pulse is used. It has already been explained that the temporal profile of the pulse can be used to identify layers within the sample if it is processed properly, and further to this, the technique of signal processing already described in this chapter can be used to separate the response of a sample to a sharply terminated THz pulse which has been directly transmitted through it.

The electric field produced by a THz TDS system is impulsive and will excite any molecules in the sample, which have vibration frequencies within its bandwidth. After some time period, these molecules will re-emit the radiation at these frequencies. As the incident pulse propagates through the sample it sequentially excites any molecules having resonant frequencies within the source bandwidth with time delays related to the velocity of propagation. Since the phases of the re-emitted radiation are matched to this velocity, the re-emission will combine to give a forward wave. Consequently, the re-emitted radiation is then predominantly aligned to the incident beam, with only a small fraction being radiated in other directions. The technique of time gating can be used to

separate the incident pulse from the re-emitted signals when investigating pulses in the time domain, and allows the properties of this re-emitted radiation to be investigated.

Of course, for this method to work and allow the separation of the incident and emitted signals, the sample must be illuminated by a sharply terminated source pulse. If any part of the source pulse is delayed after the main peak, it will interfere with some of the re-emitted radiation and cause confusion in the interpretation of the signals. Therefore, when samples are being investigated by conventional THz pulsed sources, it is normally not possible to characterise the re-emitted radiation. However, by the application of the signal processing algorithm the response of the sample to a single, simple input pulse is obtained and any structure in the temporal waveform from the sample, after passage of the directly transmitted pulse, is due to these absorptions and emissions. By using time gating on this pulse, the re-emitted radiation can be examined. In the following section these ideas are explored experimentally. However, the interpretation of the results is still open for discussion. This is discussed further in section 4.6.5.

Previous work by Harde and Grishkowsky has looked at delayed emissions of THz vapours[118, 119]. Further work has also been undertaken by Planken and Backker[120]. In both cases the vapours have narrow absorption resonances with long lifetimes and hence their emissions extend over a long time period. Consequently, there is no difficulty distinguishing the incident pulse from the extended emission.

4.6 Experimental observations of re-emitted signals

Observations on re-emitted THz signals were made in transmission, using both the standard time domain setup, previously described in chapter 2 (water and biotin), and an ultra-broadband spectrometer at the University of Leeds, which has the ability to measure THz properties of materials to ~ 7 THz[15], (PTFE). Both PTFE and biotin are solid-state materials which on the whole tend to have broad absorption resonances. As a result, the timescale of emissions is limited to a few picoseconds, which results in overlap with the latter parts of the incident pulse, rendering interpretation difficult.

4.6.1 Water vapour

The response of water vapour molecules in the atmosphere can be investigated using THz techniques by comparing the reconstruction of THz pulses which have propagated through laboratory air of moderate humidity, with a reference signal which has propagated through a purged atmosphere. Figures 4.26 and 4.27 show the THz pulses and reconstructions, obtained using parameters of $p = 1$, $q = 1$, $r = 2$, respectively. The reference signal has been offset in both amplitude and time.

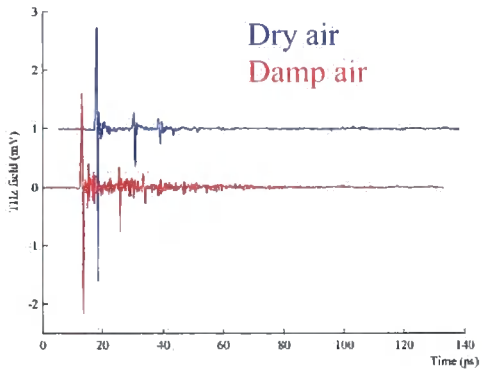

Figure 4.26: THz signals propagating through dry and damp atmospheres.

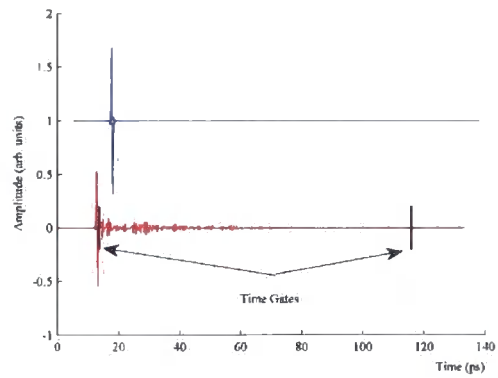

Figure 4.27: Reconstructed signals propagating through dry and damp atmospheres.

After reconstruction, the THz signals show the response of the atmosphere to the simple, single cycle input pulse. The absorption spectrum of the water vapour (figure 4.28) is found in the usual way by division of the unpurged spectra (of the pulse propagating through the damp air) by the purged spectra (of the dry pulse.) Fourier analysis of the section of the reconstructed sample signal following the initial pulse,

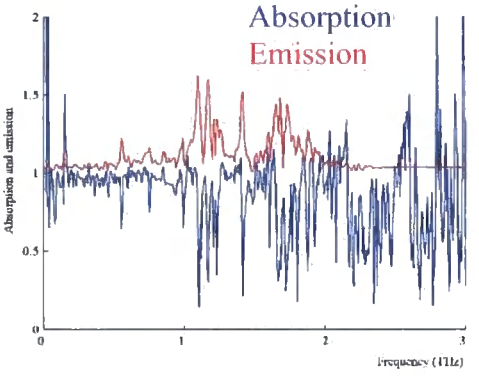

Figure 4.28: Emission and absorption spectra.

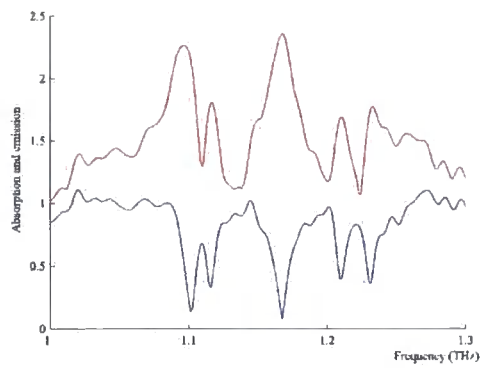

Figure 4.29: Enlarged emission and absorption spectra.

between the two time gates, allows the emission spectrum to be found, which is offset by +1 in this figure. An enlargement of some of the absorption lines of these spectra is

shown in figure 4.29. From this analysis it appears that the emission spectra is simply the reverse of the absorption spectra. The emission lines are too narrow to be resolved completely by the THz system.

4.6.2 PTFE

It is widely known that PTFE is transparent to THz radiation over the broad spectral range of a typical THz spectrometer. However, it is also known that it exhibits a single strong absorption at approximately 6.1 THz with a width of ~ 0.5 THz. Ultrabroadband transmission of THz through a pellet of PTFE, of thickness 0.35 mm, formed by compressing powder of average particle size 100 μm can be used to investigate this absorption. As usual, the ultrabroadband source signal contains echoes, after-runners and oscillations, which also appear in the transmitted signal, with these after-runners and oscillations being stronger. These are shown in figure 4.30 with the sample reconstruction in figure 4.31, calculated using parameters $p = 2$, $q = 0$, $r = 7$. After application of the reconstruction algorithm to remove the source echo from the sample pulse, between 6 and 7 ps, a strongly attenuated pulse is seen at ~ 5.2 ps caused by two reflections within the pellet. Therefore, besides the directly transmitted delay seen in both the recorded and reconstructed sample pulses, the extra delay after two internal reflections is also revealed. It is possible to determine independently both the thickness and the refractive index of the sample using this information. For measured delays of 0.5 ps and 3.7 ps respectively; this gives a refractive index value of 1.45 for a sample thickness of 0.33 mm.

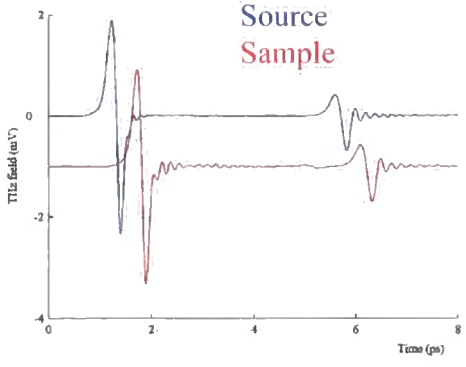

Figure 4.30: Ultrabroadband THz transmission through PTFE pellets.

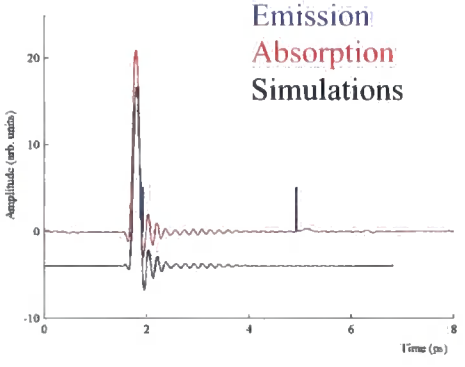

Figure 4.31: Reconstructed sample signal with simulation.

Similarly to the water vapour data, these reconstructed signals can be used to calculate the absorption spectrum of the PTFE. The reconstructed sample signal in figure 4.31

shows that the emission decays rapidly after passage of the simple, single cycle THz pulse, but that this is followed by a slower lasting decay over a time of ~ 3 ps. Once again, the spectrum of the emission can be found by Fourier analysis of the reconstructed signal between time gates placed immediately after the main transmitted pulse, and immediately before the internal sample echo at ~ 5 ps. The emission and absorption spectra are shown below in figure 4.32. It is apparent that this double peaked emission spectrum is not simply the reverse of the single absorption resonance.

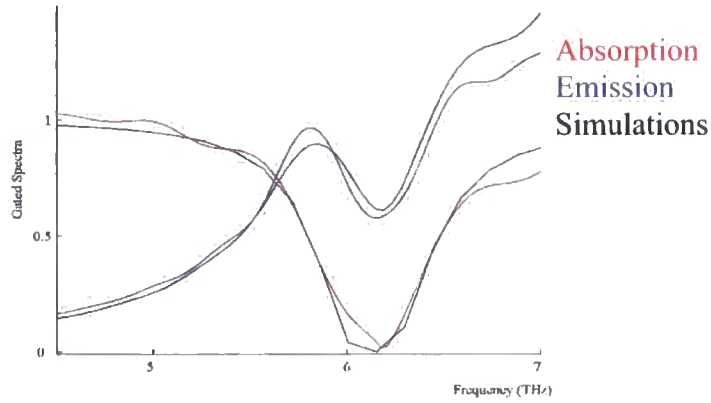

Figure 4.32: Absorption and emission spectra of PTFE.

To gain a better understanding of the response of samples to the passage of a THz pulse through them, simple modelling was undertaken with Dr. John Fletcher. The simulated signals in the above figures are a result of this modelling.

4.6.3 Modelling of pulses passing through solid-state materials

A simple quantum mechanical analysis, considering the time-dependence of the electric dipole of a molecule which has been impulsively excited, indicated that for pulses of THz radiation, which are of insufficient amplitude to perturb the system appreciably from thermal equilibrium, the transitions between the energy levels of the molecules can be treated as independent classical damped harmonic oscillators. A simple model can then be developed to describe the propagation of a wave through a layer of absorbing medium containing resonances within the pulse's bandwidth. If, as in the case of solid state materials, the sample contains a large number of molecules that can be excited by components of the pulse, the re-emitted wave is emitted in a predominantly forward direction. Consequently, a one-dimensional scalar model can be used to model the propagation.

If the material under investigation has a THz refractive index of n, and some of the molecules within it resonate at $\omega_0 / 2\pi$, the simplest way to model the propagation is as a travelling wave, moving with velocity c/n in the medium, coupled to a uniform distribution of harmonic oscillators. A coupling interaction, F, which arises from the energy of interaction of the wave's field with the displacements of the oscillators, is also required.

Using a classical Lagrangian formulation, the dispersion relation for a wave of form $\exp i(kx - \omega t)$ is:

$$\left(\frac{\omega^2}{k^2} - \frac{c^2}{n^2}\right)(\omega^2 - \omega_0^2 + 2i\omega\Gamma) = F. \tag{4.11}$$

Here, Γ is the damping constant which accounts for the linewidth of the resonant absorption that removes energy from the propagating wave. In a sample made from a non-uniform material e.g. pellets of compressed powder, the directly propagating beam will also be scattered by the particles, thus reducing the energy of it. The Phase Distribution Model of chapter three can be used to model this attenuation, and tells us that the mean free path of the scattered radiation can be approximated by the square of the wavelength divided by the effective particle grain size. A modification can be made to equation (4.11) to include these effects and also take into account the fact that most solids have numerous resonances. Thus:

$$\frac{\omega^2}{k^2} = \left(\frac{c}{n + ia\omega/2c}\right)^2 - \sum_j F_j /(\omega_j^2 - \omega^2 - 2i\omega\Gamma_j), \tag{4.12}$$

where a is the effective grain size and j labels the resonances. When the angular frequency, ω, is real valued, equation (4.12) indicates that the wave vector must be complex, corresponding to an attenuated wave.

The final step is to calculate the propagation of a broadband pulse, $E_{in}(t)$ through the system. After propagating a distance, x through an absorbing system, the electric field will become:

$$E_{out}(t) = \int B(\omega) \exp i(xk(\omega) - \omega t) d\omega. \tag{4.13}$$

Here, $B(\omega)$ describes the frequency distribution of the field:

$$B(\omega) = \frac{1}{2\pi} \int E_{in}(t) e^{i\omega t} dt. \qquad (4.14)$$

Numerical modelling of pulse propagation in PTFE: After development of the model it was applied to THz pulse propagation through the PTFE pellets and the results are shown as the simulations in figures 4.31 and 4.32. The model proceeds by propagating a pulse generated using the seed functions, which has the same form as the reconstructed single, simple sample pulse, through the harmonic oscillator that can be described by the parameters $\omega_0/2\pi = 6.15\times10^{12}\,s^{-1}$, $\Gamma = 0.65\times10^{12}\,s^{-1}$, and $F = 5.5\times10^{41}\,m^2s^{-4}$. The central dip in the emission spectrum arises from the strong sample attenuation at the centre of the absorption resonance. Not all of the absorbed radiation is re-emitted at this frequency and hence the re-emitted spectra is split into two.

4.6.4 Biotin

As a further example of the ability of the reconstruction method to investigate the response of molecular samples in the solid state, it was decided to investigate THz transmission through other samples containing absorption bands in the region of a standard spectrometer at room temperature. Biotin, a B vitamin, is an obvious choice for such a system, since it exhibits absorption bands in the required frequency range and biotin is often used as part of model biochemical systems. Pellets of varying mass, and hence thickness, were prepared from powdered biotin (Sigma Aldrich, purity 99%) using a 13 mm diameter pellet press. Korter *et al* have shown that at room temperature, the resonances in the THz range are broadened by the superposition of several transitions with similar frequencies[121].

In the original data, figure 4.33, numerous system echoes are seen in the very detailed pulse which has been transmitted through the sample pellet of 0.46 mm thickness. These oscillations are due to the absorptions and re-emissions taking place within the pellet. By comparing this transmission with the free-space THz pulses, the refractive index of a pellet can be found, shown in figure 4.34 for a pellet of thickness 0.62 mm. The black curve is a simulated refractive index obtained using the model of pulse propagation outlined above, and pulse and sample parameters described below. Biotin

is found to have a refractive index of 1.7 ± 0.1, by averaging the index obtained for a wide variety of sample thicknesses.

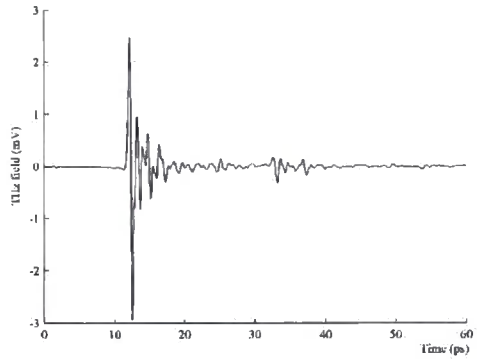

Figure 4.33: THz pulse transmitted through 0.46 mm thick biotin pellet.

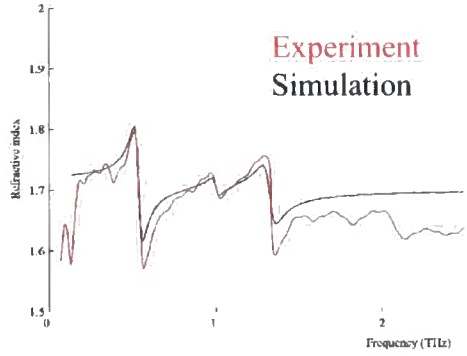

Figure 4.34: Refractive index of biotin, calculated from 0.62 mm thick pellet.

Figure 4.35 shows the reconstructed source pulse (blue) and pulse transmitted through a 0.62 mm thick biotin pellet (red), along with a simulation (black). The reconstruction parameters are: $p = 2$, $q = 1$, $r = 3$, and it is an input pulse of this shape which has been put through the model. The reconstructed signal shows that after passage of the single cycle input through the sample, numerous fast oscillations are emitted that decay over a period of approximately 10 ps. Calculation of the absorption spectra by Fourier Transform are shown in figure 4.36 for pellets of thickness 0.46 mm and 1.62 mm. These spectra reveal the absorption frequencies, in good agreement with the literature, and also show that biotin absorbs THz radiation quite strongly above a frequency of approximately 1 THz.

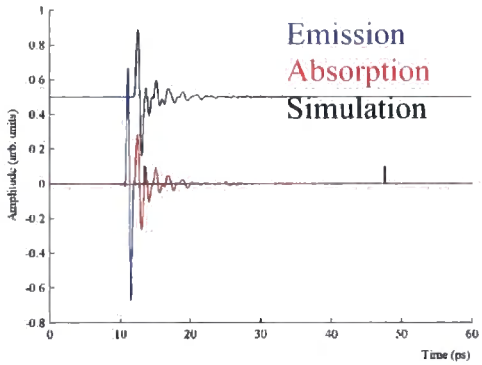

Figure 4.35: Reconstructed signals.

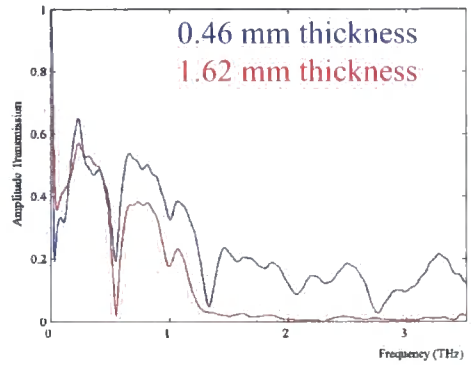

Figure 4.36: Absorption spectra.

The spectrum of the emissions in figures 4.37 and 4.38 are found by Fourier analysis of the part of the transmitted signal between the time gates. From both of these results it is clear that the emission is once again simply not the inverse of the absorption. The

decreased emission seen at 1 THz is due to destructive interference from the emissions on either side. Absorption within the biotin is increased by random scattering within the tablets from particles with effective size 120 μm.

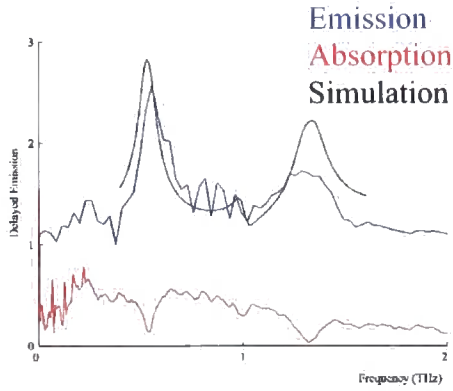

Figure 4.37: Emission and absorption spectra of a 0.46 mm thick pellet.

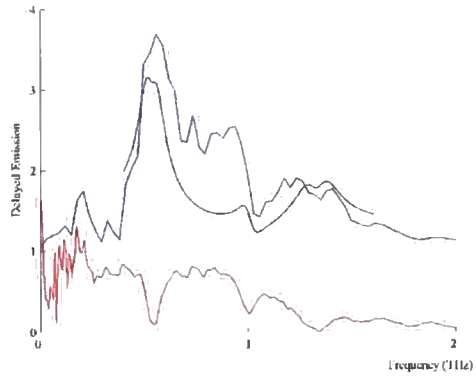

Figure 4.38: Emission and absorption spectra of a 0.90 mm thick pellet.

The modelled results shown above were carried out using equations (4.12), (4.13) and (4.14). An incident pulse (of the same form as that used to produce the reconstructed seed pulse) interacted with a set of harmonic oscillators having the following parameter values, $\omega_0/2\pi = [0.54 \quad 1 \quad 1.33]\times10^{12}\,\mathrm{s}^{-1}$, $\Gamma = [0.15 \quad 0.15 \quad 0.25]\times10^{12}\,\mathrm{s}^{-1}$, and $F = [0.7 \quad 0.21 \quad 1.5]\times10^{40}\,\mathrm{m}^2\mathrm{s}^{-4}$. These parameters were obtained from the transmission spectrum of the sample, with one set being used to model each of the three major resonances. Here the broadened lines of biotin's resonances within the THz range can be modelled as the result of a decay, with a relaxation time Γ^{-1}, chosen appropriately for the combined width.

4.6.5. Other possible reasons for the appearance of emission

It should be noted from the above results that the emission and absorption spectra often add up to one, which indicates that the phenomena of the interaction of short pulses with solid state samples is not fully understood. A sum of one for the absorption and emission indicates that all the THz radiation absorbed at a particular frequency by the sample is re-emitted at the same frequency. Absorptions by a sample in the THz range tale place over a narrow band of frequencies, and by the uncertainty principle will thus be broad in the time domain. This makes accurate time gating of the reconstructed sample pulse difficult. Consequently, interpretation of time gated temporal pulses is

still open to debate and further work needs to be undertaken to clarify the physical phenomena being observed.

4.7 Summary and conclusions

The work presented in this chapter of the thesis has been concerned with the application of signal processing techniques to the temporal form of a THz pulse. Signal processing of THz pulses is highly desirable because THz pulses generated via broadband spectrometers never have a trivial form. They always contain system echoes and after-runners due to absorptions and re-emissions from both the system and within the sample. As a result of the application of a newly developed signal processing algorithm to THz pulses, which involves convolving the source and sample signals with a seed function, the response of a sample to a simple input pulse can be measured. This input has bandwidth within the source, but it does not contain the disabling echoes and after-runners. The result of the processing method is to deliver the impulse response of the device or sample under test and "cleans up" signals so that small, but genuine, effects caused by the interaction of the THz pulse with the sample can be observed.

The method is validated by experimental transmission and reflection studies of simple "phantom" structures which mimic the behaviour of a void or "impurity" located within another object. It is also used to show the response of a sample to a simple incident pulse form and may form a technique to allow the separation of delayed emissions from within the sample from the part of the pulse directly transmitted through it. The application of signal processing methods has been shown to significantly increase the ability of broadband THz techniques to image voids within samples. These might include laminated composites or contraband concealed within sealed documents.

Experiments in transmission and reflection geometries with suitable phantoms show that significant signal to noise improvements are possible and that signals less than 2% in amplitude of the main pulse can be easily measured. Using the method, a resolution of less than 500 μm in transmission and 100 μm in reflection is readily obtainable. The use of the signal reconstruction method allows the separation of delayed emission signals from the sample from the effects of the delayed parts of the pulsed THz incident field. Experimental measurements on water vapour, biotin and solid PTFE, have been undertaken in an attempt validate this method. Successful simulation of these results

has been undertaken using a simple mathematical model for propagation in the presence of resonant molecules. It has tentatively been found that the emission spectrum is not simply the reverse of the absorption spectrum. However, further work needs undertaking to: clarify the origin of the physical processes which produce the observed signal; and to check that the technique of time gating is not removing information about specific, narrow spectral lines.

One specific and useful conclusion of the work is that purging of THz TDS systems, to reduce atmospheric water absorption, may not be necessary if signal processing methods are used. A more general conclusion that can be drawn from the work as a whole is that much more information, which is currently hidden, could be obtained if further attention were paid to THz signal processing methods.

Further improvements to this technique would be seen if narrower pulses were incident on the samples of interest. This would allow the detection of smaller voids, for example. It would also be useful to undertake further, more detailed modelling to determine the origins of absorptions within the solids. In addition, if the resolution of the system can be increased, it may be possible to further resolve the resonances. This is possible in a discrete spectrometer by increasing the scan length, with the drawbacks of an increase in data acquisition time.

5. Design and construction of a terahertz scattering setup

Scattering of THz radiation from targets of interest has previously been studied by several authors. For example, work undertaken by Mittleman *et al* has investigated the propagation of single-cycle pulses of THz radiation in random, scattering media[92], whilst Chau *et al* have investigated THz pulse propagation in strongly scattering media[104]. However, all these experiments have attempted to characterise multiply scattered radiation using transmission measurements: scattering induced dispersive effects have been observed through different path lengths of scatterers[92] and when the scatterer size or dielectric properties are changed in the sample[103].

To undertake measurements which actually record the terahertz radiation field scattered by a sample at various angles requires the construction of a totally new type of THz-TDS system. Numerous terahertz spectroscopy systems have been built that have the capability of measuring pulses of terahertz radiation which have been scattered by a 'target' sample. Mittleman *et al* constructed a scattering terahertz spectrometer to measure the electric field of a multiply scattered wave, but only at 90° to the incident beam[101]. Other work, for example that by Zhang's group, has measured the optical properties of three-dimensional structures in tomography-type experiments[122]. These measurements all used what is known as "fixed detector, rotating sample" setup. Here a terahertz beam is incident on a sample, which can be rotated about an axis, and detection takes place at a fixed non-zero angle.

We have investigated radiation scattered from a fixed sample at a number of angles. Measurements like this allow conventional tomography to be undertaken: a full description of such schemes, algorithms and terahertz tomography experiments will be given in chapter six. Here, we concentrate on describing how a novel time domain scattering terahertz spectrometer was built. Within the available literature, there are very few reports of systems which work in such a way. Previous measurements of scattering events by Mittleman *et al* involved the collection of radiation scattered at various angles by a sample cell containing Teflon spheres, and used correlation functions to characterise individual scattering events, although no real experimental details are reported[101, 123].

To measure radiation scattered from a fixed sample at numerous angles requires a totally different system design approach. The radiation must be either: focused onto the sample at the centre of rotation of the detector, with detection taking place a short distance behind; or more usually, focused onto the detector after interacting with the sample, which itself is placed at the centre of rotation. This second alternative geometry is shown in figure 5.1 in the next section. Inevitably, this geometry rather constrains the design of the terahertz detector. It must first be realised that a movable detector requires the terahertz radiation and near infrared gating beams to be incident on the opposite sides of the detector, see figure 5.1. By implication, this means that photoconductive sampling techniques must be used. A further constraint is that the terahertz radiation must propagate through the substrate GaAs layer before being detected via the current it induces across the electrodes fabricated on the low temperature annealed layer.

Two options exist for steering the gating beam to the detector over a wide range of angles: a periscope system or optical fibres. Both of these approaches have their individual merits and drawbacks and these will be discussed in turn. If a periscope system is used to gate the receiver, all of the laser beams are kept in free space avoiding the effect of pulse dispersion in a non-linear medium. This means that shorter optical pulses can be used, and thus the possibility of increased bandwidth is available. However, after rotation of the receiver, it will "switch off," since unless the periscope is perfectly aligned, rotation will cause the laser beam to move a short distance over the receiver electrodes, which are separated by a gap of just a few microns. In consequence, slight movement of the laser beam around the periscope will cause the focused laser spot to move off the receiver. Use of optical fibres, on the other hand, ensures that the receiver is always correctly illuminated by the optical pulse because the fibre output coupling and detector becomes a fixed unit. The drawback with this method is the initial difficulty of coupling a laser pulse into a fibre and the effects of pulse propagation within a non-linear medium. Here, the pulse actually changes shape (disperses) and grows in length during propagation through the fibre.

A decision was made to proceed with the building of a fibre-fed detection system since this offered the possibility of the most stable detection unit, albeit at the expense of bandwidth loss. Such systems, using optical fibres to steer the near infrared gating

beams to either the emitter or detector (or both) are available commercially from TeraView in the UK and Picometrix in the USA. Within the literature though, very few reports of fibre-coupled technology exist. Crooker built a fibre coupled system for undertaking THz spectroscopy at low temperatures and within high magnetic fields[124], whilst Van Rudd and Mittleman used optical fibres to gate their emitters and detectors whilst investigating THz emission patterns from lens-coupled antennas[125, 126].

Initially, a fibre-fed emitter and detector pair was obtained from TeraView, Cambridge as part of the EU TeraNova project to use with the femtosecond oscillator, readily available at Durham, which was described in chapter two and used for the experiments in chapters three and four. However, it quickly became apparent that the pulses output from this Coherent Mira oscillator were just too short, and hence contained too large a spectral bandwidth, for them to be of any use after propagating along optical fibres.

The second approach tried involved the loan of an Integral 50 laser from Femtolasers, Austria. As part of the TeraNova project this company has been developing a femtosecond laser with two output ports, one freespace and one fibre-based. Pulse lengths of 100 fs are guaranteed at the end of fibre. Using this laser meant that a home-made receiver would be used, gated with the output from the fibre in freespace, whilst the freespace output would be used to generate the THz radiation with a conventional LT-GaAs switch. The general experimental setup to be used was very similar to that described in section 5.1 below. After building this setup the laser, which was only a prototype of the design Femtolasers hope to market, became irreparably damaged.

Thus, the third option came into play: a (different) femtosecond Coherent Mira source loaned from Rutherford Appleton Laboratories was used. This loan laser, produced much longer pulses (of the order of 80 fs) than Durham's own Mira, which delivered pulses of approx 25 fs in length. Use of this loan laser meant that the whole setup needed building from scratch, including the coupling of the infrared beam into an optical fibre, with the associated problems of pulse compression. The general experimental principles used for this are the same as those for the Femotlasers laser, in that generation of the terahertz used purely freespace techniques, whilst the detection utilized an optical fibre to steer the near infrared pulse to the detection unit, consisting of a photoconductive switch, illuminated in free space.

Five main sections now follow in this chapter. Firstly, the design and construction of a terahertz scattering radiation spectrometer, with fibre-coupled detection, is described. Since the detection part of the experimental system requires propagation of near infrared pulses through optical fibres, acting as waveguides, a description is given of how short pulses propagate through a medium having non unity refractive index. This propagation within an optical medium causes the pulse shape and length to change. In fact, the pulse time lengthens, but techniques exist to overcome this and methods of pulse compression are described. The next section deals with techniques for measuring optical pulses, but is mainly concerned with a description of the experimental pulse lengths obtained after their propagation along a single mode fibre and how optimisation of the pulses takes place. Finally in this chapter, THz pulse profiles obtained using a fibre-fed setup, and their corresponding frequency spectra, are discussed before ways of optimising the system as a whole are detailed.

5.1 Construction of a terahertz scattering system

The construction outlined here describes building a terahertz scattering setup, using the loaned laser from Rutherford Appleton Laboratories as the source of near infrared pulses. This laser delivers pulses of average length 75 fs, assuming a Gaussian profile, average power of 1 W and centre wavelength of 800 nm. As is usually the case in terahertz spectroscopy experiments, the output from the laser was split in two using a beam splitter, with 70% propagating through free space to generate the THz radiation using a photoconductive switch, and the other 30% being used for detection. For THz detection, a photoconductive switch, of geometry identical to that described in chapter four was used; this was excited using the near infrared probe pulse that had propagated along a 3 m length of single mode optical fibre. In both cases, the photoconductive switches are fabricated on Low-Temperature grown Gallium Arsenide. Use of the fibre ensured that the probe laser beam was always focused to the correct point on the photoconductive receiver, having a gap of area 2500 μm^2. This receiver has the same geometry as that described in section 4.4.2. Figure 5.1 shows that the terahertz and near infrared beams were incident on the opposite sides of the photoconductive detector, which was free to rotate from -90° to +140° degrees about the sample, marked in blue.

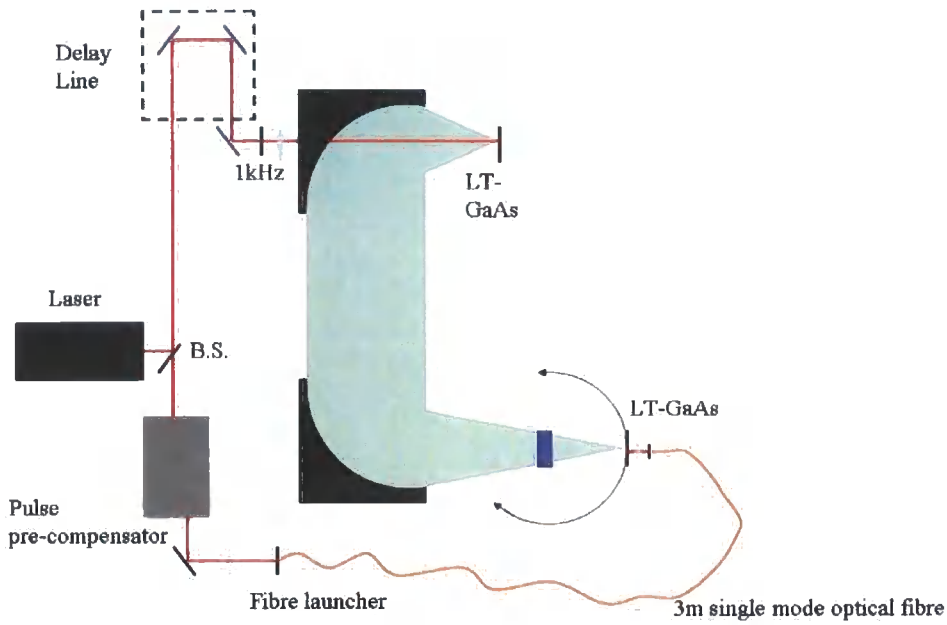

Figure 5.1: Schematic of terahertz scattering setup.

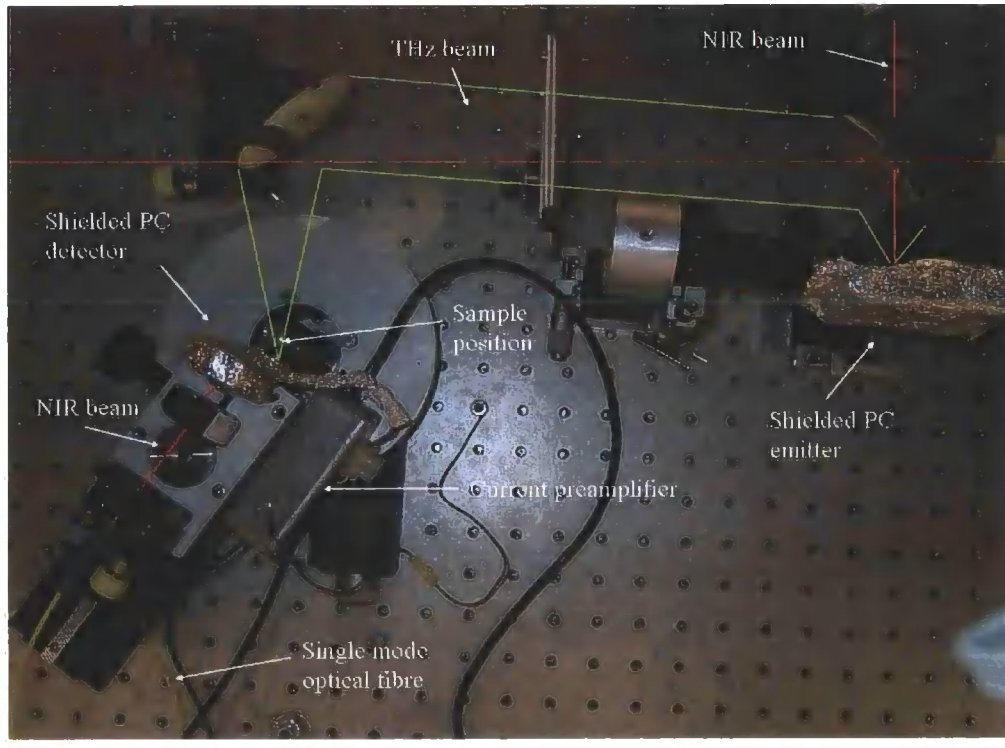

Figure 5.2: Picture of terahertz scattering setup.

In this scheme, the detector is at 0°, and positive angles are defined as being in the clockwise direction. Figure 5.2 is a picture of the part of the setup where the THz

radiation is both generated and detected, showing the relative positions of the optical and terahertz beams, with the detector at an angle of +30°.

5.1.1 Building a fibre-fed terahertz receiver

Fibre-fed THz detection schemes are currently very much in their infancy, with only a handful of reports of this technology in the literature. The major problem when sending short, intense light pulses along a length of optical fibre is that they change shape and lengthen during propagation. This is because the intensity of the pulse causes the manifestation of non-linear effects within the fibre leading to both group velocity dispersion (GVD) and self-phase modulation (SPM). These effects and ways to compensate for them are discussed in the next two sections of the chapter. Using the fibre however does have the advantage that a stable detection unit, that remains optimised, can be built and rotated about the target of interest.

Immediately after splitting the output beam from the laser, the detection beam underwent group velocity dispersion, using a Coherent technologies mini-GDC (group velocity dispersion compensator). This compensator uses four bounces off one grating to provide the dispersion compensation usually obtained by the use of a single pair of gratings and a retro-reflecting mirror. The principles behind compensation and compression are discussed in section 5.3. Figure 5.3 shows a picture of the inside of this device, with the path of the laser beam added in red. On exiting this device, a mirror pair and lens were used to steer the laser beam into the fibre launcher, from whence the optical pulse propagated along single mode optical fibre. The fibre launch coupling can also be seen in the bottom left of the picture. The fibre launcher consists of a hemispherical lens in a mount, which ensures that as much of the near infrared radiation as possible is coupled into the core of the optical fibre. Another lens is attached to the end of the fibre to ensure that the optical beam exiting it is also collimated. Measurement of the pulse power before and after the optical fibre allowed the overall coupling efficiency to be determined. A maximum value of 45% was found, but the more usual operating efficiency was of the order of 38%. The major reason for this relatively low efficiency is to do with the size of the fibre: the internal core is a few microns in diameter, and it is impossible to focus the external laser beam waist down to this size, even with the assistance of the collecting lens.

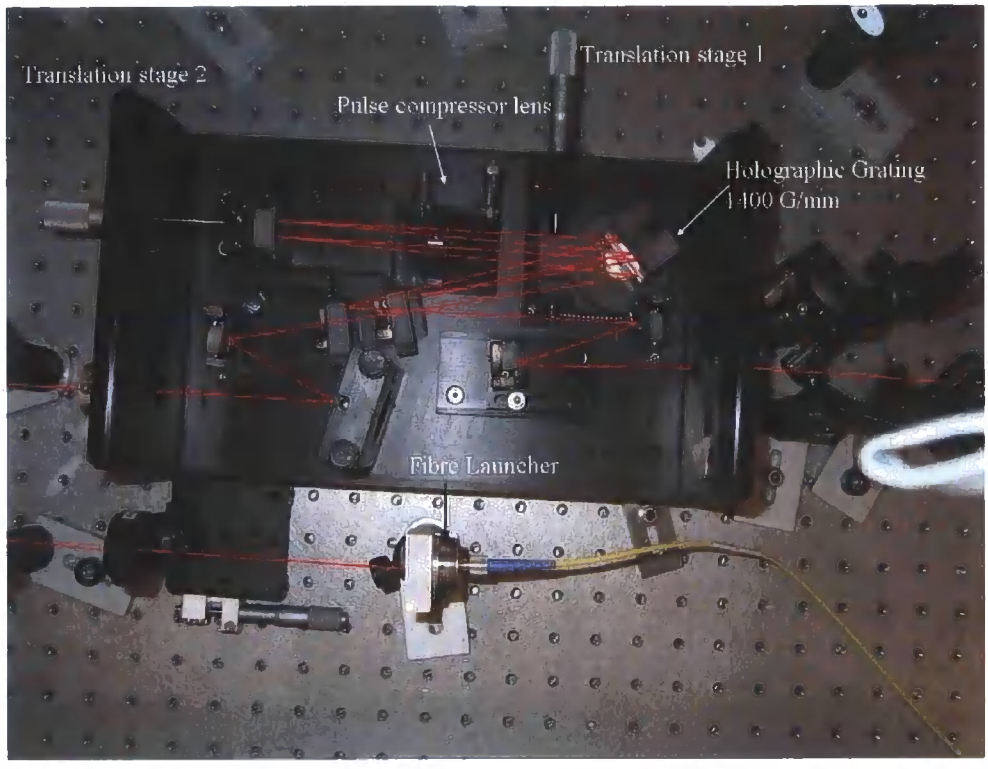

Figure 5.3: Internal layout of mini-GVD compensator.

The detection unit consisted of three major components, all mounted solidly on a base plate, which could be attached to a rotation stage. A standard optical mirror mount, having the usual degrees of manoeuvrability, was securely attached to one end of the base plate, with the fibre output coupler inserted. At the other end of the base plate, the photoconductive receiver, mounted on veroboard, was solidly attached in a lens mount. Finally, a lens, having focal length of 2 cm, was inserted between the fibre output and receiver. This could be moved longitudinally so that the tightest possible focus could be obtained on the receiver. This detection unit can clearly be seen in the bottom left of figure 5.2. Having constructed this detection unit, the photoconductive receiver was optimised, in other words its resistance (or impedance) was minimised by steering the optical beam, using the capability of the mirror mount containing the fibre output, to the correct point on the receiver.

5.1.2 Generation of terahertz radiation

After the detection unit had been constructed, the optical beam used for generating the terahertz radiation was steered to the emitter, through a hole in the first, collecting parabolic mirror. THz radiation from the emitter was collected in reflection geometry, using a parabolic mirror of focal length 5 cm, which collimated the radiation onto a

second parabolic mirror. This mirror, of focal length 15 cm, focused the THz radiation onto the backside of the GaAs substrate of the photoconductive detector. Figure 5.1 shows the schematic of this. The current induced in the receiver was then measured using a lock-in, referenced to a 1 kHz mechanical chopper inserted in the optical beam of the generation arm.

Working in reflection geometry enabled higher bandwidth components to be collected from the emitter, in the hope that the highest bandwidths possible would interact with the sample of interest and thus the broadest possible spectrum detected[74]. Since the detected terahertz first had to propagate through the GaAs substrate, the perceived bandwidth of the pulse is automatically lowered due to absorptions within the substrate. The main problem at this stage of the construction arose from matching the two optical path lengths for coherent sampling to take place. Precompensation of the optical pulse, using the mini-GVD, results in an optical path length of 1.7 m even before the propagation through the 3 m optical fibre and the freespace distances (between: laser and GVD; GVD and fibre; and fibre and receiver) are taken into account. The fibre was initially assumed to have a refractive index of 1.5: the optical fibre is constructed from Silica, which has a refractive index of 1.5 at 800 nm. Thus, the combined generating optical beam path and terahertz path had to be 7.3 m long. To obtain this length of optical path for the generating beam, multiple bounces of the near infrared beam up and down the optical bench were used. This pump path was set so that the overlap in length of the two beams occurred when the delay line translation stage was approximately in the middle of its length. Scanning the stage to find the overlap of the two beams led to the determination that the fibre's refractive index was actually very close to 1.5. A lens pair was also inserted into the generating optical beam path to prevent the beam waist from growing too much along its 6.7 m propagation length. The remaining half metre or so of pump path being transversed by terahertz as opposed to near infrared radiation.

5.2 Theory of pulse propagation

It will be recalled from chapter two that any optical pulse propagating through a medium undergoes distortion due to group velocity dispersion. This causes the pulse to become longer in time and gain a positive chirp, with red frequencies leading the blue ones. Pulse propagation in transparent media is also affected by various non-linear effects, the most important of which is self-phase modulation that can generate extra

frequencies in the pulse envelope. A combination of these effects can be used to compress optical pulses. These are now discussed in more detail.

5.2.1 Dispersion of optical pulses in a transparent medium

We first consider how light propagates in a transparent medium and, in particular, consider the case of a Gaussian pulse. Recall from chapter two that a pulse can be described by a plane wave multiplied by a Gaussian function, so has electric field:

$$E = \mathrm{Re}\left(E_0 e^{(-\Gamma t^2 + i\omega_0 t)}\right) \tag{5.1}$$

Here Γ is the shape factor. The instantaneous frequency is simply the time derivative of the phase, so $\omega = \partial\varphi/\partial t = \omega_0$, since the phase of the pulse varies linearly with time. Thus the instantaneous frequency is constant and is equal to the central angular frequency. If, on the other hand, the phase took the form of a quadratic dependence, $\varphi = i(\omega_0 t + at^2)$, the instantaneous frequency is no longer constant in time. In fact it varies linearly with time, and the pulse becomes what is known as "chirped." For example, if the constant $a > 0$, then $\omega(t) = \omega_0 + 2at$ and the pulse is more red (low frequency) at earlier times and more blue (high frequency) later in time.

The Gaussian pulse described by equation 5.1 has Fourier Transform:

$$E_0(\omega) = \exp\left[\frac{-(\omega-\omega_0)^2}{4\Gamma}\right]. \tag{5.2}$$

After propagating a distance x, the spectrum of the Gaussian pulse is modified to:

$$E(\omega, x) = E_0(\omega)\exp[-ik(\omega)x], \tag{5.3}$$

with $k(\omega) = n\omega/x$ being the frequency-dependent propagation factor. If a Taylor expansion is made of this propagation factor, the pulse spectrum can be re-written in terms of the first two derivatives as:

$$E(\omega, x) = \exp\left[-ik(\omega_0)x - ik'x(\omega-\omega_0) - \left(\frac{1}{4\Gamma} + \frac{i}{2}k''x\right)(\omega-\omega_0)^2\right]. \tag{5.4}$$

Applying an inverse Fourier Transform gives the time evolution of the electric field:

$$\varepsilon(t, x) = \sqrt{\frac{\Gamma(x)}{\pi}}\exp\left[i\omega_0\left(t - \frac{x}{v_{ph}(\omega_0)}\right)\right]\exp\left[-\Gamma(x)\left(t - \frac{x}{v_g(\omega_0)}\right)^2\right], \tag{5.5}$$

where:

$$v_{ph}(\omega_0)=\left(\frac{\omega}{k}\right)_{\omega_0}, \qquad v_g(\omega_0)=\left(\frac{d\omega}{dk}\right)_{\omega_0}, \qquad \frac{1}{\Gamma(x)}=\frac{1}{\Gamma}+2i\frac{d^2k}{dx^2}x. \tag{5.6}$$

The first term of equation 5.5 indicates that the phase is delayed by an amount of x/v_{ph}, but this is not observable. The second term shows that the pulse retains its Gaussian profile after propagating a distance x, but it is delayed by x/v_g.

Using expressions for the frequency dependent wave number, expressed in terms of the refractive index $k(\omega)=n(\omega)\omega/c$, the phase and group velocities can be written as:

$$v_{ph}=\frac{c}{n(\omega)}, \qquad v_g \sim v_{ph}\left(1-\frac{\omega}{n(\omega)}\frac{dn(\omega)}{d\omega}\right). \tag{5.7}$$

The form factor of the Gaussian part of the pulse in equation (5.5) is now dependent upon both x, the propagation distance, and the frequency through k''. Alternatively this can be written:

$$k''=\left(\frac{d^2k}{d\omega^2}\right)_{\omega_0}=\frac{d}{d\omega}\left(\frac{1}{v_g(\omega)}\right)_{\omega_0}, \tag{5.8}$$

which is known as the 'group velocity dispersion.' The form factor can also be written as:

$$\Gamma(x)=\frac{\Gamma}{1+\xi^2x^2}-i\frac{\Gamma\xi x}{1+\xi^2x^2}, \tag{5.9}$$

where $\xi=2\Gamma k''$, which on substitution into equation (5.5), allows the second part of the pulse to be written as:

$$\exp\left[-\frac{\Gamma}{1+\xi^2x^2}\left(t-\frac{x}{v_g}\right)^2+i\frac{\Gamma\xi x}{1+\xi^2x^2}\left(t-\frac{x}{v_g}\right)^2\right]. \tag{5.10}$$

This is now in the general form of a Gaussian pulse in the time domain:

$$E \sim \exp(-\Gamma t^2+i\Phi(t)). \tag{5.11}$$

Examination of the real part of equation (5.10) shows that the pulse is still a delayed Gaussian, but with a form factor of $\Gamma/(1+\xi^2x^2)$. This is always less than the form factor of the pulse before it entered the transparent medium. The imaginary part of equation (5.11) (the phase) contains a term with quadratic dependence, the condition required to create a linear frequency chirp to the pulse[59].

5.2.2 Self-phase modulation

This arises because of third order non-linear effects that originate when a short pulse propagates through a medium. Within a material the non-linear refractive index depends upon the intensity of the light passing through it. In the case of an optical pulse, the intensity varies with time, so the non-linear index can be expressed as:

$$n = n_0 + \tfrac{1}{2} n_2 I(t), \qquad I(t) = e^{-\Gamma t^2}. \tag{5.12}$$

For a plane wave propagating in a non-linear medium:

$$E(t,x) = E_0 e^{i(\omega_0 t - kx)}, \tag{5.13}$$

where $k = \frac{\omega_o}{c} n(t)$. The instantaneous frequency is the time derivative of the phase:

$$\omega(t) = \frac{\partial}{\partial t}\Phi(t) = \omega_0 - \frac{\omega_0}{c}\frac{\partial n(t)}{\partial t} x, \tag{5.14}$$

which varies as:

$$\delta\omega(t) = \omega(t) - \omega_0 = \frac{\omega_0}{c}\frac{n_2}{2}\frac{\partial I(t)}{\partial t} x. \tag{5.15}$$

From the Fourier duality between time and frequency, application of a periodic amplitude or phase modulation to a periodic signal creates new frequencies. Even though they are not synchronised, the new frequencies remain within the original pulse envelope. As an example, if n_2 is positive, red frequencies are created in the leading edge of the pulse and blue frequencies in the tale of the pulse[59]. The new frequencies produced via this method lead to a spectral broadening of the pulse envelope. Thus, if the correct group velocity dispersion can be added to suitably spectrally broaden this pulse envelope, the possibility exists for pulse compression to take place.

5.3 Pulse compression

Third order effects arising from the propagation of short pulses in a non-linear medium produce a spectral broadening within the pulse envelope by the process of self-phase modulation. However, SPM does not on its own reduce the duration of the pulse because after propagating through a non-linear medium, the pulse is no longer transform limited. If the pulse is to be compressed, the red wavelengths must be slowed down with respect to the blue ones, and this can be achieved using group velocity dispersion. The simplest way to do this is to use a diffraction grating which acts as a

dispersive delay. Individual wavelengths contained in a pulse envelope are diffracted through different angles by the grating and consequently the path length between two gratings is different for the various wavelength components of the pulse. Since the optical path is longer for the longer wavelengths, a negative group velocity dispersion can be induced on the pulse, which compensates for the positive chirp of the self-modulation.

5.3.1 Time compression by a pair of gratings

A pair of diffraction gratings is the simplest way to correct for group velocity dispersion[127]. This technique has been around since the late 1960's and uses the fact that a light pulse, incident at a non-zero angle on a grating, will be split into the various spectral components contained within it. By the law of diffraction, the various wavelengths will be diffracted by differing angles, and the path length between the two gratings will vary for the different components. The components that have been diffracted more must therefore traverse a greater distance and are thus delayed with respect to the lesser diffracted wavelengths. Further, if the two gratings can be set so that their wavelength dispersions are reversed, the second grating will recollimate the beam having introduced a spatial chirp on it.

Figure 5.4 shows a schematic of a pair of gratings (R_1 and R_2) having groove spacing d,

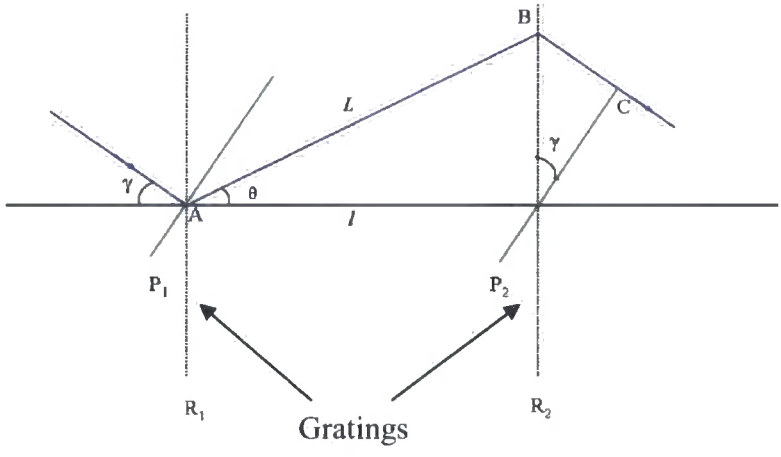

Figure 5.4: Optical path between a pair of diffraction gratings.

separated by distance l, with a ray of light of wavelength λ incident at angle γ on the first grating[128]. This is scattered through an angle θ, which is wavelength dependent.

Recall from equation (5.8) the group velocity dispersion, k'', which can instead be written in terms of wavelength, λ and group delay, t_g introduced over some propagation length, x, where $t_g = x/v_g$:

$$k'' = -\frac{\lambda^2}{2\pi c} D, \tag{5.16}$$

where $D = \frac{1}{x}\frac{dt_g}{d\lambda}$. In the above case, the group delay is simply the travel time along the path ABC. This is the distance the light beam must travel whilst the plane wave P_1 propagates through the system, exiting as plane wave P_2, thus:

$$t_g = \frac{L}{c}(1 + \sin\gamma \sin\theta), \tag{5.17}$$

where $L = l/\cos\theta$, the distance the beam travels between the two gratings. The variation of group delay with wavelength is thus:

$$\frac{dt}{d\lambda} = \frac{(1 + \sin\gamma\sin\theta)}{c}\frac{\partial L}{\partial\lambda} + \frac{L}{c}\sin\gamma\cos\theta\frac{\partial\theta}{\partial\lambda}. \tag{5.18}$$

Using the equations for a diffraction grating, $\lambda = d(\sin\gamma + \sin\theta)$ and L, the group delay variation is therefore:

$$\frac{dt}{d\lambda} = \frac{(1 + \sin\gamma\sin\theta)}{c}\sec^2\theta\tan\theta\frac{l}{d} + \frac{L}{c}\sin\gamma\cos\theta\frac{\sec\theta}{d}. \tag{5.19}$$

After further manipulation, using standard trigonometric identities, and substituting for l in terms of L, this can be written as:

$$\frac{dt}{d\lambda} = \frac{L}{cd}[\sec\theta\tan\theta + \sin\gamma(1 + \tan^2\theta)] = \frac{L}{cd}\frac{(\sin\theta + \sin\gamma)}{\cos^2\theta}. \tag{5.20}$$

Thus, substituting into equation (5.16), and taking $x = L$, the distance the beam travels between the gratings, the group velocity dispersion is:

$$k'' = -\frac{\lambda^2}{2\pi c^2 d}\frac{(\lambda/d)}{1 - \left[\frac{\lambda}{d} - \sin\gamma\right]^2}. \tag{5.21}$$

Therefore, by correctly selecting the parameters of the diffraction grating, a system can be built which provides either positive or negative group velocity dispersion. In other words, it is possible to build a device to compensate for the positive dispersion introduced when a pulse propagates through a medium and thus re-phase it. Compression using a pair of gratings before the waveguide (optical fibre) can only completely compensate second order non-linear effects: small cubic phase dispersions from pulse propagation in a non-linear medium cannot be exactly cancelled[124].

5.3.2. Pulse compression of ultrashort pulses

It should first be recalled from earlier in this chapter that as an optical pulse propagates through a medium, its high intensity causes the manifestation of non-linear effects. Consequently, the pulse undergoes: group velocity dispersion, which leads to a spectral dephasing of the pulse without affecting its spectral amplitude; and self-phase modulation, which causes a temporal dephasing to the pulse, but similarly it does not alter the temporal profile. The SPM creates new frequencies within the pulse: redder components at the leading edge and blue ones at the trailing edge. This broader spectrum does not in itself imply that the pulse has become shorter: recall that it is only transform limited pulses that occupy a minimum possible time, or conversely consider a light bulb, which shows that a broad spectral bandwidth does not necessarily imply the existence of short pulses. However, the existence of a broader spectrum of frequencies does allow one to reduce the duration of the pulse, but only if the correct dispersion can be added to the pulse to rephase it. Generally, the red frequencies must be slowed with respect to the blue ones, which means that a negative chirp needs putting on the pulse. It should also be noted that the technique of GVD can be used to rephase a chirped pulse, but it can never reduce its duration below that defined by the Fourier relation. As such, the correct application of GVD and SPM can be used to reduce the duration of an optical pulse.

When using SPM to broaden the frequency content of a pulse, a medium must be used which gives a uniform broadening across the pulse spectrum over the whole beam width. Therefore a non-linear waveguide must be used and single mode fibre works very well in this case. If such a medium were not used, the spectrum would broaden far

more at the centre of the beam, where it is most intense. After passing along the

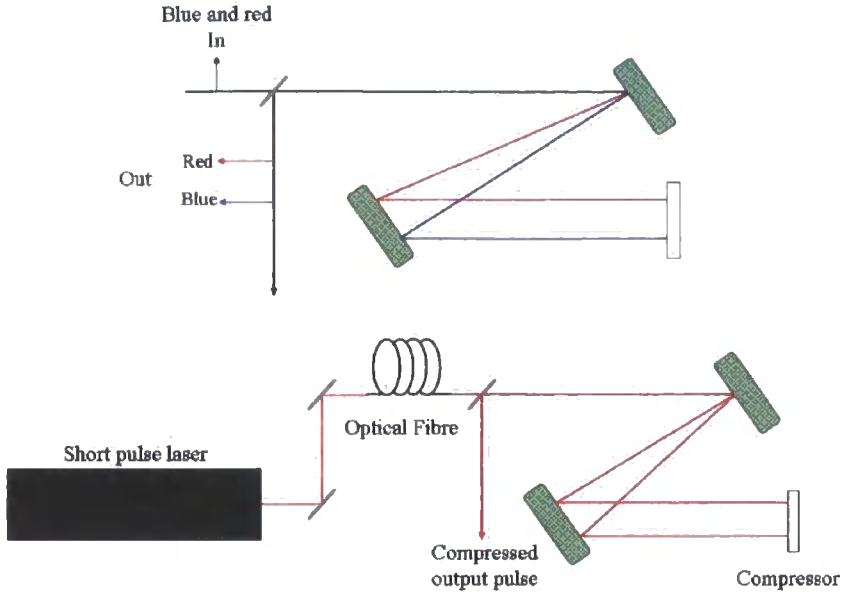

Figure 5.5: Schematic of a pair of diffraction gratings and how they are used as part of an optical compression experiment, with some non-linear waveguide.

waveguide, which has broadened the spectrum and introduced a positive chirp to the pulse, the optical pulse must then have a negative chirp induced upon it, slowing the longer wavelengths more that the shorter ones, to cancel the positive dispersion and thus rephase the pulse[129]. A grating pair provides the ability to do this, which as outlined in section 5.3.1 has a longer path length through it for the redder wavelengths. The first grating spatially disperses the different wavelengths whilst the second recollimates the beam, as shown in the upper part of figure 5.5. Further, if the beam is then retro- reflected back into the grating at a different height, the spatial chirp introduced by the first pass is cancelled, whilst the dispersion on the pulse is doubled. The lower part of figure 5.5 is a schematic of the laser, optical fibre and grating pair. Note that the pulse can only undergo maximum compression if the different wavelengths are brought back together, which corresponds to the minimum chirp. In fact, the order of the phase modulation and velocity dispersion does not actually matter, and it is more convenient to first apply a negative chirp to the pulse, before it undergoes phase modulation in the fibre in THz experiments. Thus, if a transform-limited pulse first passes through a group velocity delay it becomes negatively chirped, before being rephased as it propagates through the optical fibre.

As optical pulses become shorter, it becomes more difficult to compress them using the above technique. The technique instead becomes a tool to prevent ultrashort pulses from growing too much on propagating through a dispersive medium. The limitation arises with the GVD component: as more and more group velocity dispersion is required, so the size of the diffraction grating must grow, both in terms of the optical path length between the two gratings and consequently the actual size of the gratings themselves. However, the combination of GVD and SPM can be used to ensure that the femtosecond pulses retain their approximate Gaussian shape and do not grow in length by too much on passing through an optical fibre. After undergoing GVD with a grating pair, followed by SPM in a fibre, ultrashort pulses exiting the fibre may no longer be transform limited. Instead, the pulse envelope will contain a broader spectrum of frequencies, with some degree of positive chirp.

5.4 Measuring pulse widths after propagation through single mode optical fibre

The simplest way to measure optical pulses is by the method of autocorrelation. This technique was used to characterise the pulses exiting the optical fibre after initially undergoing group velocity dispersion. By tuning the distance between the diffraction gratings in the mini-GDC, using translation stage 2 as shown in figure 5.3, the minimum output pulse was measured.

5.4.1 Optical autocorrelation

It is widely known that optical methods provide the best way to measure the temporal profile of pulses: electronic methods are limited by the response times of photodiodes[130]. The method of auto-correlation is derived from the mathematical technique of correlation functions: consider two time-dependent functions $F(t)$ and $F'(t)$; if one is known, say $F'(t)$, then measurement of the first order correlation function, $G(\tau)$, defined as

$$G(\tau) = \int_{-\infty}^{\infty} F'(t)F(t-\tau)dt, \tag{5.22}$$

gives the other. Since femtosecond pulses are extremely short, the pulse itself must be used as its own test function, hence the name autocorrelation.

In a general auto-correlation measurement the laser pulse is split into two replicas using a beam splitter. These propagate through an interferometric setup, which means that the pulse paths are of different lengths. This path length difference introduces the required delay (light travels 300 μm in 1 ps for example) with the instantaneous electromagnetic field playing the part of the function $F(t)$. The simplest way to characterise the pulse is then to make a second order autocorrelation measurement, using a two photon process. Here, one pulse propagates along a fixed delay, with the other pulse transversing a variable delay. The pulses are recombined on a photodetector, after passing through a suitably filtered phase matched frequency doubling crystal. The harmonic field recorded corresponds to the second order correlation function[131].

5.4.2 Experimental measurement of pulse widths

After alignment of the mini-GDC, shown in figure 5.3, the laser pulse was launched into the optical fibre and the fibre coupling optimised. The fibre output was fed into an autocorrelator and the pulse width measured using an oscilloscope. Assuming that the pulses exiting the fibre had a Gaussian shape, their length could be calculated using the relation:

$$\text{Time (femtoseconds)} = \Delta t \times 32 \text{ fs/μs} \times 0.707 \qquad (5.23)$$

where Δt is the full width half maximum (FWHM) pulse time on the oscilloscope. Movement of translation stage #2 altered the distance between the grating pairs and allowed the pulse chirp to be set correctly to cancel, as much as possible, the positive chirp and hence the dispersion introduced by the fibre. Initially, pulses of average power 65 mW were launched into the fibre, exiting with a power of 24.5 mW. After optimisation of the compensation, the shortest pulses were found to exit the fibre with an autocorrelation FWHM of 20 μs, as measured directly from the oscilloscope in real time. This corresponds to a pulse width of 450 fs. i.e. the pulses had actually grown by a factor of approximately six from the 75 fs input. Using an Ocean Optics spectrometer to measure their spectra, the pulses exiting the fibre were observed to still be of a good, mode-locked profile shape. Figure 5.6 shows the variation in pulse length as translation stage #2, which alters the physical separation of the gratings, is optimised.

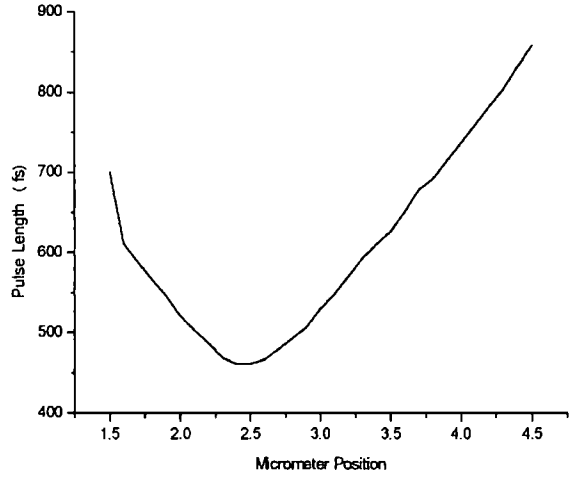

Figure 5.6: Pulse duration at end of fibre, as the distance between the gratings is changed.

Ultrashort pulses are already widely available for the generation and detection of the THz radiation and so pulse compression is not actually required. Instead, the aim here is to prevent growth of the pulse temporal envelope as it propagates along the single mode optical fibre. Within the fibre, pulse dispersion and spectral broadening are

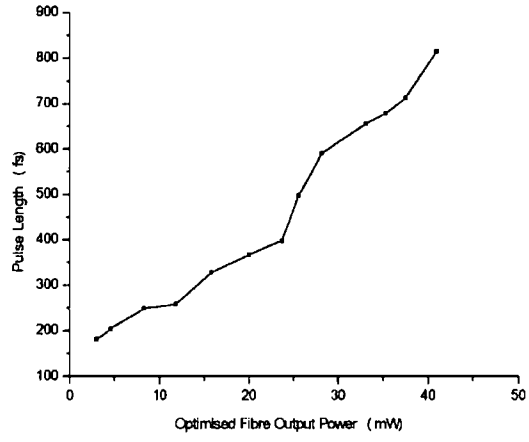

Figure 5.7: Pulse length variation with fibre output power.

caused by third order non-linear effects in the dispersive medium, both of which are dependent upon pulse intensity. Thus, these effects can actually be reduced if the initial pulse intensity launched into the optical fibre can be lowered. Reduction of the fibre input power is possible by filtering the optical power travelling through the mini-GDC using an appropriate neutral density filter placed before it. Figure 5.7 is a plot of the variation of pulse length output from the fibre with average power at the end of the

fibre. These results were obtained by decreasing the input power in steps of approximately 10 mW from 120 mW to 10 mW, and are for maximum fibre input coupling efficiency. In other words, the average output power was optimised for each given incident level. The maximum coupling efficiency is obtainable if the input power is in the range of 60 to 15 mW: outside this range the maximum possible efficiency is lower.

The minimum output power required at the end of the optical fibre, to detect THz radiation using a photoconductive receiver, is approximately 5 mW. Using the knowledge of the coupling capability of the fibre, shown in figure 5.8, if pulses with average input power in the region of 15 to 20 mW are launched into the fibre, the exit power is high enough to generate carriers in the photoconductive detector switch.

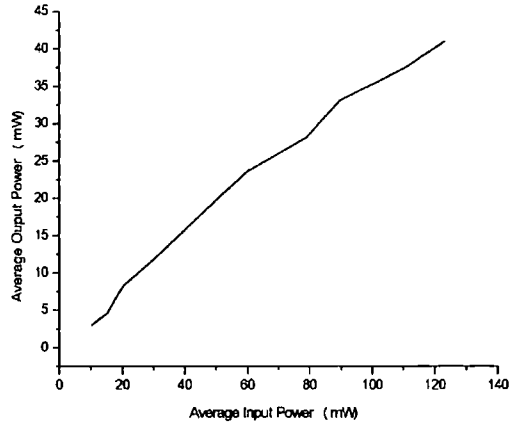

Figure 5.8: Optimised exit pulse power with input.

Numerous autocorrelation traces were then saved to the oscilloscope for average output powers of 5, 7.5 and 10 mW. Figure 5.9 shows the average of all of these autocorrelation traces for each output power. Reading the FWHM times from the graph shows that for an average output power of 5mW, the autocorrelation width is 6.0 μs, corresponding to a pulse length of 136 fs. The corresponding results for 7.5 and 10 mW are 7.4 and 8.4 μs leading to pulse lengths of 167 and 190 fs respectively. These pulse lengths are short enough to measure the expected spectral bandwidth of the system. Measurement of the pulse power before and after the fibre to check the coupling efficiency and output power should give a good estimate of the pulse length exiting the fibre. This is the way in which the pulse length was checked each time the system was used.

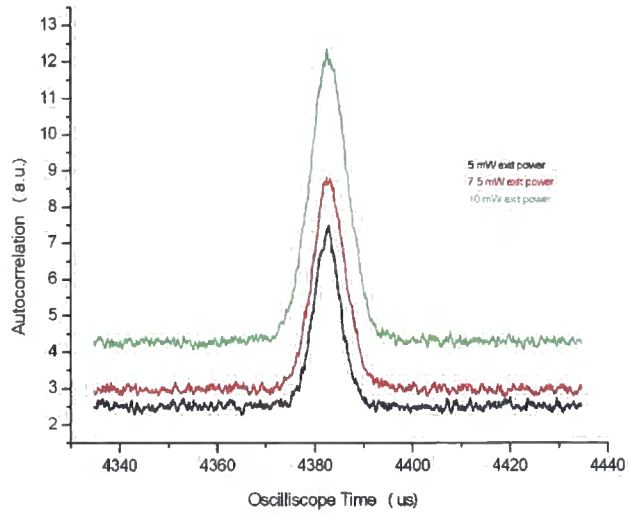

Figure 5.9: Average autocorrelation traces for 5, 7.5 and 10 mW exit powers respectively.

5.5 Measurement of terahertz pulses from this system

After optimisation of the optical pulse length exiting the single mode fibre and alignment of the rest of the terahertz system, THz pulses from it were measured as described in section 5.1.2. Initially, the current from the photoconductive receiver was measured using the lock-in and an optimised (levelled) pulse and its spectra are shown in figures 5.10 and 5.11 respectively.

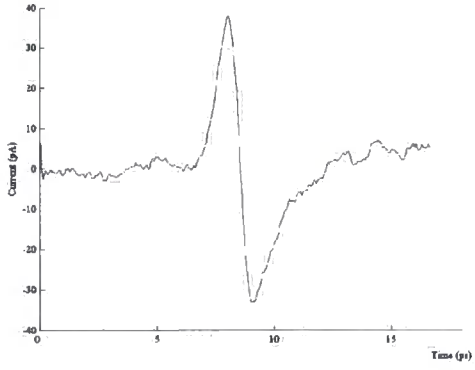

Figure 5.10: THz pulse from fibre-fed spectrometer.

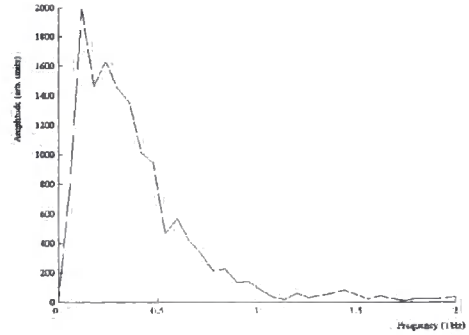

Figure 5.11: THz spectrum from fibre-fed spectrometer.

As can be seen, the pulse contains spectral components extending to about 1 THz. To improve the performance of the system it was decided to initially pre-amplify the current from the detector using a Stanford low noise current preamplifier unit placed between the switch and the lock in, as in the reflection measurements of chapter 4. This was found to improve the performance of the system somewhat, but there were still

issues with variable background noise in particular. This mainly arises because the actual current generated in the switch is tiny, of the order of a few picoamps. Also, quite a long BNC cable (of the order of half a metre) is required to connect the detector and pre-amplifier together, if the detection unit is able to move over the full range of angles. If this cable vibrates, its weight can cause slight movement of the detector board: recalling that the photoconductive gap being excited by the laser pulse is small, slight movement of the chip can cause the laser spot position to vary in the gap, changing the properties of the switch.

The final approach tried was to use a pre-amplification unit built in-house. This very simple circuit is shown below in figure 5.12. The left hand circuit schematic shows the amplification unit, whilst the right hand is the mains power supply rectifying unit to power it. Use of this circuit much improved the stability of the detection unit. As it was much smaller than a commercially available amplifier, it was possible to place it much closer to the photoconductive detector switch. In consequence, there was less chance of interference with the picoamp current before it was amplified to a voltage of a few tens of microvolts and input into the lock-in. Whilst designing the circuit, the major issue was what the size of the feedback capacitor should be, labelled C5 in the schematic.

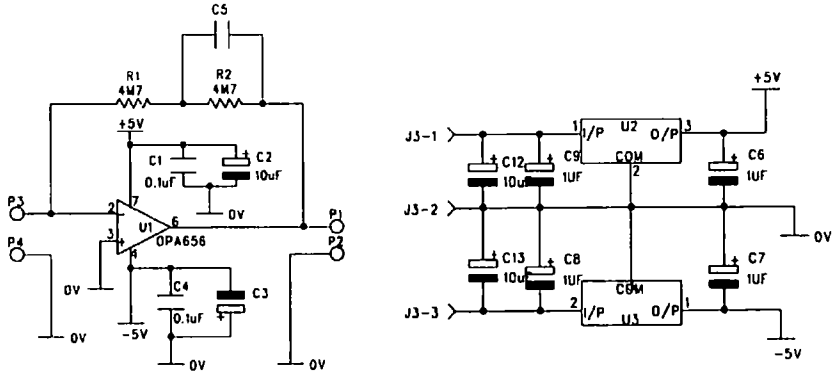

Figure 5.12: In-house built amplification and mains rectifying circuits.

Large capacitors have the advantage of reducing electrical noise at the expense of reducing peak power. Figure 5.13 shows pulses for both 22 nF and 100 pF capacitors, using both battery power and a rectified mains supply, with figure 5.14 being their

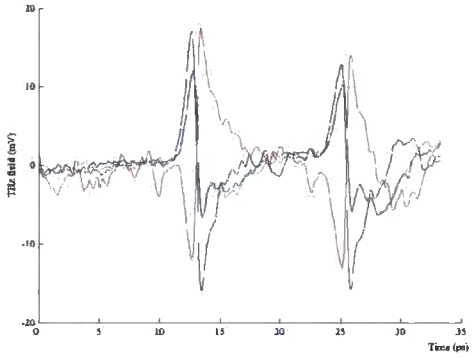

Figure 5.13: THz pulses from amplification circuit.

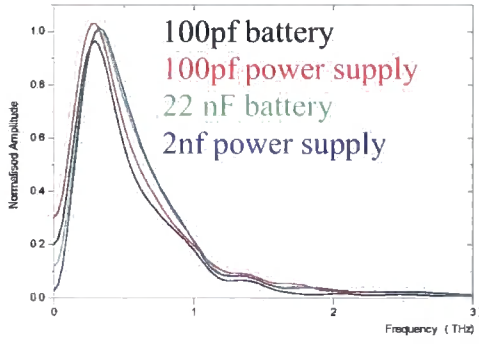

Figure 5.14: THz spectra from amplification circuit.

filtered, normalised spectra. It can clearly be seen that the larger value capacitor reduces the electrical noise in the time domain, but the detected amplified voltage is less. The 100 pF capacitor provides a higher peak to peak voltage, but is both more noisy (in the time domain) and has a lower normalised spectral bandwidth. Unfortunately, it did not prove possible to use a capacitor having intermediate value between the two shown: the two available values of capacitance in that region produced excessive noise in the scans, due to some (unknown) high Q type factor in the circuit when the detector was attached and illuminated. Since both capacitors had similar performance when the circuit was either powered by batteries (to overcome the effect of 'non-common' earths) or powered using a rectified mains supply, the circuit could be powered from the mains electricity supply, thus removing the chance of losing data due to battery failure during a scan.

It was decided to proceed with this amplification circuit using a 22nF capacitor. The circuit was mounted onto the rotation stage, and wired via short lengths of cable to the detector. The circuit was housed in a shielded metal box to remove effects of electrical interference as much as possible. Pulses containing frequency components up to 2 THz, and with signal to noise ratio of a few hundred, could be detected using this arrangement. A fully optimised pulse and its respective frequency spectra are shown in figures 5.15 and 5.16 respectively. It should be noted that there is a lack of power in the

spectra around 1.1 THz. The origin of this is unknown, but is likely to be due to absorptions in the substrate.

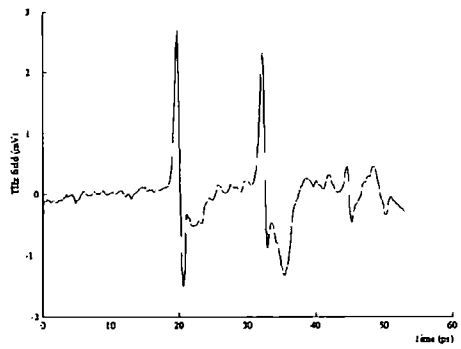

Figure 5.15: Optimised THz pulse using homebuilt amplifier.

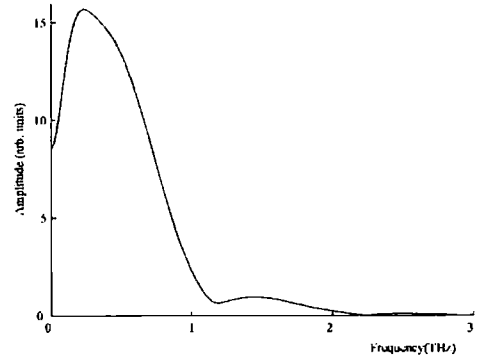

Figure 5.16: Optimised THz spectrum using homebuilt amplifier.

Finally, it should be mentioned here that a silicon hemispherical lens could have been attached to the back surface of the detector, where the THz radiation is incident to improve the collection efficiency. The lens' function is to collect as many frequency components as possible from the generated pulse and direct them all to one place at the actual detector electrodes, since the focal spot size of the various frequency components contained within a THz pulse are different. The lower frequency components focus to a larger spot size, and it is these which are of the greatest intensity. Whilst this may seem like a good idea, in practice it is not particularly helpful in this situation, since when scattered radiation is being detected off-axis, the lens will collect different frequency components which have been scattered over a range of various angles, reducing the angular resolution of the system. This is especially pertinent to work on for example meta-materials,[132, 133] in which the THz beam must be confined within the light guiding structure. Consequently, the sample must be placed at the focus of the radiation, which is set to be the centre of rotation of the detection arm, with the detector moved back, away from the focal point, into the re-expanding THz beam. Thus, the lens will only serve to confuse the issue of determining the beam steering direction of the meta-material structure, collecting, at one angle, various frequency components which have actually been scattered through different angles.

5.6 Summary and conclusions

This chapter of the thesis has been concerned with the design and development of a terahertz spectroscopy system that has the ability to measure the angular profile of

scattered pulses from a target. Such a system must use a photoconductive switch for the detector, so that the terahertz radiation and near infrared gating beams can be incident on opposite sides of the unit. Thus, either an optical periscope or an optical fibre must be used to steer the gating beam to the receiver and their relative merits and drawbacks have already been outlined. In this work, an optical fibre was used as the steering mechanism since this allows a stable detection unit to be built. However, this does have the associated problems with the propagation of ultrashort pulses in a non-linear medium, which leads to pulse dispersion and broadening. If this dispersion can be overcome by correct negative chirping of the pulse before it enters the fibre, there is no reason why this form of detection cannot be used to detect THz bandwidths useful for most "everyday" applications.

Using the experimental arrangement described in this chapter, it was possible to detect components having frequencies up to 2 THz contained within a terahertz pulse. This spectral bandwidth is the equal of that obtained by many other groups, using the same detector geometry. At this point, it seems pertinent to make a few remarks about the suitability of this system for making measurements with possible suggestions for its improvement.

This work has revealed that fibre-fed detection does provide a suitable method for detecting scattered THz radiation within the limited bandwidth that such a system provides. The results of the scattering experiments are presented in the next chapter. Use of an optical fibre to steer the optical gating beam to the detector means that a stable detection unit can be made, which is always optimised, no matter where it is moved to. However, the bandwidth of this system is limited since the THz radiation must necessarily be incident on the back surface of the detection chip and thus propagate through the GaAs substrate. Consequently, some of the radiation is absorbed and the higher frequency, but lower power, components emitted by the THz source are not detected. Improvement in the performance of this receiver can be seen if the current detected by the photoconductor is pre-amplified, with the best performance being seen when the amplification takes place as soon as possible after the chip.

The author suggests that further improvements can be made to this system by actually incorporating the detector chip onto the printed-circuit-board (PCB) containing the

amplification circuit. PCB has a much higher impedance than veroboard, which the receiver is currently mounted on, and incorporation of the detector onto the circuit board would ensure that it is very close to the amplifying circuit. In fact, the electrodes of the photoconductive detector would be bonded directly onto the input and earth tracks of the circuit in such a design. The whole unit can be placed in a metal box, to act as a screen from outside electrical signals. Electrical noise should be reduced to a minimum using this concept. As far as improving the bandwidth of such a system, this is limited in the main by absorption within the GaAs detection substrate. A pulse length of 140 – 150 fs at the end of the fibre is still short enough to detect frequency components out to a few THz, using a photoconductive switch, and would be useful for security-type measurements. Etching the substrate back to almost the LT-GaAs layer would provide a way of decreasing the absorption within the receiver chip and is an approach which deserves further attention. Attachment of a lens would also improve the collection efficiency, but this is at the expense of angular resolution.

6. Terahertz Scattering Measurements

This chapter of the thesis concentrates on presenting results obtained using the terahertz radiation scattering spectrometer described in the previous chapter. It has already been discussed in chapter three how the scattering of THz radiation can be used to determine the characteristic size, location, and even texture of objects concealed within other media. The accurate detection and interpretation of radiation scattered by structures is particularly important in the development of stand-off security systems, for example. It is known that a broadband terahertz time domain spectroscopy system has an intrinsic advantage over single-frequency systems, for example Quantum Cascade Lasers, in that it can in principle, deliver spectroscopic information. This may not always be essential for routine surveillance, in which a contrast image is built up by, for example, plotting the peak electric field over each pixel, but it may be relevant to more specialist surveillance, for example scrutiny of mail in sensitive situations such as at Embassies. Moreover, the capabilities developed in the present work are highly relevant to such applications as: monitoring the progress (in location, time and chemical activity) of a reaction in a pharmaceutical process within a reactor vessel; monitoring the presence of impurities in a food mixture; or determining the nature and position of a foreign body within a fabricated plastic or composite structure.

To our knowledge, this investigation is the first time in which a fixed sample and rotating detector experimental configuration has been used at THz radiation frequencies as a direct analogue of a conventional x-ray system (the so-called CAT scanner). Such a system allows the possibility of the application of algorithms developed in that field to be used for THz images. Furthermore, the arrangement is likely to be more acceptable if a personnel-scanning system were to be developed; the suspect could remain standing whilst the detector was rotated around him/her.

This chapter begins with a review of common imaging modalities, before a more thorough discussion of images obtained using THz radiation is given. As alluded to above, this work uses the experimental system whose construction is discussed in detail in chapter five. Data obtained with this fixed sample and rotating detector is subjected to the signal reconstruction processes developed in chapter four, before being fed

through a conventional, widely available algorithm (the back projection method) from computed tomography. This back projection method that is used to reconstruct the image is outlined, before the experimental procedures used for data acquisition are described. These include construction of the phantom objects and how measurements of the scattered radiation were made. Finally, the reconstructed images obtained using this technique are presented.

6.1 Imaging modalities

Both two- and three-dimensional imaging modalities are currently widely available and used in the field of x-ray imaging. These are most widely found: in medical imaging, for example, x-raying limbs to check for fracture; and security screening in the inspection of luggage at airports and sealed packages at Embassies. The most common two-dimensional imaging technique is radiography, which has been around since the discovery of x-rays. Over time, radiography techniques were developed to fulfil the demand which arose from the desire to produce more complex images, revealing more information about a sample's internal structure. The most useful three-dimensional imaging modality is known as computed tomography.

The technique of radiography has been around for the past one hundred or so years and produces a pixel by pixel image of the unabsorbed x-ray intensity after passing through an object. A flattened planar image is produced whose contrast is derived from the relative intensities of the partially absorbed detected beam in reference to the intensity of an unabsorbed beam. By its very nature, the image produced has no depth information.

The technique of computed tomography involves applying some form of mathematical reconstruction process to a data set to produce a two-dimensional image of the object's cross-section. In its simplest form, M parallel beams pass through a single plane of the object of interest and their intensities are measured. The sample (or source and detector system) is then rotated through an angle θ, and another set of intensity measurements recorded. Each angle at which the intensities are measured is known as a projection. After rotation of the sample (source and detector) through 360 degrees, a set of N projections exist, each of which contains information from one set of the M parallel

beams. This data can be written in the form of an ($N \times M$) matrix and is subjected to some type of reconstruction algorithm to produce a two-dimensional image of the plane of the sample under investigation. In other words, the image produced is a cross-section of one slice of the sample. A number of slices can be stacked together to produce a three-dimensional image of the object, with each slice containing information on the object's shape and internal structure.

6.1.1. Image reconstruction of computed tomography

Numerous algorithms have been developed over time to enable the reconstruction of images from experimentally obtained projection data. Each of these algorithms is based on the "Fourier Slice Theorem[134]." This states:

> The 1-dimensional Fourier Transform, $S_\theta(\omega)$, of a parallel projection, $P_\theta(t)$, of an object, f(x,y), at angle θ is a slice of the 2-dimensional Fourier Transform, F(u,v) of f(x,y) forming an angle θ with the u axes.

Figure 6.1 pictorially illustrates this principle.

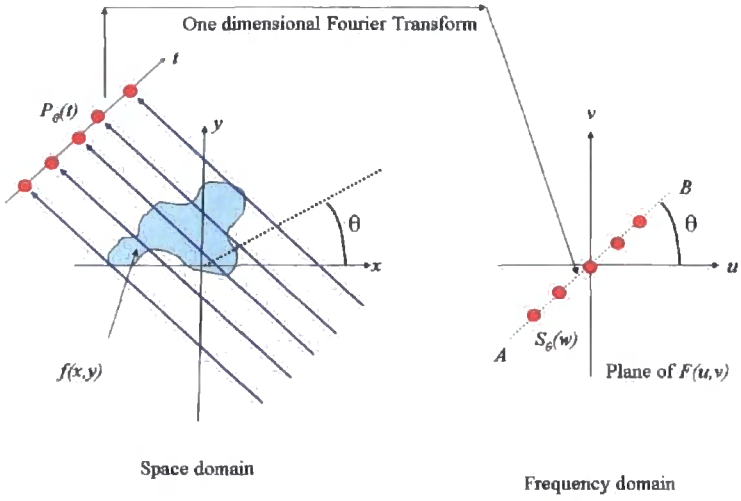

Figure 6.1: Pictorial representation of the Fourier Slice Theorem.

The resulting projections can be summed over all angles to give an estimate of the two-dimensional Fourier Transform, along radial lines in the frequency domain. In practice, imaging using this theorem is quite complex because the method involves taking both

inverse two-dimensional Fourier Transforms and coordinate shifts. Inevitably, various algorithms have been derived to simplify the process. The most widely used is the filtered back-projection method, and we use a variant of this, combined with the signal processing technique of chapter four, for our data reconstruction. In brief, the filtered back-projection method can be described as follows[135]:

1. Each set of projection data is Fourier Transformed in one-dimension:

$$S\ (\omega) = \int P_\theta\ (t) e^{-2\pi i \omega t} dt\ ; \tag{6.1}$$

2. A filter is constructed in the time domain, which is a ramp filter function multiplied by a smoothing filter:

$$T(\omega) = |\omega| \times M(\omega); \tag{6.2}$$

3. The inverse one-dimensional Fourier Transform of the product of the projected FT and filter is calculated:

$$Q(x\cos\theta + y\sin\theta) = Q(t) = \int S_\theta(\omega)|\omega| M(\omega) e^{2\pi i \omega t} d\omega; \tag{6.3}$$

4. This inverse Fourier Transform is back projected into the space domain:

$$f(x,y) = \int_0^\pi Q(x\cos\theta + y\sin\theta) d\theta. \tag{6.4}$$

A variant of this method, combined with the signal processing techniques of chapter four was used to produce the reconstructed images of various phantoms. This mathematics is given in section 6.2.1.

6.1.2. A history of terahertz imaging

Various work has been undertaken in the general area, which is collectively known as terahertz imaging. Most of the systems used to produce THz images have been variants of the radiography type method. Here, samples are imaged in a transmission geometry and, due to the absorption of THz radiation, most of the samples imaged have been "thin." By the application of suitable algorithms to the experimental data, a terahertz image of the sample can be built up. The sources used in such investigations have been both pulsed and continuous. Most of the images taken have been either two-dimensional or pseudo three-dimensional[25].

The first imaging in the far infrared region was reported in 1976 by Hartwick *et al.* They produced images of an uncovered key, and the same object housed in both a vinyl box and rubber, using a far infrared imaging instrument based on a lasing source[136]. Hu and Nuss were the first to report imaging using THz waves, produced and detected using pulsed, electro-optic systems, in 1995[137]. Their work described applications involving the real time scanning of package inspection and determination of the chemical content of organic objects. Further work has been undertaken by Mittlemann *et al*, who performed two-dimensional imaging using THz radiation in a reflection modality[113]. In their work, a floppy disk was imaged by raster scanning the object across the THz radiation focus. The reflected THz radiation was then collected and used to produce two different types of image. A conventional tomographic image was constructed by computing the total reflected THz power at each pixel and building up a grey scale map, but the internal structure of the sample was also revealed by investigation of the temporal profile of the pulse. A very simple type of signal processing was applied to the reflected waveforms (which has already been outlined in chapter four) to sharpen the reflected pulses received from the various sample interfaces. These reflected pulses provided information on the depths and thicknesses of the various layers within the disk structure.

X.-C. Zhang's group has also undertaken various forms of THz imaging, and has investigated the internal structure of defects within foam in a reflection measurement[138]. Planken *et al* have reported THz imaging of the contents of a closed match box in transmission geometry and dynamic images of CH_3F gas diffusing through a polystyrene block[121]. This image was constructed using the commensurate echo pulse transmitted through the gas. More recently, Pearce *et al* have reported the production of two-dimensional images of cross-sectional slices by the use of wide aperture reflection tomography. Using a THz transceiver, reflected rays from a horizontal slice of a sample were recorded at different angles and the image reconstructed using the filtered back-projection method[139].

The first report of true three dimensional imaging was reported by Nguyen *et al*[140]. They used a Quantum Cascade Laser to image both the internal and external structure of phantoms. Their measurements combine the high radiation powers possible from a

QCL with a filtered back projection method for the reconstruction of the image. Of course, such a method only produces an image of the object of interest, and no spectral identification can take place.

A thorough review of THz tomography using pulses of radiation has been given by Wang and Zhang[141]. Their review paper outlines all possible types of tomographic imaging that can be undertaken using THz radiation, namely: THz diffraction tomography; THz computed tomography; THz tomography with a binary lens; and THz digital holography. The main message of this review is that the various THz imaging modalities are only valid under certain physical conditions. In THz computed tomography for example, the target beam must be smaller than the Rayleigh range and this beam must be well described by a Gaussian profile in this range. For each imaging modality, the mathematics behind the image production is described and some simple experimental results are presented.

6.2 THz tomographic imaging using signal processing

As already outlined, the imaging results presented later in this chapter combine the experimental techniques developed in chapter five, with the signal processing algorithms developed in chapter four. The images produced are a form of computed tomography, and are reconstructed using the back projection method. A single THz source was used with an individual rotating detector. However, the same measurements could be performed using three or four detectors placed at various angles around the sample. Of course, this would require careful engineering of the experimental rig. This is further discussed in the summary at the end of this chapter, and in chapter seven. After obtaining the scattered radiation in the manner of the experiments described below, each scan was signal processed before being computed into an image.

The signal processing took place over various steps. First, each scan was initially levelled, removing the non-zero background component of the current from the photoconductive emitter. This levelled data was then subjected to the usual reconstruction algorithm, described in chapter four, with the reconstructed source pulse being a convolution of the seed function with the freespace THz electric field. The THz tomographic images were then formed using the back projection method described

below. It should be noted that the theory presented concerns the production of a two-dimensional image of the cross section of one vertical plane of the phantom object. To build up a three dimensional picture requires raster scanning of either the imaging unit or the phantom in the vertical direction. A number of cross-sectional image slices could then be stacked on top of each other to produce the three dimensional image.

6.2.1 Back projection theory

Radiation incident on an object consisting of vertical metal or dielectric rods, is scattered in the horizontal plane; and therefore information relating to the position of the scattering centres can be collected by moving the detector through a horizontally oriented arc, centred within the object area. The reconstructed signals then show pulse delays that are dependent on both the coordinates of each scatterer and on the detector angle. This means that the back projection becomes essentially a two dimensional problem, which greatly reduces the computational complexity.

Consider a scattering object, S having coordinates (x, z) in some irradiated plane at constant height, y. The THz beam is focused to the point $(0, F)$ in this plane, with the detector, D rotating about the origin at a radius, R. When the detector is off-axis at some angle θ, it has coordinates $(R\sin\theta, R\cos\theta)$. In this case, the extra optical path length from the scatterer to the detector, relative to another scatterer at the origin, is given by (SD - SF) where:

$$SD^2 = (x - R\sin\theta)^2 + (z - R\cos\theta)^2 \tag{6.5a}$$

$$SF^2 = x^2 + (z - F)^2. \tag{6.5b}$$

In most measurements the detector is placed such that when $\theta = 0$ it is at the THz focus i.e.) $R = F$. This arrangement is shown in figure 6.2.

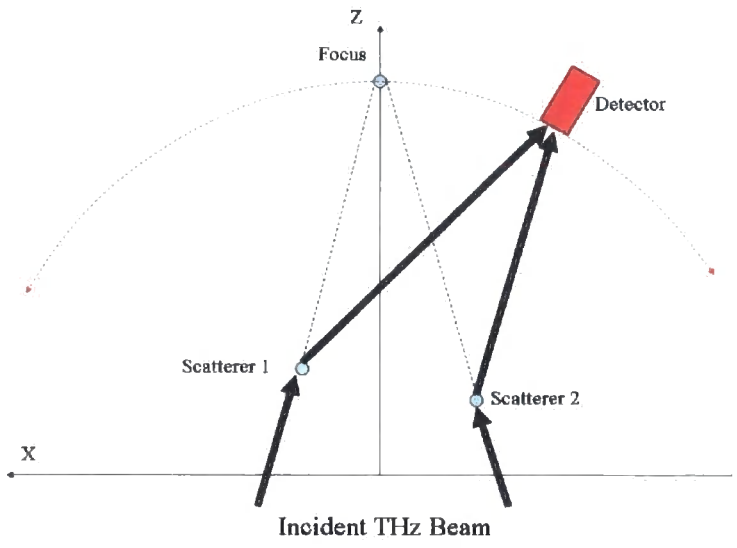

Figure 6.2: Layout of tomography system having rotatable detector.

In this diagram z is (as usual) the direction of the propagation of the wave, and x and y are the two transverse directions that form a right-handed coordinate system. For each pixel in the field of view enclosing the sample, and for each position of the detector, the expected time delay can be calculated, and the corresponding value of the reconstructed signal for that time delay selected. Summing over the range of detector angles produces the back projected image.

When the detector is only at a small angle, and is thus close to the incident beam focus, the time delays are relatively insensitive to the scatterer positions, and this part of the data does not lead to a well resolved image. As the detection angle is increased, the spatial resolution rapidly improves. The spatial resolution is also dependent on the length of the THz pulse and bandwidth. If the detector is scanned over a range from $-\alpha$ to $+\alpha$, and the bandwidth limited time resolution is t, the appropriate resolution limits are:

Longitudinal resolution: $$\Delta z \sim {ct}/{(1-\cos\alpha)}; \tag{6.6a}$$

Transverse resolution: $$\Delta x \sim {ct}/{\sin\alpha}. \tag{6.6b}$$

If the detector is scanned over a 180° range from -90° to +90°, these resolution limits become equal and assume the value *ct*.

Two forms of back projection were used to construct the images: additive and multiplicative. In additive back projection, after reconstruction of the experimental data, the value of each pixel is built up by either the addition (or subtraction) of the part of the signal, having delay equivalent to the delay of the beam which was transmitted directly through the phantom and is detected at an angle of $\theta = 0^{\circ}$, to the initial neutral image. In this case, the initial image is taken to be zero at all places. The reconstructions from each angle are added if a dielectric is being investigated (PTFE or biotin powder) or subtracted if scattering images from metals are being investigated. The multiplicative method proceeds in a similar way, but this time the initial, fiducial image, having a value of unity at all points, is multiplied by the correct part of the signal at each angle, pixel by pixel.

6.3 Experimental procedures

The experimental results which are about to be presented, were obtained using the specially constructed terahertz setup described in the previous chapter. This, to our knowledge, is the first time that a system, with a fixed sample and rotating detector has been used for undertaking THz imaging. As discussed in that chapter, only one other group has reported measuring the angular profile of scattered radiation by some form of inhomgeneous media, but these results were carried out using a commercially available spectrometer. The development, within TeraNova, of a short pulse near infrared laser with a fibre-coupled output provided partial motivation for this work, but as outlined in chapter five, this laser system did not produce any fruitful results, and the system was eventually powered using a laser from the Rutherford Appleton Laboratories loan pool. Once the system had been built, numerous phantoms were constructed to act as scatterers of the THz radiation within the experimental rig.

6.3.1 Construction of phantoms

Motivated by the fact that the realistic application of such a system would be to identify hidden objects, it was decided to construct test objects which would contain some sort of scattering object, hidden in what can be described as a "mechanical vacuum." The

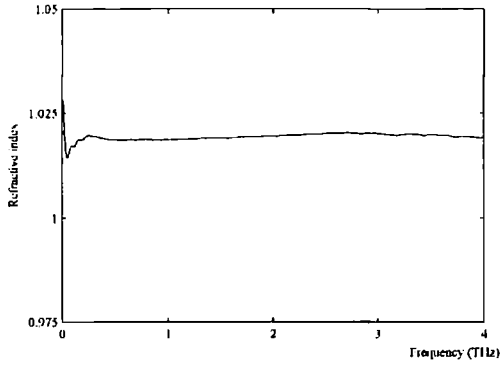

Figure 6.3: THz refractive index of expanded polystyrene.

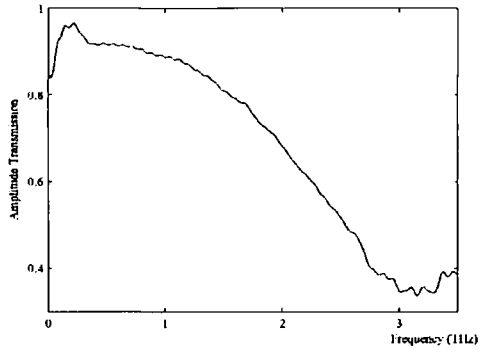

Figure 6.4: Transmitted THz spectrum through expanded polystyrene.

hidden object could consist of pure scattering material (e.g. metal) or scatterer with a THz spectral fingerprint (e.g. an organic or inorganic powder). A mechanical vacuum is some substance which is opaque at visible wavelengths, but transparent at the wavelengths used to investigate the object. Expanded polystyrene is an excellent example of such a material at THz frequencies. Figure 6.3 shows the refractive index of a 5.36 mm thick piece of polystyrene and its corresponding transmission spectra is in figure 6.4. As can be seen, the refractive index is approximately unity. In fact it is 1.018, across a wide spectral bandwidth (200 GHz - 4 THz, the bandwidth of the transmission THz-TDS); the transmitted amplitude is approximately 90% over the useful spectral range of the scattering system (300 GHz – 1.5 THz). Cylinders, of diameter 1.37 cm, were fabricated from this polystyrene to provide the mechanical vacuum into which scatterers could be inserted.

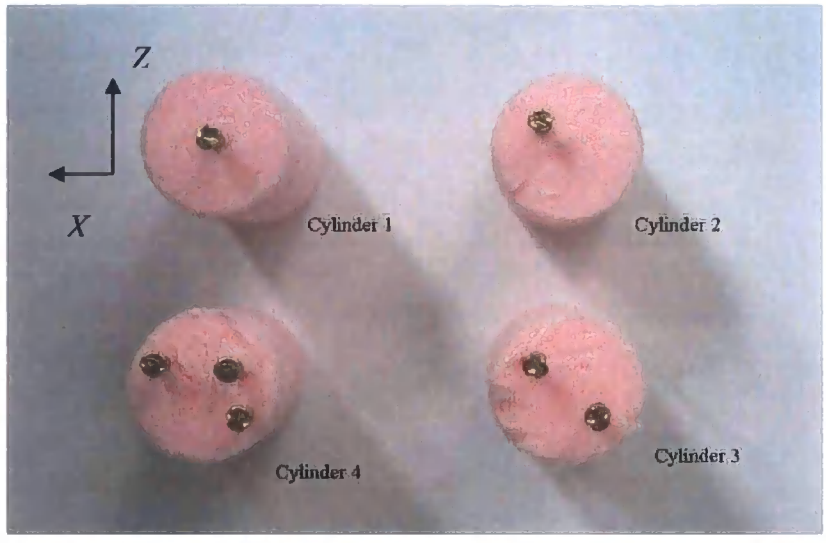

Figure 6.5: Photograph of scattering phantoms.

Two distinct types of scatterer were then placed into these cylinders. First, metallic panel pins of diameter 1.40 mm and length 19 mm were inserted, in various configurations, into the polystyrene cylinders. The most simple scattering object contained one centred pin, with the most complex containing three off-centre pins. Their co-ordinates, (x, z) in millimetres with respect to the centre of the foam cylinder were determined to be:

Cylinder Number	Pin co-ordinates (mm)
1	**(0 , 0.3)**
2	**(2.9 , 1.53)**
3	**(1.7 , 3.91) , (-0.85 , -3.05)**
4	**(-3.06 , 3.4) , (1.53 , 3.57) , (-3.74 , -3.06)**

with x across the page and the z direction up the page. Figure 6.5 shows a photograph of these phantoms, with the metallic pin heads just visible at the top surface of the cylinders.

Metallic pins were chosen since they are good scatterers of radiation over a wide range of frequencies. The pin diameter was chosen after carrying out simulations, using Mie theory, to determine the expected scattering cross-section in both **E** and **H** polarisation.

The polarisation state is defined as the component of the EM field parallel to the length of the cylinder; in other words which part of the field (**E** or **H**) lies in the y direction. Two further cylinders were also constructed from the same material, but this time with an off-centred hole of diameter 2mm bored out from the cylinder, which were filled with PTFE powder, of average particle size 100 μm, and biotin respectively. It was hoped that the particles would sufficiently scatter the incident radiation to be able to locate the position of it within the structure, whilst also perhaps being identified using spectral fingerprints.

Figures 6.6 and 6.7 show the differential and total scattering widths respectively for both **E** and **H** polarisations, using Mie type solutions for Maxwell's equations[95]. The red cross-sections correspond to **E** polarisation and the black to **H**. These cross-sections are also dependent upon scatterer radius, with the dashed lines representing metal rods of radius 0.25 mm, whilst the solid lines are for rods of radius 0.7 mm, approximately that chosen for the phantoms. Investigation of the differential scattering width for the larger rod diameter shows that the scattering can be split into two major components: narrow angle diffraction over an angular range of approximately $\pm 20^{\circ}$, and wide angle specular reflections. For smaller rod diameters, this cross-section is more isotropic, but the **H** polarisation width is in general weak. If a similar simulation were carried out for a higher frequency incident wave, the narrow angle diffraction would be sharper, but over a smaller angular range, and the specular wide angle reflections would be similar.

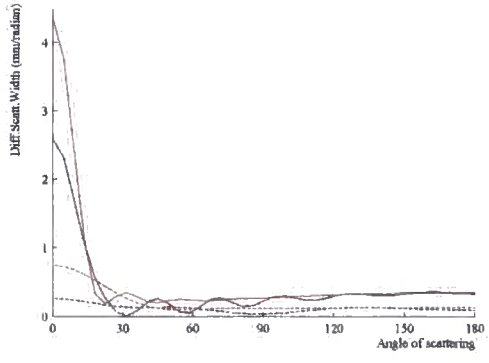

Figure 6.6: Differential scattering cross-section, at a frequency of 0.5 THz.

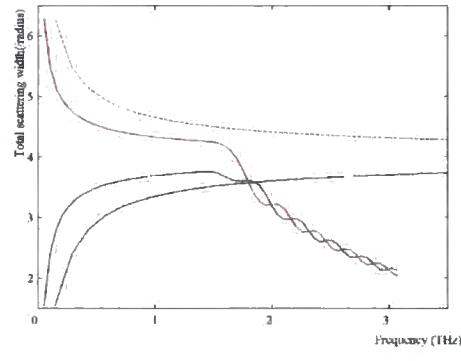

Figure 6.7: Total scattering cross-section.

Further simulations were also carried out to investigate the form of the total electric field scattered by the actual constructed phantoms and one such example is shown

below. Figure 6.8 is the total electric field, for a wave of frequency 0.3 THz, passing through cylinder 1, containing 1 centred pin, whilst figure 6.9 is the corresponding field pattern, but this time the incident wave is of frequency 1 THz. Figures 6.10 and 6.11 are corresponding plots for cylinder 3, the phantom containing two off-centre metal pins.

As predicted by the differential scattering cross section (figure 6.6) most of the low frequency wave is diffracted around the edge of the metallic cylinder, with only a small amount of specular, wide angle scattering. A long distance from the scatterer, the field is approximately the same as when no scatterer is present. At higher frequencies, a similar effect occurs, though the angular spread of the diffracted beam is narrower. For the higher frequency wave, interference between the forward scattered wave from the cylinder nearest the detector can also be seen.

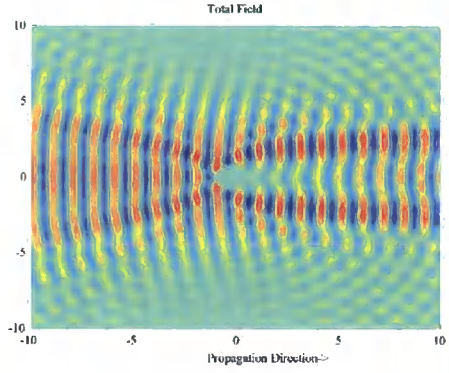

Figure 6.8: Total electric field for scattering from cylinder 1 at 0.3 THz.

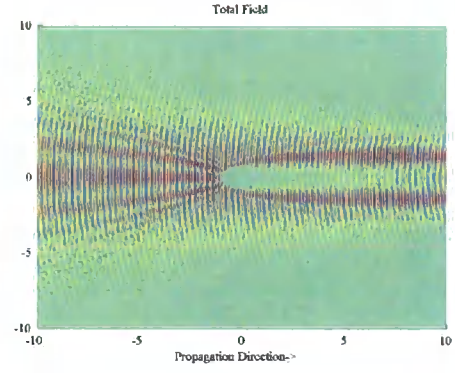

Figure 6.9: Total electric field for cylinder 1 at 1 THz.

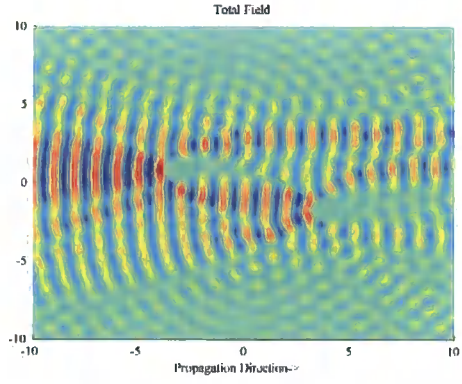

Figure 6.10: Total electric field for cylinder 3, at 0.3 THz.

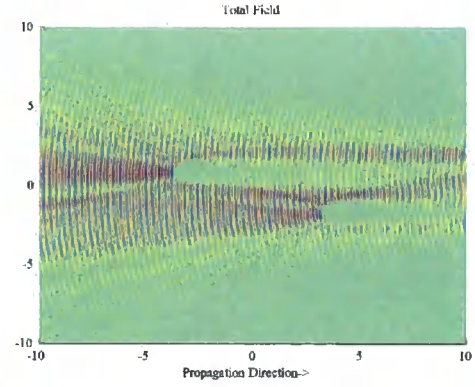

Figure 6.11: Total electric field for cylinder 3, at 1 THz.

6.3.2. Polarisation of a THz spectroscopy system

It is rather simple to change the polarisation of a THz experimental system that has been constructed using photoconductors. The THz electric field polarisation is always dominated by the direction of the field applied to the emitter, which as explained in chapter two, is of the order of hundreds of kV/m. Even though the near infrared laser beam is polarised, its field is small compared to that of the bias field, so it has negligible effect on the polarisation of the THz. Thus, rotating the emitter through an angle of 90° has the effect of changing the polarisation of the THz field from horizontal to vertical. Similarly, the receiver must be rotated by the same amount to have maximum detecting ability. It should be noted that the efficiency of photoconducting antennas does depend on the polarisation of the optical gating pulse, but only when optical excitation takes place very close to the electrodes[142]. In general, the polarisation of the THz radiation field does not affect the measurements of the field transmitted or reflected by a sample: it is only chiral compounds which can change the polarisation state of the field. Castro-Camus *et al* have developed THz detectors that can measure both polarisation states of the THz beam simultaneously, which are most useful if chiral compounds are to be investigated[143]. However, in our measurements we are only interested in the scattering of the THz radiation in one plane and thus have designed the experimental system accordingly.

6.3.3 Experimental measurements

The phantoms were placed at the centre of rotation of the detector unit, with the focus of the THz beam on the receiver. By setting the distance from the centre of rotation to the detector as 4.5 cm, the whole of the phantom width is illuminated by the converging THz beam. Initial measurements were taken using **H** polarisation, in other words, having the electric field parallel to the diameter of the rods, since this meant that no change was required to the experimental system. The system was initially built to operate in **H** polarisation because all previous experimental systems had been designed to operate in this way due to the design of the emitter mount, which was constructed to be mounted vertically on a standard optical post. However, even though the diameter of the rods was chosen so that the scattering should have been approximately the same in both polarisations, the scattering data obtained were not particularly good. Therefore,

the experimental rig was reconfigured to operate in **E** polarisation, with the **E** field thus becoming perpendicular to the rods' diameter, or parallel to their length. This polarisation has the **E** field out of the plane of the paper in figures 6.2 and 6.4. All measurements presented were obtained in this polarisation.

In all the measurements undertaken an initial reference pulse, with no phantom in the beam, was recorded. After this, the THz pulses transmitted through the cylinders and scattered at various angles were recorded. Initially, scattering angles of between ± 5° and ± 20° were recorded in five degree steps to make preliminary measurements. It was only over this angular range that the first, unclear **H** polarisation measurements were made before the system was converted to **E** polarisation.

These initial **E** polarisation measurements recorded the THz electric field over a long time. Analysis of this data indicated that it was only necessary to record the main pulse and first system echo, along with a small amount of background before the main pulse to allow for changes to the delay time of the main pulse centre, at the various scattering angles. In effect this meant that a 40 ps THz pulse needed recording. Calculation of the Nyquist frequency, defined as half the maximum frequency of the discrete system, was used to determine the minimum translation step size. Since the system cut-off (the point at which the source power becomes too weak to be useful) is 1.5 THz a Nyquist

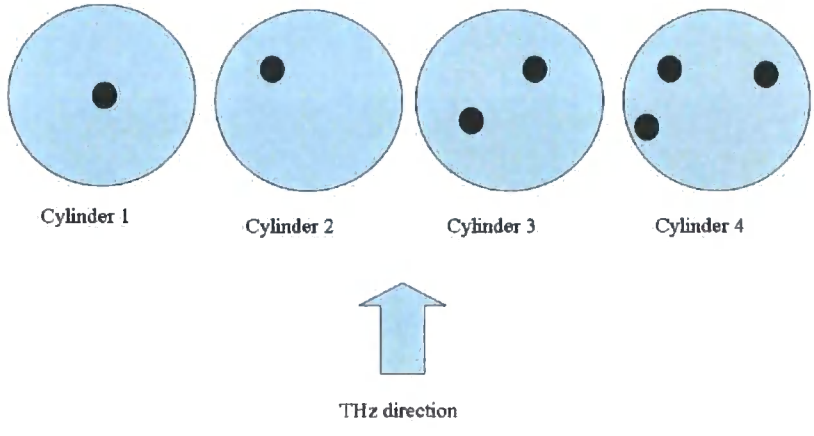

Figure 6.12: Layout of phantoms with respect to terahertz beams (low resolution).

frequency of 3 THz is valid. This indicates that the minimum step size of the translation stage only needs to be 25 μm: this longer step size speeds up the data acquisition time, reducing the scan time by over one half. Figure 6.12 shows the orientation of the scatterers with the various cylinders, relative to the incoming THz beam, for the first set of low resolution experiments.

After analysis of the results, it was decided to take measurements over a wider range of angles to increase the resolution of the system, in the z (propagation) direction as described by equations (6.6a) and (6.6b). Once again, a reference scan was measured; the scattered radiation profile over a range of angles from -90° to +90° in ten degree steps was then experimentally obtained. The phantom layouts for these experiments are shown below in figure 6.13.

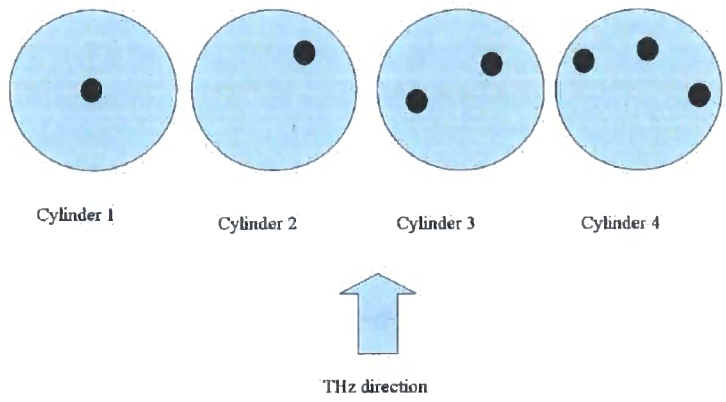

Figure 6.13: Phantom layout for high resolution measurements.

Analysis of this set of results showed that the scattered power detected from the phantoms containing more than one pin was rather low. To improve the signal to noise ratio of the system at non-zero scattering angles, it was decided to move the detector away from the THz focus towards the sample. The detector was set in a position such that it was only 2 cm away from the centre of rotation; when it was at the THz beam focus this distance was 4.5 cm. This meant that the distance from the parabolic mirror

to the detector was reduced to 12.5 cm. In this case, the experimental detection system

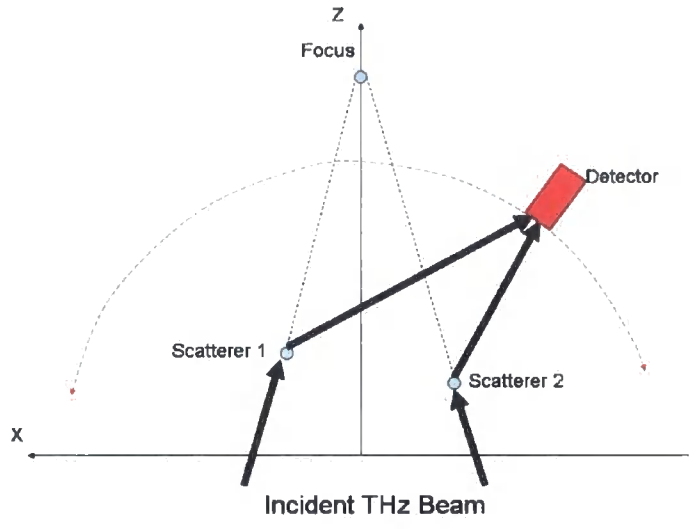

Figure 6.14: Detection arrangement, receiver off-focus.

arrangement is as shown in figure 6.14, but the equations given in section 6.2.1 still hold: of course, *R* and F now take different values.

This experimental arrangement was used to measure the scattered radiation profiles from the fourth cylinder phantom and the cylindrical phantoms containing the biotin and PTFE powders. The orientations of the phantoms for these results, with respect to the incoming beam, are shown in figure 6.15.

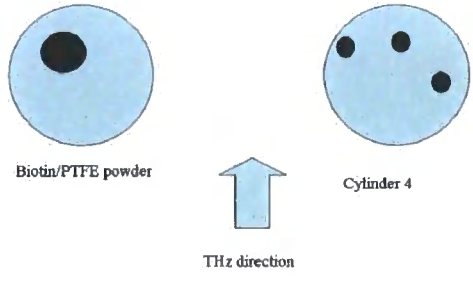

Figure 6.15: Cylinder orientation, receiver off-focus.

6.4 Results

This section of the chapter is a presentation of the results obtained in the different experimental arrangements already described. It should be noted from chapter five that the cut-off frequency of the fibre-fed THz detection system is approximately 1.5 THz. Thus, the full-width of the reconstructed source pulse can be reduced to ~ 1 ps before noise becomes excessive.

6.4.1. Low angular resolution experiments

The first set of results presented are for scattering from the foam cylinders containing metal pins in **E** polarisation and are obtained by back projection using the additive projection method. The angular range of each of the scans is $0^{\circ},\pm 5^{\circ},...,\pm 20^{\circ}$. Figure 6.16, below shows the back projected image from each of the four foam cylinders,

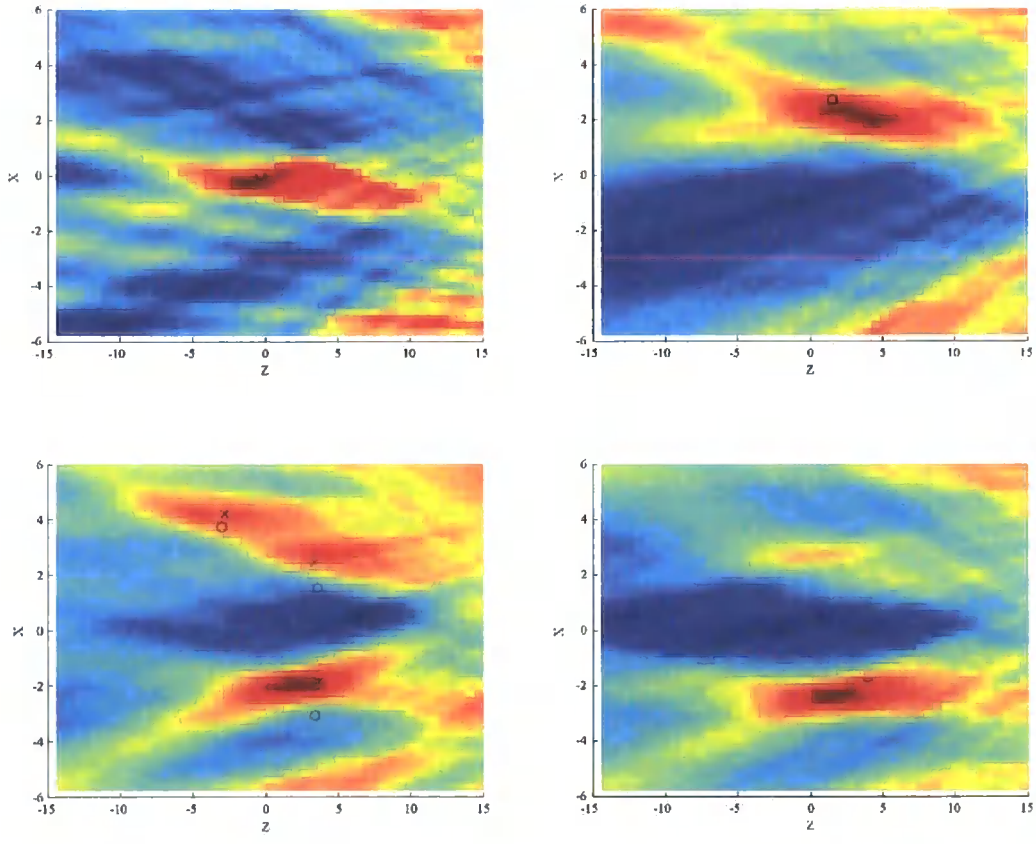

Figure 6.16: Back projected image from phantoms using angular range of -20° to +20° in 5° steps. Clockwise from top left: cylinder 1, cylinder 2, cylinder 3 and cylinder 4.

which are presented in ascending cylinder order, clockwise from the top left. The black circles on each plot show the expected position of the cylinders. Reconstruction parameters of $p = 2, q = 0, r = 5,$ were used to form the filter.

The first thing to note from the image is that the resolution is much greater in the x-direction than the z-direction i.e. the resolution is much better in the direction perpendicular to the propagation of the THz beam. The resolution of the single centred pin (top-left image) is approximately 5 mm in the propagation direction, and 1 mm in the direction perpendicular to this. This is in good agreement with the expected resolution from equations 6.5a and 6.5b. Inspecting the back-projected image for the fourth cylinder (which contained three pins) shows that the individual pin having a negative x coordinate is well resolved, but the images of the two pins having positive x coordinates overlap each other and are not clearly resolved, due to lack of z resolution.

Comparison of the images with the expected positions obtained from the pin coordinates, shows that, for the two cylinders containing single pins, there is good agreement between expected and reconstructed positions. For cylinder 3, the reconstructed pins are measured to have a separation of 7.2 mm, in good agreement with their separation according to the coordinates (7.4 mm). The discrepancy seen between expected and reconstructed positions arises from a rotation of the phantom between the photographed image and the experimentally obtained reconstruction. Finally, comparison of cylinder 4 with the expected positions of its pins shows that the reconstructed image reproduces the expected positions fairly well. There is an offset of approximately 1mm in the positive x direction between expected and reconstructed positions, indicated by the crosses. This indicates that the phantom was not quite aligned over the centre of rotation.

6.4.2 High angular resolution experiments

To improve the resolution of the reconstructed image in both directions (but especially in the x direction) the scattered radiation profile was measured over an angular range of $\pm 90^\circ$ in 10° steps, which should theoretically make the resolution the same in both directions. Figure 6.17 shows the scattered data over an angular range of 0° to $+90^\circ$,

with a reference scan (green) for cylinder 2, one off-centred pin. The same data is presented in figure 6.18 after reconstruction, using the technique described in chapter four, with parameters $p = 2, q = 0, r = 5$. The reconstructed reference scan is shown in blue.

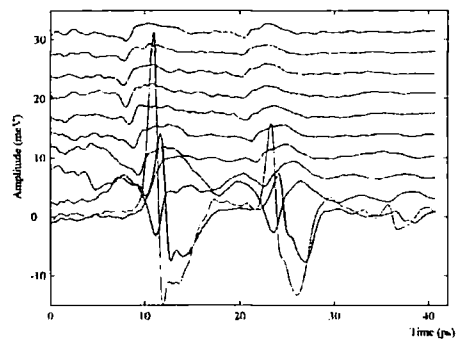

Figure 6.17: Raw data, positive scattering angles, cylinder 2.

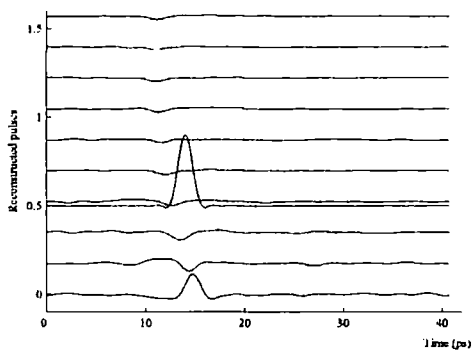

Figure 6.18: Reconstructed data, positive scattering angles, cylinder 2.

Applying the back projection method to this reconstructed data, with the similar data set obtained for negative scattering angles, produces the images for each cylinder shown in figure 6.19. From top left in a clockwise direction these are: cylinder 1, cylinder 2, cylinder 3 and cylinder 4. For each image, the x and z resolution are the same, and for the best image (cylinder 2) this resolution is about 0.3 mm, in good agreement with that given by equations (6.6a) and (6.6b). Inspection of the images reveals that the source power on the positive x side is reduced in comparison to negative x. This was thought to be due to a slight misalignment of the detection system; the beam from the second parabolic mirror must not be converging in a direction which is perfectly perpendicular to the detector. Consequently: the best resolved image is for the single off-centred pin in the negative x direction; while for cylinders 3 and 4 the pins having negative x-coordinates are far more clearly resolved. For the cases of phantoms containing more than one pin, the separations of the pins in the reconstructed images are in good agreement with the values measured from the phantom.

It is worth commenting here that this apparent misalignment was not present in the first set of low angular resolution measurements, but it should be noted that the system had to be rebuilt between the two sets of measurements. This was due to emitter failure (one of the wires connecting the emitter electrodes to the mount came loose) plus the

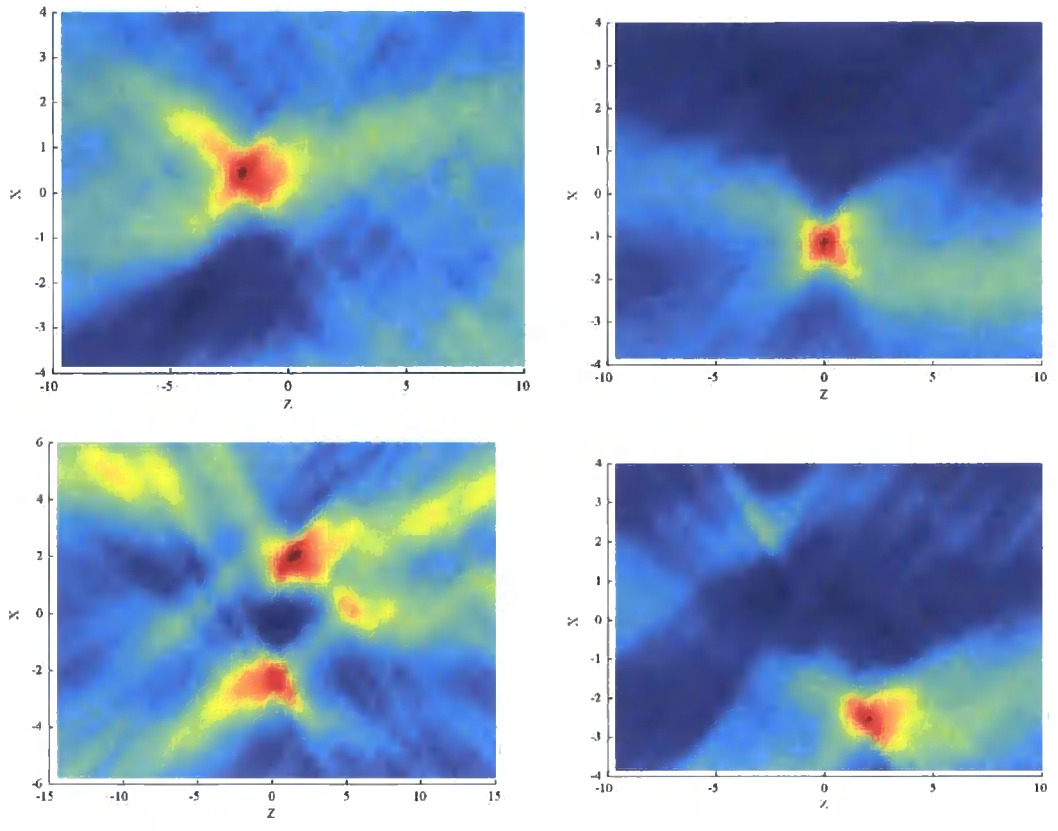

Figure 6.19: High resolution back-projected images, using angular range -90° to +90° in 10° steps. Clockwise from top left: cylinder 1, cylinder 2, cylinder 3 and cylinder 4.

necessity to realign the laser cavity. A combination of these factors meant that it was thought beneficial to realign the THz optics of the system, which led to this non-perpendicular convergence of the THz beam from the second parabolic mirror to the detector.

The back projected image places the (supposed) single centred cylinder just off centre; this slight discrepancy between projected and actual position exists because the exact position of the pin, including its orientation once in the sample, are unknown quantities. Only alignment of the pin head over the approximate centre of rotation is actually possible. Due to both the low source power for positive x and experimental noise, the back-projected image for cylinder 4 suffers from a lack of clarity. The low source power produces a very poorly resolved image of the single pin having large positive x coordinate, but also returns a spurious image indicating the possible placement of a

further scatterer, between the two pins nearest the detector. This is due to interference effects from the waves scattered off the two actual pins in the phantom.

6.4.3 Measurements with off-focus detector

To overcome the lack of signal quality for the scattered radiation from cylinder 4, it was decided to undertake another set of measurements over the angular range -90° to $+90^{\circ}$, but with the detector moved off focus towards the phantom. This improves the signal amplitude received at non-zero angles and allows better collection of the scattered radiation. Once again, the THz optics of the system were realigned, to correct for the lack of perpendicular convergence in the previous results. After realignment of the THz optics, the system was optimised with the THz focus on the detector, before this unit was translated 2.5 cm towards the rotation point.

Figure 6.20 shows the reconstructed image from the scattered radiation from cylinder 4. This is produced using the multiplicative back projection method. The three pins are all clearly seen, and are at the positions of the dark red reconstructed amplitudes; but since the detector is now off-focus, the resolution in the z direction especially has once again

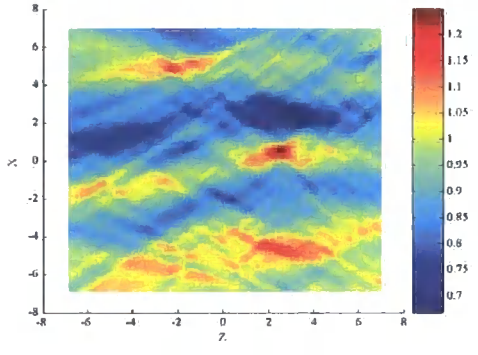

Figure 6.20: Cylinder 4 with unfocused detector.

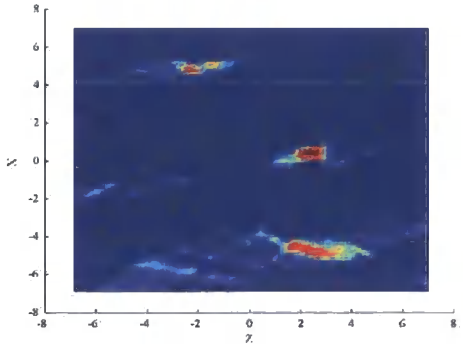

Figure 6.21: Contrast enhanced image of cylinder 4 with unfocused detector.

decreased. Lines of higher back projected signal exist along directions of constant x, whose amplitude decreases further away from each scatterer. To improve this image, the technique of contrast enhancement can be applied. This is a well known tool used in the reproduction of images. Here, using the indicator bar on the right of figure 6.20, a value of back projected amplitude can be set below which all parts of the image are sent

to zero. This then just leaves clearly defined areas with high signal amplitude seen in a zero background, shown in figure 6.21. The image in figure 6.21 has been produced by zeroing all points of the back projection having an amplitude of less than 1.1 in figure 6.20. In this image, the separations of three pins are measured to be 4.8, 6.4 and 9.5mm, which are in good agreement with the separations calculated from the physical coordinates of the phantom of 4.7, 6.6 and 9 mm.

Using the same experimental method as above, namely an angular range of 0° to $\pm 90^\circ$, with an off-focus detector, scattered radiation was collected from cylinders with a bored-out hole containing some type of scattering powder. Figures 6.22 and 6.23 show respectively the back projected image obtained from scattering measurements from a polystyrene cylinder filled with PTFE powder and a contrast enhanced version of this result. The reconstruction parameters used here were $p = 2, q = 0, r = 10,$ and the contrast enhancement threshold was set to be 1.8. A clearly defined off-centred image can be seen with diameter of a few mm. The position and size of the image correspond well with the expected image position; the image is off-centred in the x (transverse) direction more than expected, but this is due to the hole bored in the sample being not quite vertical. The limited bandwidth of the system unfortunately prevents spectral identification of the PTFE: the first absorption of PTFE in the THz region is at around 6 THz.

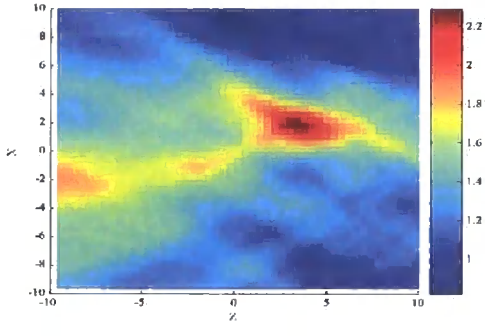

Figure 6.22: Cylinder filled with 100 µm PTFE powder, with unfocussed detector.

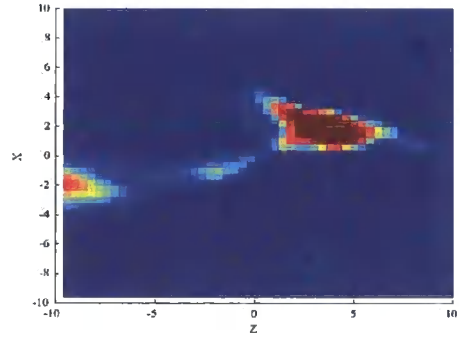

Figure 6.23: Contrast enhanced cylinder filled with 100 µm PTFE powder, with unfocussed detector.

A similar experiment was carried out using biotin powder as the scattering medium. Since this has spectral features over a much wider bandwidth than PTFE, see chapter

four for details, it was hoped that its spectral fingerprint could be used to identify it. The results obtained for scattering from biotin were unfortunately not very good: the 2-3 mm diameter of the bored hole filled with the biotin meant that the THz path through the scattering material was too large and too much absorption occurred. Consequently, the reconstructed image of the position of the biotin scattering material was not at all clear. Unfortunately, the loan pool laser had to be returned before a repeat of the biotin scattering measurements could be made, using a cylinder with a much smaller diameter bored-out hole.

6.4.4 Angular range requirement of the detector

As will be explained in the concluding part of this chapter, if such a system were to find a use in any real life application, the data acquisition time needs speeding up. One way of doing this is to reduce the number of angles used in the back projection of the scattered data to produce the object's image. Figure 6.24 shows the reconstructed image of the one off-centred cylinder using an angular range of $0^\circ, \pm 10^\circ, \pm 20^\circ, ..., \pm 90^\circ$, previously shown in figure 6.19, whilst figure 6.25 is the back-projected image of the same object, but only using data scattered at angles of $-90^\circ, -60^\circ, -30^\circ, 0^\circ, +30^\circ, +60^\circ, +90^\circ$. It should be noted that the pin is still clearly

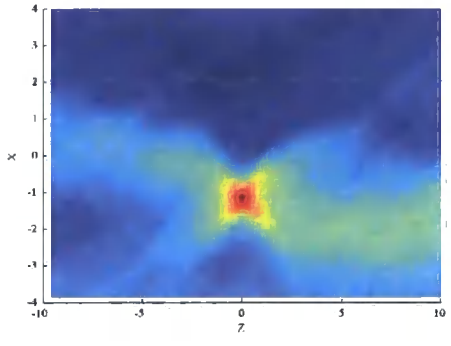

Figure 6.24: Reconstructed image of cylinder 2, all angles.

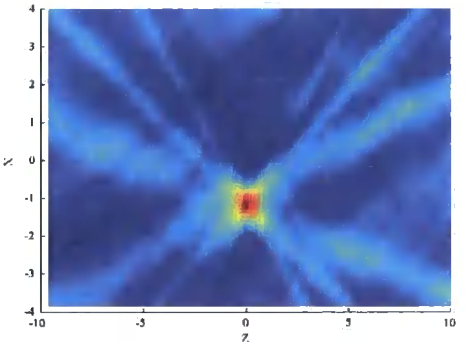

Figure 6.25: Reconstructed image of cylinder 2, reduced angular range.

resolved, with identical limits on the x and z resolution, when a reduced angular range is used. However, numerous lines appear in the reconstruction radiating away from the cylinder. At these points, the reconstructed amplitude is not completely cancelled. As more angles are used in the reconstruction, more weakly scattered specular waves are detected, and hence a clearer picture of the scattering object is built up. Applying

contrast enhancement to both reconstructions would result in the same image. Therefore, it is possible to collect scattered radiation over a reduced angular range and thus speed up the acquisition time.

6.5 Summary and conclusions

Work in this chapter has shown that it is possible, in principle, to construct an image of some phantom using back projected, signal processed THz pulses. THz radiation scattered from various specially constructed phantoms was measured using a specially constructed time domain arrangement. This system had the ability to record THz pulses over a wide angular range, and contained a detection unit gated by a femto-second pulse, which had propagated along a length of single mode optical fibre. After collection of the THz pulses scattered in a forward direction, over an angular range of -90° to $+90^{\circ}$, an image of the phantom illuminated by the THz beam was produced using a variant of the filtered back projection method. Here, the experimentally obtained THz pulses were first reconstructed, using the reconstruction algorithm of chapter four, before being back projected to produce the image of the sample. This method produced good images of scattering phantoms when the THz electric field was parallel to the large dimension of the scatterer.

The results obtained only produce a two-dimensional cross-sectional image of the object, but in principle this method can be easily extended to the third dimension by placing the sample under illumination on a y translation stage. This would allow the sample to be scanned in a vertical direction to the beam: cross sections obtained at a constant height, by angular scanning of the detector, would be stacked together to produce a three-dimensional image of the phantom.

If the techniques described in this chapter for the production of THz images, using a similar experimental system to that described in chapter five, are used to collect data and produce an image, the major problem that needs to be overcome is data acquisition time. Here it should first be noted that the signal reconstruction methods applied to the THz pulses before back projection actually remove most of the noise from the pulsed waveforms, and thus very little averaging is required at each point of the THz pulse

whilst it is being recorded. Also, due to the maximum frequency limit of the system, quite large steps can be used on the translation stage. However, even under these conditions, recording the THz pulsed waveform at one angle takes just over a minute because of the speed restrictions imposed by the motorised translation stage. Therefore, acquiring the necessary data to produce just one cross-section of the sample takes approximately 10 to 20 minutes, depending upon the number of discrete angles at which the scattered data is recorded. This is far too long a time for the production of an image in most applications, especially if a three-dimensional image was required.

Various ways can be envisaged to overcome the problems of data acquisition, some of which already exist, and some of which would require careful engineering. The major improvement that is required for any system working in a real-life environment is a method to drastically reduce the time of producing one THz waveform. This can most easily be overcome using a scanning delay line instead of motorised stepper translation stage[27]. Such technology does exist and some groups undertaking THz research use it as the delay line within their systems. These scanning delay lines can record a THz pulse at a rate of upto a few tens of hertz. Therefore, using such technology in the THz system would allow the acquisition of a single THz waveform (with enough averaging) in just over one second. It should be noted that in fact this applies equally to any commercial system which could be used to measure: simple THz transmission or reflection spectra; provide a two-dimensional planar THz image of a sample, when the object of interest is scanned through the THz beam; or in a system such as ours to build a cross-sectional image of a layer of the sample.

The second improvement, which would be required in the realisation of any tomography system, is the use of more than one detector working in parallel. Consequently, scattered waveforms could be collected at more than one angle simultaneously. This would provide a reduction in the number of discrete angles at which the detector would need placing to record a sufficient number of waveforms to produce the image. The work undertaken in section 6.4.4 shows that THz signals recorded over a smaller range of angles can be used to successfully reconstruct the image of a slice of an object. Therefore, if a hybrid detector system could be built having a number of detectors working in parallel, the total image recording time of each

slice of the sample of interest could be drastically reduced, with only one or maybe two rotations of the detector unit required.

7. Conclusion

The work presented in this thesis has been concerned with the propagation of terahertz radiation through non-homogeneous materials and structures. This work was initially motivated by the possible application of THz to security applications.

Terahertz radiation from pulsed sources extends over a broad range of frequency components. The region is broadly defined as the frequency range 300 GHz – 10 THz, or in wavelength 1mm to 300 μm. Photons of terahertz radiation are consequently of an energy which is comparable to the characteristic energies of specific internal processes in many materials. Resonances thus occur at THz frequencies with groups of molecules undergoing vibrational, twisting and breathing motions. THz radiation can also pass through certain opaque objects, revealing what is behind them. This makes it a promising candidate to fulfil applications in numerous areas of security and surveillance, as well as biology and biophysics (chapter one). Due to the position of the terahertz region within the electromagnetic spectrum, it is not possible to generate convenient bright sources or produce simple detectors using conventional physical methods. Therefore, numerous novel ways have been sought to bridge this gap in the last thirty or so years (chapter two), the most common of which uses optoelectronic techniques to generate and detect the radiation. From the very nature of broadband THz pulses, their various components will be affected differently when they pass through everyday media having a random internal structure (chapter three). A simple model (the Phase Distribution Model) to describe this behaviour has been proposed and tested.

Pulses of THz radiation from laser driven sources have complex shapes. Thus, confusion can arise if their temporal profile is used in experimental investigations. By application of suitable signal processing algorithms (chapter four) useful information can be obtained regarding the temporal profile of a THz pulse. The investigation of THz radiation scattered by targets of interest is highly desirable. A novel scattering spectrometer is required to undertake this and its development is described (chapter five). Scattered radiation can then be used to image objects of interest and reveal their internal structure, which is described in chapter six.

A very brief overview of terahertz radiation was given in chapter one. Researchers have been interested in the terahertz region of the spectrum from the time of Herschel. This frequency region is just one small portion of the electromagnetic spectrum for which the associated physical phenomena are most conveniently described by the Maxwell equations. However, work in this region was initially limited by the lack of suitable sources and detectors, with a gap existing between optical methods (on the high frequency side) and electronic means (for longer wavelengths) for the production of bright sources. The lack of conveniently operable detectors was also a limiting factor in the application of this spectral range. The advent of optoelectronic sources in the 1970's and 1980's fuelled the growth in THz techniques. Applications of both terahertz imaging and terahertz spectroscopy exist across a wide range of disciplines (security, medical, semiconductor and microscopy), with many more possible areas currently emerging in the fields of artificial materials and biophysics.

Many methods have been developed to bridge the so-called 'THz gap,' and these were discussed in chapter two. Optoelectronic sources provide the most convenient way to generate THz employing a transducer to convert ultrashort pulses of near infrared laser light into pulses of terahertz radiation. These THz pulses contain a broad bandwidth of frequencies and are mainly generated using what is known as "photoconductive sources." Photoconductive sources have been extensively developed since the first report of generating sub-picosecond electric pulses using dipoles. Using the reverse process to emission allowed coherent detectors of THz radiation to be constructed. These provide convenient and efficient ways of detecting the low powers emitted from a THz optoelectronic source. Both of these techniques require pulsed laser technology, and it was the advent of this which enabled the expansion of terahertz research in the 1990's. It has also been shown how photoconductive sources and electro-optic detection can be combined to produce a terahertz time domain spectrometer. A spectrometer such as this allows THz pulses to be recorded quickly and with a good signal to noise ratio. Standard physical techniques can then be applied to analyse these waveforms, most often by Fourier Transform, to investigate the absorption spectrum of a sample.

Terahertz spectrometers emit pulses of radiation over a broad spectral range. It is the different interaction characteristics of the various spectral components with samples of interest which makes THz so useful and potentially exciting. However, when a broadband pulse interacts with a sample of random structure, interference and scattering phenomena will also take place. These effects can be used to advantage for locating hidden objects, but can scramble the waveform of the detected signal, making interpretation difficult. Chapter three provides a discussion of some of the major phenomena which can affect a THz pulse as it propagates through a sample, along with the development and testing of a simple model (the Phase Distribution Model) to predict the transmitting behaviour of a randomly structured sample. This model uses a statistical approach to describe the phase changing properties of a sample, which can be split into layers perpendicular to the direction of propagation, and relates the bulk transmission to this. Validation of the model was undertaken by comparing its predictions with: scattering from isolated objects; exact numerical solution of Maxwell's equations; and THz pulse transmission through various phantoms (cylinder arrays, fabrics and randomly arranged powders). Overall, a satisfactory agreement was seen for the cylinder arrays, whilst the model provided an excellent description of THz propagation through both randomly arranged spheres and clothing. The transmission results can also be used to make an informed discussion of the suitability of THz radiation in a stand-off detection system.

In addition to the above scattering and interference problems, a generic THz pulse has a complex shape. This means that its temporal profile often cannot easily be analysed. For example, echoes arise in the pulse from reflections within the source and detector which can interfere with pulses that are delayed within the sample. Oscillations also exist in the source pulse from its interaction with water vapour in the atmosphere. Chapter four outlines an approach to signal process such temporal waveforms after detection. The source pulse is numerically processed with a seed function, based on binomial forms, to produce a single, simple incident pulse with spectral content within the bandwidth of the actual source. By application of the algorithm to the pulse which has propagated through the sample, it is possible to investigate the response of the sample to the simple incident pulse and hence remove the undesired effects of the source after-runners on the temporal waveform. Various experiments were undertaken

to validate this method by the investigation of the transmission through and reflection from, various dielectric slabs. These results indicate that it is possible to resolve signals having amplitude less than 2% of the main pulse, which are hidden within the source pulse background and to determine the presence of much smaller gaps between layers of dielectric. By applying time gating to the reconstructed sample signal, it is also possible to investigate the response of a sample to a simple, single input pulse. Any structure in the reconstructed sample signal after passage of the directly transmitted beam will include information which is due to the delayed response of the sample to the THz pulse. It is found that this delayed emission is often not simply the reverse of the transmission spectra. The interpretation of this is still open to question and needs further work to relate the observed signal to identifiable physical processes.

In chapter five, the design and construction of a terahertz spectrometer with the capability to measure radiation scattered by samples was described. After various setbacks in the acquisition of a suitable pulsed laser source, a system was built which had the capability of making angular measurements of the scattered THz radiation profiles. The detection unit of the system was pumped using infrared pulses that had propagated along single mode optical fibre. Any pulse propagating through a transparent medium is dispersed, which causes both a lengthening of the pulse and the addition of a positive chirp. However, third order non-linear effects are also manifest when a pulse propagates through the medium, which spectrally broaden the pulse. Therefore, if the pulse can be suitably rephased, by use of a pair of gratings, it is possible to compress it. Since, ultrashort pulses already exist for the detection (and generation of THz radiation) the problem of ultrashort pulse propagation in fibres is thus reduced to the prevention of their temporal growth. It was found that if pulses of length 75 fs were launched into the optical fibre, the minimum exit pulse length, having sufficient power to generate carriers in the THz photoconductive detector, was 136 fs. Using such pulses to detect THz radiation, generated using freespace excitation of a photoconductive source, allowed a spectrometer of bandwidth 1.5 THz to be constructed. This bandwidth was limited by the necessity of the THz radiation to propagate through the substrate of the receiving chip.

After construction of the above scattering system, radiation which had been scattered by various samples was collected over the angular range of the detector. Using reconstruction algorithms, widely used in tomography, combined with post detection THz signal processing, allowed, to our knowledge, the first ever set of THz tomographic images to be obtained using a geometry in direct analogy with x-ray computed tomography. It was found that good images could be produced of phantoms constructed from metallic scatterers within a mechanical vacuum, but that the results for phantoms containing some form of scattering powder were variable. This was especially noticeable when high absorbing biotin powder, which has a good THz spectral fingerprint, was used as the scattering medium.

7.1 Suggestions for future work

This final part of the thesis makes suggestions on how the work undertaken could be extended. Some of these have already been alluded to in various parts of the manuscript.

Measurements of THz transmission through randomly structured objects have indicated that the phase distribution model provides good agreement for volume fractions of less than 0.5. It is known that the use of propagators (to describe the field transmitted through an object) provide an additional method for determining transmission in such situations, and further modelling in this general area would be useful. For measurements relating to pulse processing, THz systems of a broader bandwidth could be usefully employed to determine smaller gaps between layers. The simplest method for this would include a photoconducting source in reflection geometry with a thin electro-optic detection crystal. This method could also be usefully extended to investigate the use of signal processing of signals from three-layered structures of which the middle layer has spectral resonances in the THz regime. By use of signal processing with time gating, it should be possible to determine the spectral absorptions of the individual layers.

Much work has been expended on the development of a scattering terahertz spectrometer. The results produced by such a system, could be improved: if the detecting chip were incorporated onto the pre-amplification circuit in a shielded

metallic box (to remove as much excess electrical noise as possible); and the bandwidth increased by etching the substrate back to reduce the distance through which the THz beam propagates before reaching the detector electrodes. Further to this, if the whole detection unit could be miniaturised somewhat, it would be possible to place both receiving chip and sample at the approximate THz beam focus. This would allow small samples to be confined, for example artificial materials, within the focal point of the beam and their beam steering properties measured. It would also be useful to undertake work to investigate the feasibility of attaching a lens to the detector, providing that it only collected scattered radiation at one angle. This problem is reduced the nearer the detector can be placed to the focus, but would require modelling of the radiation profile detected and focused by the lens.

Due to the time constraints imposed by the return of the loan pool laser on the scattering system (and breakdown of the Femotlaser source) there was not really enough time to conduct a thorough study of THz scattering from random powders, especially those with THz signatures. Such experiments would prove the ability of a scattering spectrometer to locate and identify hidden objects. However, to make use of this type of spectrometer, methods need to be developed to increase the data acquisition speed. These could include: using a number of parallel off-axis detectors (it has already been shown that high quality images can be produced using larger angle step and appropriate contrast enhancement); and the use of a shaking device as the delay line. Further experiments could also usefully be undertaken to measure scattering from other random, dielectric arrays, for example the arrays of cylinders (with further extension to the modelling) and phantoms containing spectrally active powders.

[1] Herschel W. *Experiments on the Refrangibility of the invisible Rays of the Sun:* Phil Trans R. Soc **90** (1800) 284
[2] Rubens H. and Nichols E.F. *Heat rays of great wave length:* Phys. Rev. **4** (1897) 314
[3] Glagolewa-Arkadiewa A. *Short Electromagnetic Waves of Wavelength up to 82 Microns:* Nature **113** (1924) 640
[4] Nichols E.F. and Tear J.D. *Short electric waves:* Phys. Rev. **21** (1923) 587
[5] Rubens H. and Baeyer O.V. *On Extremely Long Waves Emitted by the Quartz Mercury Lamp:* Phil. Mag. **21** (1911) 689
[6] Golay M.J.E. *A Pneumatic Infra-Red detector:* Rev. Sci. Inst. **18** (1947) 357
[7] Kimmitt M.F. *Restrahlen to T-Rays – 100 years of Terahertz Radiation:* J. Bio. Phys. **29** (2003) 77
[8] Chamberlain J.M. *Where optics meets electronics: recent progress in decreasing the terahertz gap:* Phil. Trans. R. Soc. Lond. A **362** (2004) 199
[9] Chan W.L., Deibel J. and Mittleman D.M. *Imaging with terahertz radiation:* Rep. Prog. Phys **70** (2007) 1325
[10] Mittleman D.M., Gupta M., Neelamani R., Baraniuk R.G., Rudd J.V. and Koch M. *Recent advances in terahertz imaging:* Appl. Phys. B **68** (1999) 1085
[11] Federici J.F., Schulkin B., Huang F., Gary D., Barat R., Oliveira F. and Zimdars D. *THz imaging and sensing for security applications – explosives, weapons and drugs:* Semicond. Sci. Technol. **20** (2005) S266
[12] Liu H.-B., Chen Y., Bastiaans G.J. and Zhang X.-C. *Detection and identification of explosive RDX by THz diffuse reflection spectroscopy:* Opt. Exp. **14** (2006) 415
[13] Kemp M.C., Taday P.F., Cole B.E., Cluff J.A., Fitzgerald A.J. and Tribe W.R. *Security applications of terahertz technology:* SPIE **5070** (2003) 44
[14] Shen Y.C., Lo T., Taday P.F., Cole B.E., Tribe W.R. and Kemp M.C. *Detection and identification of explosives using terahertz pulsed spectroscopic imaging:* App. Phys. Lett. **86** (2005) 241116
[15] Burnett A., Fan W., Upadhya P.C., Cunningham J., Linfield E.H., Davies A.G., Edwards H., Munschi T. and O'Neil A. *Analysis of drugs-of-abuse and explosives using terahertz time domain and Raman Spectroscopy:* SPIE **6120** (2006) 155
[16] Kemp M.C. *Millimetre Wave and Terahertz Technology for Detection of Concealed Threats – A Review:* IEEE **07EX1863** (2007) 647
[17] Dutton P.L., Munro A.W, Scrutton N.S. and Sutcliffe M.J. *Introduction. Quantum catalysis in enzymes: beyond the transition state theory paradigm:* Phil. Trans. R. Soc. B **361** (2006) 1293
[18] Fischer B.M., Walther M. and Uhd Jepsen P. *Far-infrared vibrational modes of DNA components studied by terahertz time-domain spectroscopy:* Phys. Med. Biol. **47** (2002) 3807
[19] Whitmire S.E., Wolpert D., Markelz A.G., Hillebrecht J.R., Galan J. and Birge R.R. *Protein Flexibility and Conformational State: A Comparison of Collective Vibrational Modes of Wild-Type and D96N Bacteriorhodopsin:* Biophys J. **85** (2003) 1269
[20] Doria A., Gallerano G.P., Giovenale E., Messina G., Lai A., Ramundo-Orlando A., Sposato V., D'Arienzo M., Perrotta A., Romano M., Sarti M., Scarfi M.R., Spassvsky I. and Zeni O. *THz radiation studies on biological systems at the ENEA FEL facility:* Infra. Phys. & Tech. **45** (2004) 339
[21] Choi C.H., Kalosakas G., Rasmussen K.Ø., Hiromura M., Bishop A.R., Usheva A. *DNA dynamically directs its own transcription initiation:* Nucl. Acids Res. **32** 1584 (2004)
[22] Markelz A.G., Roitberg A. and Heilweil E.J. *Pulsed terahertz spectroscopy of DNA, bovine serum albumin and collagen between 0.1 and 2.0 THz:* Chem. Phys. Lett. **320** (2000) 42
[23] Brucherseifer M., Nagel M., Haring-Bolivar P., Kurz H., Bosserhoff A. and Büttner R. *Label-free probing of the binding state of DNA by time domain terahertz sensing:* App. Phys. Lett. **77** (2000) 4049
[24] Nagel M., Haring Bolivar P., Brucherseifer M., Kurz H., Bosserhoff A. and Büttner R. *Integrated THz technology for label-free genetic diagnostics:* App. Phys. Lett. **80** (2002) 15
[25] Arnone D.D., Ciesla C.M., Corchia A., Egusa S., Pepper M., Chamberlain J.M., Bezant C., Linfield E.H., Clothier R. and Khammo N. *Applications of terahertz technology to medical imaging:* SPIE **3828** (1999) 209
[26] Crawley D.A., Lonbottom C., Wallace V.P., Cole B.E., Arnone D.D. and Pepper M. *Three-dimensional terahertz pulse imaging of dental tissue:* J Biomed. Opt. **8** (2003) 303
[27] Woodward R.M., Cole B.E., Wallace V.P., Pye R.J., Arnone D.D., Linfield E.H. and Pepper M. *Terahertz pulsed imaging in reflection geometry of human skin cancer and skin tissue:* Phys. Med. Biol. **47** (2002) 3853
[28] Wallace V.P., Fitzgerald A.J., Shankar S., Flanagan N., Pye R.J., Cluff J. and Arnone D.D. *Terahertz pulsed imaging of basal cell carcinoma ex vivo and in vivo:* Br. J. Dermatol **151** (2004) 424
[29] Pickwell E., Cole B.E., Fitzgerald A.J., Pepper M. and Wallace V.P. *In vivo study of human skin using pulsed terahertz radiation:* Phys. Med. Biol. **49** (2004) 1595

[30] Fitzgerald A.J., Wallace V.P., Jimenez Linan M., Bobrow L., Pye R.J., Purushotham A.D. and Arnone D.D. *Terahertz pulsed Imaging of Human Breast Tumors:* Radiology **239** (2006) 533
[31] Pickwell E. and Wallace V.P. *Biomedical applications of terahertz technology:* J. Phys. D: App. Phys. **39** (2006) R301
[32] Van Exter M. and Grischkowsky D. *Optical and electronic properties of doped silicon from 0.1 to 2 THz:* App. Phys. Lett. **56** (1990) 1694
[33] Jeon T. and Grischkowsky D. *Characterization of optically dense, doped semiconductors by reflection THz time domain spectroscopy:* App. Phys. Lett. **72** (1998) 3032
[34] Nashima S., Morikawa O., Takata K. and Hangyo M. *Measurements of optical properties of highly doped silicon by terahertz time domain reflection spectroscopy:* App. Phys. Lett. **79** (2001) 3293
[35] Beard M.C., Turner G.M. and Schmuttenmaer C.A. *Transient photoconductivity in GaAs as measured by time-resolved terahertz spectroscopy:* Phys. Rev. B **62** (2000) 764
[36] Beard M.C., Turner G.M. and Schmuttenmaer C.A. *Subpicosecond carrier dynamics in low-temperature grown GaAs as measured by time resolved terahertz spectroscopy:* **96** (2001) 5915
[37] Hunsche S., Koch M., Brener I. and Nuss M.C. *THz near-field imaging:* Opt. Comm. **150** (1998) 22
[38] Van der Valk N.C.J. and Planken P.C.M. *Electro-optic detection of sub-wavelength terahertz spot sizes in the near field of a metal tip:* App. Phys. Lett. **81** (2002) 1558
[39] Chen H.T., Kersting R. and Cho G.C. *Terahertz imaging with nanometer resolution:* App. Phys. Lett. **83** (2003) 3009
[40] Chamberlain J.M. and Miles R.E. (eds) *New directions in terahertz technology:* Dordrecht: Kluwer (1997)
[41] Smith F.G. and King T.A. *Optics and Photonics. An Introduction:* Chapter 15 Wiley (2000)
[42] Rullière C. (ed) *Femtosecond laser pulses:* Chapter 1, Springer (2005)
[43] Gordon J.P., Zeiger H.J. and Townes C.H. *The Maser – New Type of Microwave Amplifier, Frequency standard and spectrometer:* Phys. Rev. **99** (1955) 1264
[44] Schawlow A.L. and Townes C.H. *Infrared and Optical Masers:* Phys Rev **112** (1960) 1940
[45] Maiman T.H. *Stimulated Optical Radiation in Ruby:* Nature **187** (1960) 493
[46] Javan A., Bennet W.R. and Herriot D.R. *Population Inversion and Continuous Optical Maser Oscillation in a Gas Discharge containing a He-Ne mixture:* Phys. Rev. Lett. **6** (1961) 106
[47] Gebbe H.A., Stone N.W.B., Findlay F.D. *Far infrared stimulated emission sources:* Nature **202** 685 (1964)
[48] Faist J., Capasso F., Siveo D.L., Sirtori C., Hutchinson A.L. and Cho A.Y. *Quantum Cascade Laser:* Science **264** (1994) 553
[49] Köhler R., Tredicucci A., Beltram F., Beere H.E., Linfield E.H., Davies A.G., Ritchie D.A., Iotti R.C. and Rossi F. *Terahertz semiconductor-hetrostructure laser:* Nature **417** (2002) 156
[50] Tredicucci A. *Recent Advances and Future Prospects of THz Quantum Cascade Lasers:* IEEE 07EX1863 (2007) 34
[51] Scalari G., Walther C., Faist J., Beere H. and Ritchie D. *Electrically switchable, two-color quantum cascade laser emitting at 1.39 and 2.3 THz:* App. Phys. Lett. **88** (2006) 141102
[52] Walther C., Scalari G., Faist J., Beere H. and Ritchie D. *Low frequency terahertz quantum cascade laser operating from 1.6 to 1.8 THz:* App. Phys. Lett **89** (2006) 231121
[53] Williams B.S., Kumar S., Hu Q. and Reno J.L. *Operation of terahertz quantum-cascade lasers at 164 K in pulsed mode and at 117 K in continuous-wave mode:* Opt. Exp. **13** (2005) 3331
[54] Tredicucci A. *Private Communication:* December 2007
[55] Auston D.H., Cheung K.P. and Smith P.R. *Picosecond photoconducting Hertzian dipoles:* App. Phys. Lett. **45** (1984) 284
[56] Bass M., Franken P.A., Ward J.F. and Weinreich G. *Optical Rectification:* Phys. Rev. Lett. **9** (1962) 446
[57] Kübler C., Huber R. and Leitenstorfer A. *Ultrabroadband terahertz pulses: generation and field-resolved detection:* Semicond. Sci. Tech. **20** (2005) S128
[58] Spence D.E., Kean P.N. and Sibbett W. *60-fsec pulse generation from a self-mode-locked Ti:sapphire laser:* Opt. Lett. **16** (1991) 42
[59] Rullière C. (ed) *Femtosecond laser pulses:* Chapter 2, Springer (2005)
[60] Rizvi N.H., French P.M.W. and Taylor J.R. *Continuously self-mode locked Ti:sapphire laser that produces sub-50 fs pulses:* Opt. Lett. **17** (1992) 279
[61] Kittel C. *Introduction to Solid state Physics:* Chapter 5, Wiley (1996)
[62] Auston D.H. *Picosecond optoelectronic switching and gating in silicon:* App. Phys. Lett. **26** (1975) 101
[63] Fattinger Ch. and Grischkowsky D. *Point source terahertz optics:* App. Phys. Lett **53** (1988) 1480
[64] Fattinger Ch. and Grischkowsky D. *Terahertz beams:* App. Phys. Lett. **54** (1989) 490
[65] Born M. and Wolf E. *Principle of Optics:* CUP, Chapter 2 (1980)

[66] Zhang X.-C., Hu B.B., Darrow J.T. and Auston D.H. *Generation of femtosecond electromagnetic pulses from semiconductor surfaces:* App. Phys. Lett. **56** (1990) 1011
[67] Zhang X.-C. and Auston D.H. *Optoelectronic measurement of semiconductor surfaces and interfaces with femtosecond optics:* J. App. Phys. **71** (1992) 326
[68] Johnston M.B., Whittaker D.M., Corchia A., Davies A.G. and Linfield E.H. *Simulation of terahertz generation at semiconductor surfaces:* Phys. Rev. B **65** (2002) 165301
[69] Uhd Jepsen P., Jacobsen R.H. and Keiding S.R. *Generation and detection of terahertz pulses from biased semiconductor antennas:* J. Opt. Soc. Am. B **13** (1996) 2424
[70] Darrow J.T., Zhang X.-C., Auston D.H. and Morse J.D. *Saturation Properties of Large-Aperture Photoconducting Antennas:* J. Quant. Elec. **28** (1992) 1607
[71] Tani M., Matsuura S., Sakai K. and Nakashima S. *Emission characteristics of photoconductive antennas based on low-temperature-grown GaAs and semi-insulating GaAs:* App. Opt. **36** (1997) 7853
[72] Cai. Y., Brener I., Lopata J., Wynn J., Pfeiffer L. and Federici J. *Design and performance of singular electric field terahertz photoconducting antennas:* App. Phys. Lett. **71** (1997) 2076
[73] Gregory I.S., Baker C., Tribe W.R., Evans M.J., Beere H.E., Linfield E.H., Davies A.G. and Missous M. *High resistivity annealed low-temperature GaAs with 100 fs lifetime:* App. Phys. Lett. **83** (2003) 4199
[74] Shen Y.C., Upadhya P.C., Linfield E.H., Beere H.E. and Davies A.G. *Ultrabroadband terahertz radiation from low-temperature-grown GaAs photoconductive emitters:* App. Phys. Lett. **83** (2003) 3117
[75] Uhd Jepsen P. and Keiding S.R. *Radiation patterns from lens-coupled terahertz antennas:* Opt. Lett. **20** (1995) 807
[76] Wu Q. and Zhang X.-C. *Freespace electro-optic sampling of terahertz beams:* App. Phys. Lett., **67** (1995) 3523
[77] Tipler P. *Physics,* Chapter 33 (Wiley), 1999
[78] Rullière C. (ed) *Femtosecond laser pulses:* Chapter 10, Springer (2005)
[79] Han P.Y. and Zhang X.-C. *Coherent, broadband midinfrared terahertz beam sensors:* App. Phys. Lett. **73** (1997) 3049
[80] Kono S., Tani M. and Sakai K. *Ultrabroadband photoconductive detection: comparison with free space electro-optic sampling:* App. Phys. Lett. **79** (1997) 898
[81] Park S.-G., Melloch M.R. and Weiner A.M. *Comparison of terahertz waveforms measured by electro-optic and photoconductive sampling:* App. Phys. Lett. **73** (1998) 3184
[82] Cai Y., Brener I., Lopata J., Wynn J., Pfeiffer L., Stark J.B., Wu Q., Zhang X.-C and Federici J.F. *Coherent terahertz radiation detection: Direct comparison between free-space electro-optic sampling and antenna detection:* App. Phys Lett. **73** (1998) 444
[83] Kono S., Tani M., Gu P. and Sakai K. *Detection of up to 20 THz with a low-temperature-grown GaAs photoconductive antenna gated with 15 fs light pulses:* App. Phys. Lett. **77** (2000) 4104
[84] Shen Y.C., Upadhya P.C., Beere H.E., Linfield E.H., Davies A.G., Gregory I.S., Baker C., Tribe W.R., Evans M.J. *Generation and detection of ultrabroadband terahertz radiation using photoconductive emitters and receivers:* App. Phys Lett. **85** (2004) 164
[85] Zhao G., Schouten R.N., van der Valk N., Wenckebach W. Th. and Planken P.C.M. *Design and performance of a THz emission and detection setup based on a semi-insulating GaAs emitter:* Rev. Sci. Inst. **73** (2002) 1715
[86] Beard M.C., Turner G.M. and Schmuttenmaer C.A. *Terahertz spectroscopy:* J. Phys. Chem. B **106** (2002) 7146
[87] Smith F.G. and King T.A. *Optics and Photonics. An Introduction:* Chapter 5 Wiley (2000)
[88] Born M. and Wolf E. *Principle of Optics:* CUP, Chapter 1 (1980)
[89] Uhd Jepsen P. and Fischer B.M. *Dynamic range in terahertz time domain transmission and reflection spectroscopy:* Opt. Lett. **30** (2005) 19
[90] van Exter M., Fattinger Ch. and Grischkowsky D. *Terahertz time-domain spectroscopy of water vapor:* Opt. Lett. **14** (1989) 1128
[91] O'Leary M.A., Boas D.A., Li X.D., Chance B. and Yodah A.G. *Fluorescence lifetime imaging in turbid media:* Opt. Lett. **21** (1996) 158
[92] Pearce J. and Mittleman D.M. *Propagation of single-cycle terahertz pulses in random media:* Opt. Lett. **26** (2001) 2002
[93] Fletcher J.R., Swift G.P., Levitt J.A., Dai D. and Chamberlain J.M. *Propagation of terahertz radiation through random structures: An alternative theoretical approach and experimental validation:* J. App. Phys. **101** (2007) 013102
[94] Ishimaru A. *Wave Propagation and Scattering in Random Media: Volumes 1 and* 2 Academic Press (1978)

[95] Ishimaru A. *Wave Propagation and Scattering in Random Media (Single Scattering and Transport Theory), Vol. 1, Chapter 2:* Academic Press (1978)
[96] Ishimaru A. *Wave Propagation and Scattering in Random Media (Single Scattering and Transport Theory), Vol. 1, Chapter4:* Academic Press (1978)
[97] Pearce J. and Mittleman D.M. *Using terahertz pulses to study light scattering:* Physica B **338** (2003) 92
[98] Pearce J. and Mittleman D.M. *Scale model experimentation: using terahertz pulses to study light scattering:* Phys. Med. Biol. **47** (2002) 3823
[99] Cheville R.A. and Grishkowsky D. *Time domain terahertz impulse ranging studies:* App. Phys. Lett. **67** (1995) 1960
[100] Pearce J., Jian. Z. and Mittleman D.M. *Statistics of Multiply Scattered Broadband Terahertz Pulses:* Phys. Rev. Lett. **91** (2003) 043903
[101] Jian Z., Pearce J. and Mittleman D.M. *Characterizing Individual Scattering Events by Measuring the Amplitude and Phase of the Electric Field Diffusing through a Random Medium:* Phys. Rev. Lett. **91** (2003) 033903
[102] Pearce J., Jian Z. and Mittleman D.M. *Bayesian approach to non-Gaussian field statistics for diffusive broadband terahertz pulses:* Opt. Lett. **30** (2005) 2843
[103] Pearce J., Doyle K., Jian Z., Deibel J. and Mittleman D.M. *Nonstationary time-domain statistics of multiply scattered broadband terahertz pulses:* J. Opt. Soc. Am. B **23** 1506 (2006)
[104] Chau K.J. and Elezzabi A.Y. *Terahertz transmission through ensembles of subwavelength-size metallic particles:* Phys. Rev. B **72** (2005) 075110
[105] Mujumdar S., Chau K.J. and Elezzabi A.Y. *Experimental and numerical investigation of terahertz transmission through strongly scattering sub-wavelength size spheres:* App. Phys. Lett. **85** (2004) 6284
[106] Ratcliffe J.A., Rep. Prog. Phys. **19** 188 (1956)
[107] Fejer J.A., Proc. R. Soc. Lond. Ser. A **220** 455 (1953)
[108] Bell P.M., Pendry J.B., Martin Moreno L. and Ward A.J. *A program for calculating photonic band structures and transmission coefficients of complex structures:* Comp. Phys. Comm. **85** (1995) 306
[109] Bjarnason J.E., Chan T.L.J., Lee A.W.M., Celis M.A. and Brown E.R. *Millimeter-wave, terahertz, and mid-infrared transmission through common clothing:* App. Phys. Lett **85** (2004) 519
[110] Planken P.C.M., van Rijmenam C.E.W.M. and Schouten R.N. *Opto-electronic pulsed THz systems:* Semicond. Sci. Technol **20** (2005) S121
[111] Mathematical technique of pulse reconstruction has been patented: **GB0708491.6**: *'Pulse Reconstruction.'*
[112] Dragoman D. and Dragoman M. *Time-frequency signal processing of terahertz pulses:* App. Opt. **43** (2004) 3848
[113] Mittleman D.M., Hunsche S., Boivin L. and Nuss M.C. *T-ray tomography:* Opt. Lett. *22* (1997) 904
[114] Oppenheimer A.V. and Shafer R.W. *Discrete Time Signal Processing:* Prentice-Hall (1998)
[115] Pashkin A., Kempa M., Němec H., Kadlex F. and Kužel P. *Phase-sensitive time-domain terahertz reflection spectroscopy:* Rev. Sci. Inst. **74** (2003) 4711
[116] Khazan M., Meissner R. and Wilke I. *Convertible transmission-reflection terahertz time-domain spectrometer:* Rev. Sci. Inst. **72** 3427 (2001)
[117] Born M. and Wolf E. *Principle of Optics:* CUP, Chapter 7 (1980)
[118] Harde H., Keiding S. and Grischkowsky D. *THz Commensurate Echoes: Periodic Rephasing of Molecular Transitions in Free-Induciton Decay:* Phys. Rev. Lett. **66** (1991) 1834
[119] Harde H., Cheville R.A. and Grischkowsky D. *Terahertz Studies of Collision Broaden Rotational Lines:* J. Phys. Chem. **101** (1997) 3646
[120] Planken P.C.M. and Bakker H.J. *Towards time-resolved THz imaging:* App. Phys. A. **78** (2004) 465
[121] Korter T.M. and Plusquellic D.F. *Continuous-wave terahertz spectroscopy of biotin: vibrational anharmonicity in the far-infrared:* Chem. Phys. Lett. **385** (2004) 45
[122] Ferguson B., Wang S., Gray D., Abbot D. and Zhang X.-C. *T-ray computed tomography:* Opt Lett. **27** (2002) 1312
[123] Pearce J., Jian Z. and Mittleman D.M. *Propagation of terahertz pulses in random media:* Phil. Trans. R. Soc. Lond. A **362** (2004) 301
[124] Crooker S.A. *Fiber-coupled antennas for ultrafast coherent terahertz spectroscopy in low temperatures and high magnetic fields:* Rev. Sci. Inst. **73** (2002) 3258
[125] Van Rudd J., Johnson J.L. and Mittleman D.M. *Cros- polarized angular emission patterns from lens-coupled terahertz antennas:* J. Opt. Soc. Am. B. **18** (2001) 1524
[126] Van Rudd J. and Mittleman D.M. *Influence of substrate-lens design in terahertz time domain spectroscopy:* J. Opt. Soc. Am. B. **19** (2002) 319

[127] Treacy E.B. *Optical Pulse Compression With Diffraction Gratings:* J. Quant. Elec. **QE-5** (1969) 454
[128] Yang T.-Y., Ho P.-P., Katz A., Alfano R.R. and Ferrante R.A. *Femtosecond laser pulse compression using volume phase transmission holograms:* App. Opt. **24** (1985) 2021
[129] Rullière C. (ed) *Femtosecond laser pulses:* Chapter 6, Springer (2005)
[130] Weber H.P. *Method of Pulsewidth Measurement of Ultrashort Light Pulses Generated by Phase-Locked Lasers using Nonlinear Optics:* J. App. Phys. **38** (1967) 2231
[131] Rullière C. (ed) *Femtosecond laser pulses:* Chapter 7, Springer (2005)
[132] Gallant A.J., Kaliteevski M.A., Wood D., Petty M.C., Abram R.A., Brand S., Swift G.P., Zeze D.A. and Chamberlain J.M. *Passband filters for terahertz radiation based on dual metallic photonic structures:* App. Phys. Lett. **91** (2007) 161115
[133] Wu D., Fang N., Sun C., Zhang X., Padilla W.J., Basov D.N., Smith D.R. and Schultz S. *Terahertz plasmonic high pass filter:* App. Phys. Lett. **83** (2003) 201
[134] Herman G.T. *Image reconstruction from projections: The fundamentals of Computerised Tomography:* Academic Press (1980)
[135] Kak A.C. and Slaney M. *Principles of Computerized Tomographic Imaging:* IEEE Press, New York (1987)
[136] Hartwick T.S., Hodges D.T., Barker D.H. and Foote F.B. *Far infrared imagery:* App. Opt. **15** 1919 (1976)
[137] Hu B.B. and Nuss M.C. *Imaging with terahertz waves:* Opt. Lett. **20** (1995) 1716
[138] Zhong H., Xu J., Xie X., Yuan T., Reightler R., Madaras E., and Zhang X-C. *Nondestructive Defect Identification with Terahertz Time-of-Flight Tomography:* IEEE Sensors J **5** (2005) 203
[139] Pearce J., Choi H., Mittleman D. M., White J. and Zimdars D. *Terahertz wide aperture reflection tomography:* Opt. Lett. **30** (2005) 1653
[140] Nguyen K.L., Johns M.L., Gladden L.F., Worrall C.H., Alexander P., Beere H.E., Pepper M., Ritchie D.A.., Alton J., Barbieri S. and Linfield E.H. *Three-dimensional imaging with a terahertz quantum cascade laser:* Opt. Exp. **14** (2006) 2123
[141] Wang S. and Zhang X.-C. *Pulsed terahertz tomography:* J. Phys. D: Appl. Phys. **37** (2004) R1
[142] Huggard P.G., Shaw C.J., Cluff J.A. and Andrews S.R. *Polarization-dependent efficiency of photoconducting THz transmitters and receivers:* App. Phys. Lett. **72** (1998) 2069
[143] Castro-Camus E., Lloyd-Hughes J., Johnston M.B., Fraser M.D., Tan H.H. and Jagadish C. *Polarization-sensitive terahertz detection by multicontact photoconductive receivers:* App. Phys. Lett **86** (2005) 254102